2018

Detailed Understanding of Flow, Heat Transfer, and Pressure Drop Behavior in a Square Channel With 45 Deg Ribs

Lumaya Ahmed
University of Central Florida

DETAILED UNDERSTANDING OF FLOW, HEAT TRANSFER, AND PRESSURE DROP BEHAVIOR IN A SQUARE CHANNEL WITH 45 DEG RIBS

by

LUMAYA AHMED
B.S. Mechanical Engineering, Bangladesh University of Engineering & Technology, 2009
M.S. Mechanical Engineering, Bangladesh University of Engineering & Technology, 2012
M.S. Mechanical Engineering, University of Central Florida, 2014

A dissertation submitted in partial fulfillment of the requirements
for the degree of Doctor of Philosophy
in the Department of Mechanical and Aerospace Engineering
in the College of Engineering and Computer Science
at the University of Central Florida
Orlando, Florida

Fall Term
2018

Major Professor: Jayanta S. Kapat

ABSTRACT

Internal Duct Cooling (IDC) with rib turbulators is one of the common cooling techniques applied inside the turbine airfoils. It is very important for the gas turbine industry to design and develop an optimized cooling channel that maximizes the amount of heat removed, while simultaneously minimizing the pressure drop for a target overall cooling effectiveness. Angled ribs perform superior to the transverse ribs due to additional secondary flow associated with them. However, they result in a highly non-homogenous heat transfer distribution, which is a manifestation of the complex, turbulent flow field inside the channel. It is very important to comprehend the secondary flow physics to characterize the heat transfer distribution in such angled ribbed channels. Additionally, due to the manufacturing constraint, the gas turbine industry encounters a challenge to make ribs edge sharp and results in ribs with rounded edges. The one of the main objectives of the present study is to provide a fundamental understanding of the flow physics on the heat transfer and pressure drop behavior in 45° ribbed channels both with sharp and rounded-edge ribs. It is found that the secondary flow has a significant effect on the heat transfer behavior for both types of ribs. There is a great need of high-fidelity PIV flow field data in the inter-rib space for an angled ribbed channel which can be used for CFD validation, especially for LES. The current study provides benchmarking flow field data in the inter-rib space in a square channel with 45° ribs using stereoscopic PIV technique. Besides the experiments, numerical studies were also conducted by using LES and different RANS models. The LES results show an excellent prediction capability for aerothermal behavior in such channels. However, the prediction capability of RANS models is found to be inconsistent for different rib configurations and flow conditions.

DEDICATED TO MY BELOVED FAMILY. THANK YOU FOR EVERYTHING.

ACKNOWLEDGMENTS

I am grateful to my supervisor, Dr. Jayanta Kapat whose determination, discipline, and passion for research have helped me to mature as a researcher.

I want to thank all members of my supervisory committee for their mentorship.

I want to thank all my colleagues at the CATER lab, especially Michael Elmore, Patrick Tran, Christopher Vergos, Luisana Calderon, and Dr. Erik Fernandez.

My husband, Md. Mahmudul Hasan who always stand by me in my difficult times.

My parents whom I love and respect so much. They have always been there for me.

TABLE OF CONTENTS

LIST OF FIGURES

LIST OF TABLES

LIST OF NOMENCLATURES

A_c	=	Cross sectional area of the channel = $H \times W$
AR	=	Aspect ratio of the channel = $\frac{W}{H}$
C_P	=	Specific heat of air
C_s	=	Smagorinsky model constant
C_w	=	WALE model constant
D_h	=	Hydraulic diameter of the channel = $\frac{2\times H\times W}{(H+W)}$
e	=	Rib height
$e+$	=	Roughness Reynolds number
f	=	Friction factor $= \frac{\frac{\Delta P}{\Delta Z} D_h}{0.5\, \rho_{air} {U_b}^2}$
f_i	=	Body force
H	=	Channel height (m)
h	=	Heat transfer coefficient
k	=	Thermal conductivity
k	=	$\frac{1}{2}\, \overline{u'_\iota u'_\iota}$, Turbulent kinetic energy
L	=	Period length
l_r	=	Extent of the vortex, V1
$\dot{m}$	=	Mass flow rate
Nu	=	Nusselt number
$\mathrm{Nu_x}$	=	Module average Nusselt number

P = Rib pitch

P = Pressure

p = Pressure

Q = Surface heat transfer rate

Q = Q criterion

Q_{input} = Heat input

$Q_{leakage}$ = Heat loss

R = Gas Constant

R = Electrical resistance

r = Fillet radius of the ribs

Re = Reynolds number

RXX = Reynolds normal stress in spanwise direction = $\overline{u'^2}$

RXY = Reynolds shear stress = $\overline{u'v'}$

RXZ = Reynolds shear stress = $\overline{u'w'}$

RYY = Reynolds normal stress in wall normal direction = $\overline{v'^2}$´

RYZ = Reynolds shear stress = $\overline{v'w'}$

RZZ = Reynolds normal stress in streamwise direction = $\overline{w'^2}$

S = Strain rate tensor

S_{ij} = Mean strain rate

t = time

T = Temperature

T_{amb} = Ambient temperature

T_b = Local bulk temperature

T_f = Bulk temperature of the fluid

T_{f_0} = Bulk temperature of the fluid at the inlet

U = Uncertainty

u^* = Friction velocity

u' = Velocity fluctuation in *X* direction

U_b = Bulk velocity

u_i = Instantaneous velocity vector

$\overline{u_i}$ = Mean velocity

$\overline{U_i}$ = Resolved velocity

v = Average velocity

V = Voltage

v' = Velocity fluctuation in *Y* direction

V_X, V_Y, V_Z= Mean velocity in *X, Y, Z* direction

V_X', V_Z' = Mean velocity in *X´, Z´* direction

W = Channel width

w = Rib width

w' = Velocity fluctuation in *Z* direction

x = Module number

X, Y, Z= Spanwise, wall normal, streamwise direction

X´, Z´ = Direction along and normal to the ribs

y^+ = Dimensionless wall distance

y^* = Height of vortex (V1) core

Greek

α = Angle of attack of the ribs

β = Pressure gradient

γ = Temperature gradient

θ = Dimensionless temperature variable

λ = Dimensionless temperature gradient

δ_{ij} = Kronecker delta

Δ = Difference between two parameters

Δ = Filter width

Δ = Grid Size

$\Delta d+$ = Nondimensional size of the unstructured grid

$\Delta x+$, $\Delta y+$, $\Delta z+$ = Nondimensional grid size in *X*, *Y*, *Z* directions

ε = turbulent dissipation rate

η = Thermal performance

μ = Molecular viscosity

μ_{SGS} = SGS Eddy viscosity

μ_t = Turbulent eddy viscosity

υ = Kinematic molecular viscosity

υ_{SGS} = Kinematic SGS eddy viscosity

υ_t = Kinematic turbulent eddy viscosity

ρ = Density

ρ_{air} = Air density

$\mathcal{T}$ = Reduced temperature

τ = Shear stress

τ_{ij} = Subgrid stress

ω = Specific rate of dissipation

Ω = Vorticity tensor

Subscripts

amb = Ambient

0 = Smooth channels

x = Module number

w = Wall

Acronyms

CFD = Computational Fluid Dynamics

CMOS = Complementary Metal-Oxide-Semiconductor

EVM = Eddy Viscosity Model

FDI = Fully Developed Interface

HWA = Hot Wire Anemometry

LES = Large Eddy Simulation

PIV = Particle Image Velocimetry

RANS = Reynolds-Averaged Navier-Stokes

SGS = Subgrid Scale

TKE = Turbulent Kinetic Energy

WALE = Wall-Adapting Local Eddy-viscosity SGS Model

Abbreviations

$(\acute{})$ = Fluctuating component

$(\bar{})$ = Time averaged quantity

CHAPTER 1: INTRODUCTION

Background

Gas turbines are the prime movers in land-based power generation, aviation, oil and gas industries, processing plants, etc. The thermodynamic cycle of the gas turbine is the Brayton cycle as shown in Figure 1. The thermal efficiency of the Brayton cycle primarily depends on the turbine inlet temperature. To achieve higher power output and higher thermal efficiency, advanced gas turbines operate at very high inlet temperature (~ 1500°C or above) which exceeds the melting temperature of the metallic airfoils of the turbine. First stage turbine airfoils are most susceptible to this kind of damage since those are exposed to the hottest gases from the exit of the combustor. To ensure safe operation of the gas turbine, it is necessary to maintain the turbine airfoils several hundred degrees below the operating temperatures.

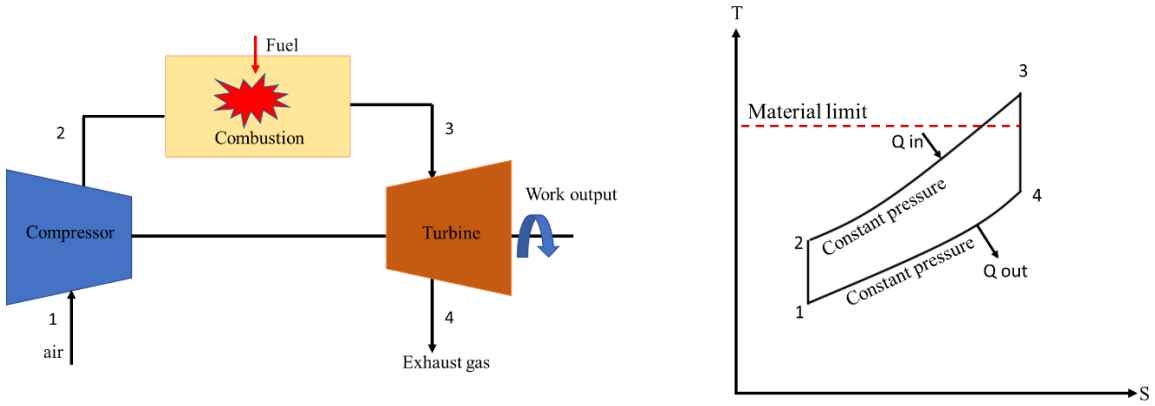

Figure 1 Ideal thermodynamic cycle (Brayton cycle)

In modern gas turbines, both Thermal Barrier Coating (TBC) and different sophisticated cooling techniques are incorporated for the reliable operation of the engine. TBC is applied on the turbine airfoils and it acts as insulation which allows a 200°F-300°F higher turbine inlet temperature. To cool the turbine airfoils, the coolant air is extracted from the compressor which is also known as compressor bleed air. The cooling techniques used in modern gas turbines' airfoils are broadly categorized into two types, i.e. (i) internal and (ii) external cooling. In one of the internal cooling techniques, the compressor bleed air is circulated through multiple serpentine channels inside of the airfoils. Such cooling technique is known as the Internal Duct Cooling (IDC). The impingement and pin-fin cooling are the other internal cooling methods used in turbine airfoils. A portion of the inside coolant is evicted out through some discrete holes. This ejected cooler air forms a blanket along the airfoil surface and protects the metal from the hot gases which is known as Film cooling. The extraction of compressor bleed air for cooling causes a reduction in the power output as well as the thermal efficiency of the engine. If the coolant flow is too little, it causes high airfoil temperature and reduces component life. If the flow is excessive, it decreases engine' thermal efficiency. Therefore, novel cooling strategies are paramount to the successful turbine operations.

Turbine Airfoil Cooling Techniques

To obtain high overall cooling efficiency, modern gas turbines use very sophisticated, complex cooling techniques. Some of the cooling techniques used in turbines' airfoils also vary between engine manufacturers. Figure 2 shows a sectional view of a turbine's airfoil. Different zones of the airfoils are cooled with different cooling methods based on its thermal load. The film cooling holes

are applied at the different zones, such as the leading edge, pressure, and suction sides, and the airfoil's tip area. The leading edge faces the highest thermal load as the hot gas directly impinges in this zone. The jet impingement along with film cooling is applied to cool this zone. The pin fins and the trailing edge ejection is utilized to cool the trailing edge as this area has space restriction. The zone in between the leading and trailing edge is known as the main body. Internal duct cooling is applied to cool this portion.

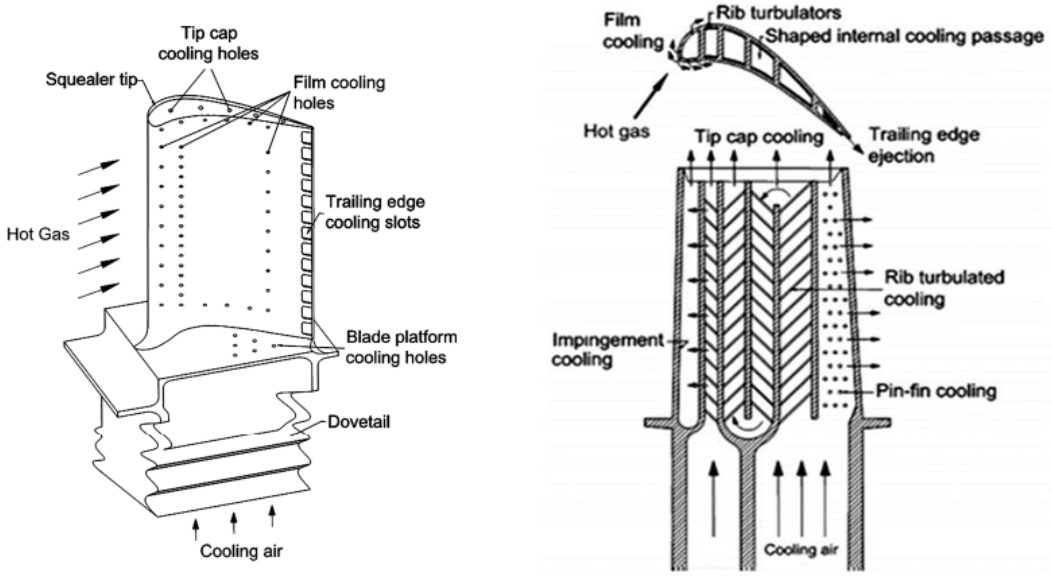

Figure 2 Schematic of turbine airfoil with different cooling technologies in different zones [1]

Turbulated Internal Duct Cooling

Inside turbine airfoils, cold air circulates through the internal cooling channels. The cooling performance of internal cooling channels is often improved by applying different types of

turbulators within the channels. For instance, ribs, pin fins, wedges, dimples, etc. are the different kinds of turbulators used in the internal cooling channels. Turbulators help in heat transfer enhancement by disrupting viscous sublayer formation and promoting mixing of the hotter fluid near the metallic surface with the colder fluid at the core. Research has found that the boundary layer separation occurs both in front and behind the ribs (as shown in Figure 3) as well as on top of the ribs [2]. The separated flow reattaches again and increases the Heat Transfer Coefficient (HTC). However, turbulators are also responsible for high pressure drop due to high friction factors. To improve the cooling performance of turbulated internal cooling channels of gas turbine airfoils, it is essential to design and develop an optimized channel that maximizes the amount of heat removed, while simultaneously minimizing the pressure drop, and subsequently lowering the coolant flow rate for a target overall cooling effectiveness. The efficiency of the internal cooling channel depends on the flow pattern inside the cooling channel which in turn depends on rib parameters, such as, rib height (e), rib pitch (P), blockage ratio ($\frac{e}{D_h}$), the relative orientation of the ribs (α) to the flow direction. In addition to this, the flow pattern is also influenced by the channel geometry (cross-section, aspect ratio, AR) and the coolant flow rate (Re).

Literature Review

Turbulated Internal Duct Cooling Channel

For the past few decades, research on the evaluation and improvement of the cooling performance of different types of turbulated internal cooling passages has been of great interest. Many experimental and numerical investigations have been conducted to quantify the heat transfer

coefficient values (both local and overall) and friction factor (*f*) of the internal cooling channels with different turbulators configuration over the last fifty years. J.C Han and his group did many early research on different aspects of rib turbulators. For example, Han [3] studied the heat transfer and friction behavior in rectangular channels roughened with transverse ribs ($\frac{e}{D_h}$ = 0.047 and 0.078; *P*/*e* = 10 and 20) for Re = 10,000-60,000. They found that the streamwise distribution of regional average Nusselt result shows periodicity (fully developed flow) after $3D_h$ after the entrance. They observed that ribs not only enhance the heat transfer of the ribbed walls but also that of the adjacent smooth walls by 20% - 50%. Their investigations were performed under different channel aspect ratio (*AR* = 1/4, 1/2, 1, 2, 4) and found that the narrower channel had higher heat transfer enhancement for the ribbed walls but showed slightly lower value for the average (average of ribbed walls and smooth walls) heat transfer enhancement.

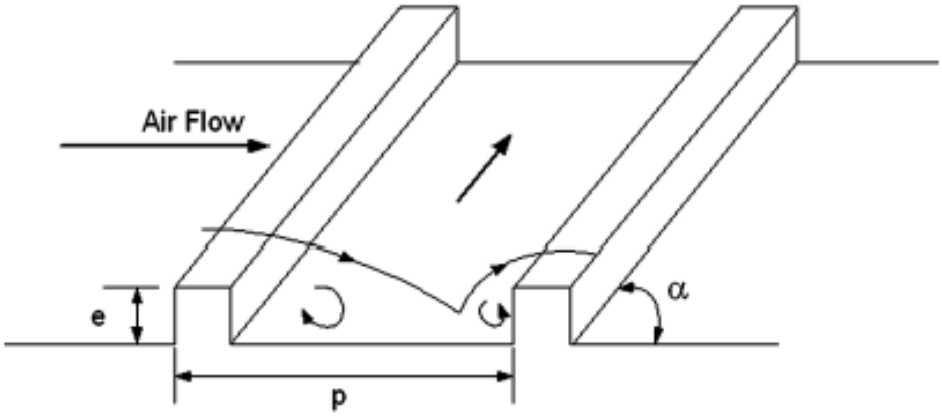

Figure 3 Flow separation by angled ribs [1]

Han et al. [4] also studied the effect of the angle of attack (90°, 60°, 45°, and 30°) of the ribs on the heat transfer and friction behavior in a square channel ($\frac{e}{D_h}$ = 0.0625; P/e = 10) for Re = 7,000-90,000. It was found that, besides the flow separation, inclined ribs caused additional secondary flow structures, which enhances heat transfer notably. For instance, the heat transfer enhancement with inclined ribs (α = 45°, 30°) was about 10%–20% higher than the transverse ribs. Moreover, the inclined ribs also cause 20% - 50% lower pressure drop than the transverse ribs. However, the amount of additional heat transfer enhancement caused by the ribs also depends on the aspect ratio of the channel. Han and Park [5] investigated ($\frac{e}{D_h}$ = 0.047, and 0.078; P/e = 10 and 20; Re = 10,000-50,000) the collective effects of the rib's orientation angle (30°, 45°, 60°, 90°) and the channel aspect ratio (AR = 1, 2, 4). Their results showed that the angle-of-attack of the ribs highly affects the heat transfer performance in a square channel; whereas, it has little effect on a rectangular channel (with AR = 2 and 4). For instance, angled ribs (30° and 45°) show almost 30% and only 5% higher heat transfer performance than transverse ribs in a square channel and a rectangular channel, respectively. They also proposed the semi-empirical correlations for heat transfer and friction using the similarity law of the wall. These correlations consider the orientation angle and spacing of the ribs, channel aspect ratio, and blockage ratio and flow Re. This correlations are applicable for their experimental range: $e^+ > 50$, $30° < \alpha < 90°$, $0.021 < e/D_h < 0.078$, $10 < P/e < 20$, $1 < W/H < 4$, and $8000 < \text{Re} < 80000$, where, e^+ is viscous scaled roughness height (ratio of the roughness height to viscous effects) or also called as roughness Reynolds number. This parameter is one of the most important length scales which is essential to classifying a rough-walled flow which is defined as, $e^+ = \frac{eu^*}{\vartheta} = (\frac{e}{D_h})Re\sqrt{\frac{f}{2}}$, where, the friction velocity $u^* = \sqrt{\frac{\tau_w}{\rho}}$.

Park et al. [6] ($\frac{e}{D_h}$ = 0.047 and 0.078, P/e = 10; AR = 1/4, 1/2, 1, 2, 4; Re = 10,000 to 60,000) reported that the 60°/45° ribs offer the maximum heat transfer performance for the AR = 1. The 45°- 60° ribs show higher thermal performance for the lower aspect ratio channel (AR = l/4 or l/2), while 30°/45° ribs display superior performance for the larger AR. That concludes that 45° ribs perform good irrespective of all the aspect ratios. So far, it was found that inclined ribs perform better than the transverse ribs, but it is not always true. Taslim and Lengkong [7] investigated heat transfer performance of 45° and 90° ribs (both sharp and rounded corners) with higher blockage ratio ($\frac{e}{D_h}$ = 0.133, 0.167, and 0.25; P/e = 5,8.5, and 10; Re = 10,000-50,000) in a square channel. Their results show that for high blockage ratio ribs ($\frac{e}{D_h}$ = 0.25), the transverse ribs have superior thermal performance than 45° ribs.

Bailey and Bunker [8] studied the heat transfer performance of staggered 45° ribs with high blockage ratio ($\frac{e}{D_h}$ = 0.193-0.333) in a rectangular channel with an aspect ratio of 2.5. Their results also agreed with Taslim and Lengkong [7] that with higher blockage ratio ribs, transverse ribs cause higher heat transfer than 45° ribs. They illustrated the reason behind this contradictory phenomenon. As mentioned earlier, the secondary flow structures caused due to the angled ribs are the primary factor of the increase in heat transfer enhancement by inclined ribs over transverse ribs. However, in case of high blockage ratio inclined ribs, the strength of the rotating cell secondary flow structures gets reduced, which results in lower heat transfer augmentation than transverse ribs. Taslim et al. [9] also investigated the effects of the number of ribbed walls and

found that roughening all walls with ribs has much potential for increasing the heat transfer performance.

Some researchers also studied the effect of the distance between the ribs (P/e) on the heat transfer and pressure drop behavior in a ribbed channel. For example, Taslim and Spring [10] researched how the rib spacing affects the heat transfer and friction performance in a rectangular channel (AR = 2) turbulated with transverse ribs. They also varied the rib blockage ratio ($\frac{e}{D_h}$) in the range between 0.15-0.285. Their results show that a favorable rib spacing P/e exists for every $\frac{e}{D_h}$. If there is sufficient space between the ribs, the flow reattachment occurs. This reattachment zone shows the maximum heat transfer enhancement and then reduces continuously in the flow direction before it hits the following rib. Therefore, intentional reduction in the distance after the reattachment location helps to increase the heat transfer enhancement. Conversely, if the rib space is decreased too much such that the length is not enough for the reattachment, the zone of the high heat transfer coefficient associated with it is absent and reduces the heat transfer enhancement. However, this phenomenon is valid for transverse ribs only. It is found in the literature that in the case of 45° ribbed channel, the heat transfer enhancement increases monotonically with the reduction of rib spacing. Rallabandi et al. [11, 12] investigated the spacing effect on the square channel with 45° angled ribs ($\frac{e}{D_h}$ = 0.1-0.2, Re = 30,000-400,000) with sharp edges and as well as rounded edges. They studied three different ratios of rib pitch to rib height (P/e) ranging between 5-10. The result showed that the reduction of ribs-to-ribs spacing enhances the heat transfer enhancement of the channel due to increased available heat transfer area. Additionally, reduction

of rib spacing results in more ribs which cause more secondary flow in case of angled ribs. The secondary flow intensifies the circulation of the coolant between the ribs. Consequently, heat transfer enhancement keeps increasing as the *P*/*e* ratio [13] decreases. However, the resultant high heat transfer enhancement due to the reduction in rib spacing is also accompanied by a large pressure drop.

Alkhamis et al. [14] studied V-shaped ribs (α = 45° and $\frac{e}{D_h}$ = 0.1-0.18) in a square channel for a wide range of Re = 30,000-400,000. They experimented with *P*/*e* in the range of 5 to 10. Wright et al. [15] also investigated the V-shaped and W-shaped ribs (α = 45° and $\frac{e}{D_h}$ = 0.078, *P*/*e* = 10) in a rectangular channel (AR = 4) for Re = 10,000-40,000. In both studies, the comparative heat transfer performance results with parallel 45° ribs demonstrated that both V-shaped and W-shaped ribs possess higher heat transfer capacity than conventional parallel angled ribs due to the increased number of additional secondary flow structures caused by V and W-shaped ribs. In the rectangular channel, a substantial spanwise variation in heat transfer distribution has also been observed for conventional angled ribs. V and W shaped ribs help to reduce this spanwise variation of heat transfer too. Han and Zhang [16] studied the effect of the discretization of the ribs on the heat transfer and pressure drop behavior of a square channel. They investigated continuous and discrete (broken) parallel ribs at an angle of 90°, 60°, and 45°, and continuous and broken V ribs with 60° and 45° angle. Their results also confirmed that the V-shaped ribs' performance is superior to the parallel angled ribs. Moreover, broken V ribs have higher performance than the continuous V ribs, which concludes that the discretization of the ribs has a good chance to enhance the heat transfer augmentation. It is conjectured that discretization creates even more additional secondary flow

structures than those caused by continuous V ribs. Valentino et al. [17] studied the thermal performance of symmetric (full) and non-symmetric (half) wedge turbulators in a rectangular channel (AR = 2). Their results show that the non-symmetric wedges resulted in a higher reduction of both heat transfer augmentation and friction augmentation than the symmetric wedge cases. All studies mentioned above showed that the heat transfer coefficient rises when the Re increases, but the heat transfer augmentation reduces or remains almost same for increasing Reynolds number. In other words, the advantage of applying ribs decays at higher Reynolds numbers. Conversely, the friction augmentation caused by the ribbed channel increases with Reynolds number. Most of the studies in the literature were conducted at lower Re (< 70,000). Rallabandi et al. [11] studied the heat transfer and friction behavior in a square channel with 45° ribs at a wide range of Re = 30,000-400,000. They varied the blockage ratio $\frac{e}{D_h}$ in the range between 0.1 and 0.18. Their data do not agree with the earlier published correlations proposed by Han et al. [18]. Therefore, they proposed new correlations for their experimented range. Note that the old correlations by Han et al. [18] were based on $0.048 < \frac{e}{D_h} < 0.078$ and $10 < P/e < 20$, and Re< 70,000.

The cooling channels inside the turbine airfoils are not always of a rectangular shape. The leading-edge cooling channels can be modeled as a triangular channel. The leading edge has the highest thermal load due to the presence of a stagnation point. Taslim et al. [19] and Domaschke et al. [20] have investigated the heat transfer and pressure drop behavior in a leading-edge channel. They measured heat transfer behavior in a leading-edge cavity like a duct roughened with 45° ribs ($\frac{e}{D_h}$ =

0.1, Re = 20000-50000) using Transient Liquid Crystal (TLC) technique. They also analyzed the flow behavior of such channels numerically by using the SST turbulence model.

Most of the research on turbulated internal duct cooling focus on the single straight channel. Some studies are performed on multi-pass passages. For instance, Lei et al. [21] and Huh et al. [22] investigated heat transfer behavior in a square two pass channels with 45° ribs. Smith et al. [23] studied thermal performance in a three-pass serpentine channel. Their investigation was performed with 45° angled ribs with varying aspect ratio of the channel (AR = 1, 1/2, 1/6; $\frac{e}{D_h}$ = 0.1 to 0.058, Re = 4,000-130,000). Their results depict that the maximum heat transfer augmentation happens in AR = 1/6 when Re ≥ 50,000. Rallabandi et al. [24] and Yang et al. [25] also studied the heat transfer characteristics in a three-pass serpentine channel. They also performed the investigation with 45° ribs with varying AR of the channel.

The above mentioned research indicate that the performance of a turbulated channel is affected by different parameters such as $\frac{e}{D_h}$, P/e, Re, number of ribbed walls, the configuration of the ribs and the aspect ratio of the channel, etc. Any variation of these parameters causes a difference in the flow behavior as well as the heat transfer capability and friction of the channel. Experimental investigation of each turbulated channel is expensive both in terms of time and cost. Numerical simulation is a good and effective alternative. Therefore, several researchers tried to investigate heat transfer and friction behavior of a ribbed channel numerically, especially with RANS (Reynolds Average Navier Strokes) turbulence models. For instance, Acharya et al. [26] studied the flow as well as the heat transfer behavior in a channel with a rectangular cross section with

transverse ribs. They used non-linear and standard *k*-ε turbulence models for their investigation. They observed that both turbulence models failed to detect the recirculation zone just behind the ribs. Rigby et al. [27] numerically studied the heat transfer behavior in a square channel with transverse ribs and bleed holes using *k*-ω turbulence models and found reasonable agreement with the experimental data. Jang et al. [28] investigated both rotating and stationary straight channel with 45° ribs ($\frac{e}{D_h}$ = 0.1) by Reynolds stress turbulence model. The summary of the studies conducted on the different parameters of the ribbed internal duct cooling channels is shown in Table 1.

Table 1 Summary of the studies on the internal duct cooling channel with ribs

Authors	Year	Channel AR	Re	Ribs angle	Ribs cross-section	No. of the ribbed	No. of passes	$\frac{e}{D_h}$	P/e	Rotating effect	Heat transfer exp	Friction exp	Flow field exp	CFD
Han et al. [18]	1984	1	8k-80k	15°-90°	Square	2	1	0.048-0.078	10,20	-	Uniform heat flux	Yes	-	-
Han et al. [4]	1985	1	8k-80k	15°-90°	Square	2	1	0.093	10,20	-	Uniform heat flux	Yes	-	-
Han [3]	1988	1/4,1/2, 1,2, and 4	10k-60k	90°	Square	2	1	0.047, 0.078	10,20	-	Uniform heat flux	Yes	-	-
Han and Park [5]	1988	1,2, and 4	10k-60k	30°-90°	Square	2	1	0.047, 0.078	10,20	-	Uniform heat flux	Yes	-	-
Han and Zhang [16]	1991	1	15k-90k	30°-90° V	Square	2	1	0.0625	10	-	Uniform heat flux	Yes	-	-

Authors	Year	Channel AR	Re	Ribs angle	Ribs cross-section	No. of the ribbed	No. of passes	$\frac{e}{D_h}$	P/e	Rotating effect	Heat transfer exp	Friction exp	Flow field exp	CFD
Park et al. [6]	1992	1/4,1/2, 1,2, and 4	10k-60k	30°-90°	Square	2	1	0.047, 0.078	10	-	Uniform heat flux	Yes		
Ekkad and Han [29]	1997	1	6k-60k	V (90° and 60°)	Square	1	2	0.125	10	-	TLC	-	-	-
Taslim and Lengkong [30]	1998	1	10k-50k	45°	Square	2	1	0.133, 0.167, and 0.25	5,8.5, 10	-	Yes HTC on rib surfaces	Yes	-	-
Taslim et al. [9]	1998	1 and trapezoidal	5k-30k	45°	Square and round	2,3, 4	1	0.22	8.5,9.1 ,7.99	-	TLC	Yes	-	-

Authors	Year	Channel AR	Re	Ribs angle	Ribs cross-section	No. of the ribbed	No. of passes	$\frac{e}{D_h}$	P/e	Rotating effect	Heat transfer exp	Friction exp	Flow field exp	CFD
Wright et al. [15]	2001	4	10k-60k	45° V and W shaped	Square	2	1	0.078	10	Yes	Uniform heat flux	Yes	-	-
Bailey and Bunker [8]	2003	2.5	20k-100k	45°	Square and round	2	1	0.193-0.333	10	-	TLC	Yes	-	-
Acharya et al. [26]	2004	4.9	U_{ref} = 3.6 m/s	90°	Square	1	1	0.063	20	-	Uniform heat flux	-	LDV	(nonlinear k-ε), FDI
Liu et al. [13]	2006	2	5k-40k	45°	Square	2	2	0.094	10,7.5, 5,3	Yes	Uniform heat flux	Yes	-	-

Authors	Year	Channel AR	Re	Ribs angle	Ribs cross-section	No. of the ribbed	No. of passes	$\frac{e}{D_h}$	P/e	Rotating effect	Heat transfer exp	Friction exp	Flow field exp	CFD
Rallabndi et al. [11]	2010	1	30k - 400k	45°	Square	2	1	0.1,0.15 ,0.18	5,7.5, 10	-	Uniform heat flux	Yes	-	-
Alkhamis et al. [14]	2011	1	30k-400k	45° V shaped	Square	2	1	0.1-0.018	5, 7.5,10		Uniform heat flux	Yes	-	-
Domaschke et al. [20]	2012	Leading edge cavity	20k-50k	45°		2	1	0.1	10	-	TLC	Yes	-	SST, FDI
Lei et al. [21]	2012	2	10k-40k	45°	Square	2	2	0.098	5,7.5, 10	Yes	Uniform heat flux		-	-
Smith et al. [23]	2013	1,1/2, 1/6	50k	45°	Square	2	3	0.058-0.1	10	Yes	Uniform wall temperature	Yes	-	-

Authors	Year	Channel AR	Re	Ribs angle	Ribs cross-section	No. of the ribbed	No. of passes	$\frac{e}{D_h}$	P/e	Rotating effect	Heat transfer exp	Friction exp	Flow field exp	CFD
Rallabandi et al. [24]	2014	trapezoidal	75k-165k	45°	Square	2	3	0.081-0.133	10	Yes	Uniform heat flux	Yes	-	-
Current study	2018	1	6k-135k	45°	Square and rounded edge	1, 2	1	0.0625	10	-	Uniform wall temperature	Yes	PIV	LES, RANS (RKE, v^2-f, SST k-ω), FDI

Study on Rounded-Edged Ribs

Due to manufacturing constraints, the gas turbine industry faces a challenge to make the sharp-edged ribs, which often results in rounded edge ribs. Therefore, it is essential to study the consequence of the rounded edged ribs on the heat transfer and pressure drop. Taslim and Lengkong [7] studied the effect of rounding the top edges of the ribs on the heat transfer and friction behavior in a square channel. Their study was done for three different high blockage ratio ribs ($\frac{e}{D_h}$ = 0.25, 0.167 and 0.133; P/e = 5-10, 45° ribs) for Re = 10,000 to 50,000. They found that rounded edge ribs reduce both heat transfer and friction factor than those of sharp-edged ribs. The reduction of heat transfer and friction factor lessens with the decrease in blockage ratio. However, the rounded edged ribs cause a higher amount of reduction in pressure drop than the reduction in heat transfer for all the cases. For example, the rounded edge ribs cause 17.5% to 12% lower heat transfer, but 41% to 15% lower pressure drop compared to the sharp ribs for $\frac{e}{D_h}$ = 0.25. Jang et al. [28] used Chimera RANS model to study the heat transfer as well as the flow behavior in a duct with 45° ribs of round cross-section (AR = 1, $\frac{e}{D_h}$ = 0.1, P/e = 10, Re = 25,000) with different rotation number. Rallabandi et al. [12] also studied the effect of all edges filleted 45° ribs on the heat transfer and friction behavior in a square channel. Their investigation was also conducted for high blockage ratio ribs ($\frac{e}{D_h}$ = 0.0944 - 0.188; P/e = 5-10) but in a wide range of Re values (30,000-400,000). They also reported that rounding the edges of the ribs do not have a significant effect on the heat transfer coefficient. However, rounded edge ribs caused lower pressure drop compared to the sharp-edged ribs, especially with the taller ribs. They anticipated that the reduced recirculation

zone at the base of the rounded edge ribs caused the reduction in the local pressure loss. These studies indicate that the round ribs have a great potential for better thermal performance. However, all these investigations were performed at the high blockage ratio ribbed channels (tall ribs). To the best of our knowledge, no study was performed to see the effect of rounding edges with low blockage ratio ribs. A new study on the low blockage ratio ribbed channel (smaller ribs) may offer an interesting insight. Additionally, the studies on the round ribs were limited to the heat transfer and pressure drop mainly. To understand the effect of the rounded edge ribs on the heat transfer distribution properly, comprehension of its flow behavior is very important. Table 2 shows the summary of the research done on the ribs with a rounded edge.

The current study examines the effect of rounded-edged ribs on the heat transfer and friction behavior in a low blockage ratio ($\frac{e}{D_h}$ = 0.0625, ribs on two walls applied in parallel fashion) 45° ribbed channel. To achieve this, both sharp and rounded edge ribs (all other parameters same) were studied in a wide range of Re both experimentally and numerically. Three different turbulence models, namely SSST k-ω, Realizable k-ε (RKE) and v^2-f turbulence models were used. To understand the effect of the rounded edge ribs on the heat transfer distribution properly, a detail comparative flow field study between the sharp and round ribs was performed using numerical results.

Table 2 Summary of the work on rounded-edged ribs

Authors	Year	Channel AR	Re	Ribs Angle	Fillet on the ribs	No of the ribbed walls	e/D_h	P/e	Experiment	CFD
Taslim and Lengkong [7]	1999	1	10,000-50,000	45°	Top edges	2	0.25, 0.167, 0.133	5-10	Average heat transfer and pressure drop	No
Jang et al. [28]	2000	1	25,000	45°	Top and bottom edges	2	0.1	10	-	Yes, Chimera RANS
Rallabandi et al. [12]	2011	1	30,000-400,000	45°	Top and bottom edges	2	0.0944 - 0.188	5-10	Average heat transfer and pressure drop	No
Current study	2018	1	6,000-135,000	45°	Top and bottom edges	2	0.0625	10	Average heat transfer and pressure drop	Yes, RANS

Flow Behavior Investigation in Internal Duct Cooling Channels

Thermal performance of different kinds of turbulators is an active area of research. Many researchers have performed experiments and produced a volume of data which help the gas turbine industry to move forward. Compared to that, few researchers have investigated the complex three-dimensional turbulent flow fields in a ribbed channel. The flow field is very complicated due to the presence of flow separation and reattachment, secondary flows and bends, centrifugal buoyancy forces, and the Coriolis effect due to the rotation, etc. These factors make the flow prediction very difficult. Some researchers have tried to understand the flow physics experimentally by using some advanced technologies such as Hot Wire Anemometry (HWA), Particle Image Velocimetry (PIV), and Laser Doppler Velocimetry (LDV), etc. For example, Rau et al. [31] studied the detailed heat transfer and aerodynamic behavior of a square channel with transverse ribs ($\frac{e}{D_h}$ = 0.1, P/e = 6, 9, 12, AR = 1, one and two ribbed walls) using LDV and TLC at Re = 30,000. The results showed that the flow inside a turbulated channel, especially near the ribs is very complex, unsteady, turbulent, and highly three dimensional. This complex flow field results in uneven heat transfer distributions within the channel.

The major drawback of HWA and LDV method is that these techniques only provide velocity measurements at a point. Unlike the HWA and LDV, PIV provides the flow field data in a plane of interest which makes the PIV a better tool to comprehend the flow physics in such turbulated channels. For instance, Son et al. [32] determined flow field in a square, two passes, smooth and 90° ribbed ($\frac{e}{D_h}$ = 0.125 and P/e = 10) channel at Re = 30,000 using planer PIV. They correlated

their flow field data with a previously conducted heat transfer study [29]. The result shows the wall heat transfer enhancement highly is influenced by the secondary flow characteristics, such as shape, strength, the direction of the rotation, and the position of the vortex. Casarsa and Arts [33] also used the planer PIV technique to investigate the flow field inside a square channel with high blockage transverse ribs ($\frac{e}{D_h}$ = 0.3) installed on one wall (Re = 40,000). They established a quantitative correlation between the aerodynamic results with previously studied heat transfer data for high blockage ration channel. Liou et al. [34] investigated the flow field inside a parallelogram-shaped two pass channels with transverse ribs. They used planer 2D PIV for their study. Gao and Sundén [35, 36] studied flow field of a rectangular duct (AR = 8) with various rib configuration, such as inclined ribs with the various angle of attack (30°- 45°), crossed and V-shaped ribs with α = 60° at Re ≈ 5800. They measured the local flow structure between the ribs, but a detailed turbulence data was not reported in the inter-rib space. They found that the rib orientation angle highly influences the style and strength of the secondary flow for inclined ribs, and 45° ribs produce the strongest secondary flow (two cells) between all the inclined ribs.

Schabacker et al. [37] used stereoscopic PIV technique to investigate the effect of the bend in a two-pass internal cooling channel roughened with 45° ribs ($\frac{e}{D_h}$ = 0.1, P/e = 10) at Re = 45,700. Chanteloup et al. [38] used PIV to determine the flow field data in a two-pass channel with 45˚ ribs ($\frac{e}{D_h}$ = 0.1, P/e = 10, staggered) on two walls (Re = 50,000). They used stereoscopic PIV to determine all the three mean velocity components in several planes to determine how the main and secondary flow characteristics influence heat transfer. No turbulence data, e.g., turbulent kinetic

energy, Reynolds normal and shear stresses are reported in this study. Due to the light reflections, the results at the vicinity of the wall in the inter-rib space could not be captured too.

Most of the experimental flow behavior studies reported on the transverse ribs. There are very few studies conducted in a channel with angled ribs. It is very challenging to measure the flow field data in the inter-rib space for a channel with angled ribs due to the obstruction caused by the ribs. There is a great need for high fidelity experimental data in the inter-rib space for an angled ribbed channel which can be used for CFD validation, especially for LES. The current study measures the detailed flow field data in the inter-rib space in a square channel with 45° ribs using stereoscopic PIV technique. The results of mean velocity components, turbulent kinetic energy, and all the Reynolds stresses are presented. The investigation was done in a wide range or Re = 10,000-150,000. An LES study at Re ≈ 30k was also performed and validated with the experimental stereo PIV results which is discussed in chapter 7.

Table 3: Summary of the flow investigations in the ribbed channel using PIV

Authors	Year	Channel AR	Re	Ribs Angle	No. of ribbed walls	$\frac{e}{D_h}$	P/e	Measurement techniques
Son et al. [32]	2002	1	30,000	90°	1	0.125	10	Planer PIV
Chanteloup et al. [38]	2002	1	50,000	45°	2	0.1	10	Stereo PIV
Gao and Sundén [35, 36]	2004	8	5800	30°, 45°, 60°, 90° (Round cross section-ribs)	2	0.06	10	Planer PIV
Casarsa and Arts [33]	2005	1	40,000	90°	1	0.1	10	Planer PIV
Coletti [39]	2012	0.9	15,000	90°	1	0.1	10	Planer PIV
Liuo et al. [34]	2015	Parallelogram	10,000	90°	2	$e/H = 0.1$	10	Planer PIV
Current study	2018	1	10,000-150,000	45°	1	0.0625	10	Stereoscopic PIV

LES Work on Internal Duct Cooling Channels

With the exponential increase in computational power in the last few decades, Direct Numerical Simulations (DNS) and Large Eddy Simulations (LES) are also being used to investigate the complex flow field inside of a ribbed channel. For example, Burattini et al. [40] and Leonardi et al. [41] performed DNS in a channel with transverse ribs. Orlandi and Leonardi [42] investigated two and three-dimensional roughness elements using DNS. Till date, DNS is prohibitively expensive at high Re. Researchers rely on LES for higher accuracy (than RANS) which has much lower computational expenses than DNS.

Tyacke [43] studied flow and heat transfer behavior in a square duct with a 180° bend (transverse ribs, $\frac{e}{D_h}$ = 0.1, P/e = 10) at Re = 20,000. They used LES and hybrid RANS–LES methods for their study. A comparison was conducted with experimental data and found a good match. They concluded that the choice of the LES does not matter since the large scales dominates the flow mainly. The inlet turbulence is found to have a little effect as the ribs generate very strong turbulence in the flow.

Kubacki et al. [44] conducted a flow study in a rotating rectangular channel with transverse ribs at Re = 15,000. The flow is simulated with periodic assumption and the computational domain consists of two streamwise periods. They used both hybrid RANS/LES and basic RANS k-ω model to determine its capability in reproducing the flow structures in such channel. Comparing with the experimental results, they found that the hybrid RANS/LES k-ω model reproduce the flow field in

a rotating ribbed channel precisely. However, the modified *k-ω* model for frame rotation also predicts the mean velocity profiles in the midplane of the channel well. However, it does not predict the fluctuations and the secondary vortices result well.

Patil and Tafti [45] conducted LES of flow and heat transfer in a square ribbed duct with transverse ribs of $\frac{e}{D_h}$ = 0.1 and 0.05 and P/e = 10 and 20. Their investigated Re were 20,000 and 60,000. The computational methodology assumes a periodic fully developed flow and heat transfer and hence the computation domain contained only one pitch. They compared their wall modeled LES results with the previously conducted wall-resolved LES data and some other available data. They found a good match between the experimental results and LES. Both of the wall modeled and wall-resolved LES showed similar accuracy at the higher Re. However, the wall modeled LES lessens the computational difficulties significantly than the wall-resolved LES.

O Labbé [46] conducted an LES study of turbulent flow and heat transfer in a duct roughened with transverse ribs ($\frac{e}{D_h}$ = 0.3, P/e = 10, AR = 1) at Re = 40,000. They performed two simulations. The first one was full domain consists of five ribs and the second one was with the periodic interface in streamwise direction with one rib. Both the simulations show excellent match with the experimental results of recirculation zones and the center plane mean velocities. However, the LES results obtained in the periodic domain case shows a better match with experimental results than the one with the full domain. One possibility of this discrepancy might be the inlet boundary conditions, which do not represent the experiments.

Kang and Yang [47] studied the effect of the rib spacing (P/e) on turbulent heat transfer in a circular ribbed-pipe flow using LES (with dynamic subgrid model). The ribs were of $\frac{e}{D_h}$ = 0.0625 and the P/e varied 2, 4, 6, 8, 10 and 18. The investigation was performed at Re = 24,000.

Sewall et al. [48] examined the prediction capability of LES for reproducing the experimental data of heat transfer and flow behavior in a 2-pass square duct with transverse ribs ($\frac{e}{D_h}$ = 0.1, P/e = 10) at Re = 20,000. The three calculations domains used, i) developing flow region (eight ribs) ii) Fully developed flow model (one rib- periodic fully developed flow) iii) 180˚ bend. They reported that the LES predicts the flow physics accurately within 10% - 15% of experiments.

Tyagi and Acharya [49] investigated aerothermal behavior in a ribbed (α = 90˚, $\frac{e}{D_h}$ = 0.1, P/e =10) channel (AR = 1) at Re = 12,500 using LES with rotating condition. They used the periodic boundary condition in streamwise direction for the simulation. Their computation domain contains two inter-rib space/pitches. Most of the LES studies reported with the periodic Fully Developed Interface (FDI) used constant heat flux boundary conditions because of the high computational cost associated with the isothermal wall boundary condition. Since isothermal wall conditions represent the turbine blade wall temperatures better, they applied isothermal wall conditions for the simulation by using a newly proposed noniterative method which makes it cost effective. There are many other LES work done with the transverse ribbed channel. Watanabe and Takahashi [50] and Tafti [51] also investigated the heat transfer and aerodynamic behavior with LES for a transverse ribbed channel. Cui et al. [52] investigated turbulent flow behavior in a square channel

with d and k-type transverse ribs at Re ≈ 10,000 based on the bulk velocity and half of the channel's height.

Dritselis [53] performed an LES investigation in a channel with transverse turbulators of various cross-sections (square, triangular, circular) applied on one wall at a very low Re = 5,600. The investigator evaluated the feasibility of different subgrid-scale models by comparing the results with DNS generated results [54, 41, 42]. The results showed that all the mentioned subgrid-scale models predict the main flow physics with fidelity and exhibit similar performances.

Wahab and Tafti [55] investigated flow and heat transfer behavior in a ribbed duct (α = 45°, $\frac{e}{D_h}$ =0.1, P/e = 10, Re ≈ 47,000). The ribs were applied on two opposite walls in a staggered fashion. They used the dynamic Smagorinsky subgrid model for the simulation. Their results showed good compliance with the experimental results.

Jia et al. [56] studied the heat transfer behavior of the upstream and downstream pointing V-shaped ribs using v^2-f (α = 45˚, $\frac{e}{D_h}$ = 0.0625 and 0.125, Re = 4,000 to 32,000), as well as LES (α =60˚, $\frac{e}{D_h}$ = 0.0625 and 0.125, Re = 4,000). The simulations were done with the fully developed periodic condition in a streamwise direction which allowed the computation domain of one pitch length.

There are many LES studies for flow and heat transfer behavior investigation in internal duct cooling channels; most of the these are performed with transverse ribs. A recent review paper by Holgate et al. [57] summarizes the LES studies done for internal flows till date. Only a handful

LES studies are performed for a channel with angled ribs, especially with 45° ribs. There is a great need to investigate the prediction capability of LES for angled ribbed channels. One of the primary objectives of the present study is to conduct an LES study of aerothermal behavior in a square channel with 45° ribs ($\frac{e}{D_h}$ = 0.0625, P/e = 10) applied on one wall at Re ≈ 30,000. The LES results were validated with the experimental data obtained with stereoscopic PIV. Besides LES, RANS simulations with different turbulence models were also conducted and compared with the experimental results as well as LES to evaluate the prediction capability of RANS models in such turbulated channels.

CHAPTER 2: RESEARCH OBJECTIVES

Objectives of the Present Study

One of the main objectives of the current study is to provide a detailed understanding of the heat transfer and pressure drop behavior in a square internal duct cooling channel roughened with 45° ribs and the flow physics associated with it. The application of an internal duct cooling channel with 45° ribs is one of the most common cooling techniques in the gas turbines. It is found that the angled ribs result in a highly non-homogenous heat transfer distribution. The heat transfer distribution is directly affected by the complex turbulent flow inside the channel. Therefore, comprehension of the flow physics is essential for characterizing the heat transfer behavior in such channels properly. In the current study, both sharp and rounded-edge ribs have been studied. The investigations were conducted in a combination of both experimental and numerical approaches. Research shows that only a handful of LES studies have been performed for a channel with angled ribs, especially with 45° ribs. The present study determines the suitability of LES for predicting aerothermal behavior in a square channel with 45° ribs. The prediction capability of different turbulence models was also evaluated. Additionally, the flow field data acquisition in the inter-rib space for a channel with angled ribs is very challenging due to the obstruction caused by the ribs. There is a great need for high fidelity experimental data in the inter-rib space for an angled ribbed channel which can be used for CFD validation, especially for LES. The current study provides the flow field data in the inter-rib space in a 45° ribbed duct using stereoscopic PIV technique.

The following approaches were applied to study the above mentioned problems.

- Experimental heat transfer and pressure drop investigation in a square channel with 45° ribs at a wide range of Re (6,000-135,000).

  The investigations were conducted in three different configurations. Those are- A) Sharp-edged ribs on two opposite walls, B) Rounded-edged ribs on two opposite walls, and C) Sharp-edged ribs on one wall.

- RANS simulations using three different turbulence models- a) Realizable k-ε (RKE), b) v^2-f, and c) SST k-ω for both sharp and round ribs of two ribbed wall cases.

  The results of each turbulence model are compared with the experimental heat transfer and friction data to shed light on the prediction capability of these models for both types of the ribs at the wide range of Re (6,000-135,000).

- To produce the benchmarking experimental flow field data in the inter-rib space in a 45° ribbed duct by using stereoscopic PIV.

  The experiment was conducted at the streamwise midplane of the one ribbed wall case. The investigations were done at different Re, ranging from 10,000 to 150,000.

- To conduct LES as well as RANS simulations for the one ribbed wall case at Re ≈ 30,000.

The LES and RANS results are compared with the experimental flow field and heat transfer data. A detail discussion of the aerothermal behavior of the sharp ribs is conducted using the LES results.

- Comparative aerothermal behavior study between the sharp and rounded-edged ribs. The investigation was done using the results obtained by the v^2-f turbulence model at Re ≈ 52,000.

Novelty

The present study provides a detailed understanding of the flow physics on the heat transfer and pressure drop behavior in 45° ribbed channels both with sharp and rounded-edged ribs. Both numerical and experimental approaches were implemented for the investigation. The effect of the rounded-edged ribs on heat transfer and pressure drop behavior in a low blockage ratio ($\frac{e}{D_h}$ = 0.0625) channel is studied. The current study presents a detail comparative aerodynamic results between the sharp and rounded-edge ribs. A detailed discussion is done to correlate the aerodynamic behavior with the wall heat transfer distribution for both kinds of the ribs.

To measure the detail flow field data in the inter-rib space for a channel with angled ribs is very challenging due to the obstacles caused by them. In the literature, there is not enough PIV flow field data in the inter-rib space for an angled ribbed channel which can be used for CFD validation, especially for LES. The current study provides benchmarking flow field data in the inter-rib space in a square channel with 45° ribs using stereoscopic PIV technique. The investigation was done in

a wide range of Re = 10,000-150,000. A large eddy simulation was also performed for the aerothermal behavior investigation in a 45° ribbed channel at Re ≈ 30,000. The LES results are compared with the experimental flow and heat transfer results to determine its prediction capability in a 45° ribbed channel. The LES results show excellent agreement with the experimental data. The prediction capability of different RANS turbulence models was also evaluated by comparing their results with the experiment as well as the LES.

Research Impact

This research focuses on the importance to comprehend the secondary flow physics to characterize the heat transfer distribution in the internal duct cooling channels with angled ribs. Due to manufacturing constraints, gas turbine industry has the challenge to make perfectly sharp ribs, often the ribs' edges become filleted. This research highlights the comparative effect of the sharp and rounded edge ribs on the aerodynamic behavior and the consequent effect on the heat transfer distribution on the walls. This study produces benchmarking stereo PIV data very close to the ribbed wall in a 45° ribbed channel which can be used for CFD validation as well. With the recent improvement in computational capacity, CFD is used as investigation tool for different types of turbulated channels. RANS simulations are widely used due to its lower computational cost with a compromise of accuracy. LES show very good prediction capability of aerothermal behavior in ribbed cooling channels especially with transverse ribs. The current study evaluates the prediction capability of LES as well as different RANS turbulence models by comparing the results with the experimental flow field and heat transfer data in a 45° ribbed duct. The results focus on the high accuracy of the LES in predicting the aero-thermal behavior. However, the prediction capability

of different RANS models is found to be inconsistent for the different configurations and the flow conditions (Re). This study emphasizes the potential of LES for predicting the aerothermal characteristics in an angled ribbed channel with high accuracy, which can be leveraged to study turbulated internal cooling more reliably.

CHAPTER 3: INVESTIGATION TECHNIQUES

Particle Image Velocimetry

Particle image velocimetry is a nonintrusive instantaneous flow field measurement procedure. Unlike the HWA and LDV, PIV provides the instantaneous flow field data in a plane of interest. The mean velocity maps can also be achieved by using the PIV generated instantaneous velocity data. For PIV measurements, the flow is homogeneously entrained with small tracer particles (diameter 0.5–5μm) so that the tracer particles faithfully follow the flow motion. The ratio between the response time of particle and the integral time scale of the flow (Stokes number) requires to be very low for the particles to track the flow motion with high fidelity. Therefore, the tracer particles need to be very small to have a low Stokes number. On the contrary, the particle size must be large enough to scatter an adequate amount of light for being identified by the CCD camera. A combination of lenses and a high-power Nd: YAG laser are used to generate the light sheet to illuminate the seeded fluid. Then the entrained fluid is illuminated twice in short succession and an image pair of particle patterns are recorded by using a CCD camera. The displacement field of the seeding particles is estimated using the cross-correlation of the image pairs in the interrogation area. Finally, the velocity vector field is determined from the displacement field and the time interval between the successive image pairs.

The traditional 2-dimensional-2C (two components) PIV method can provide only the projection of a velocity vector in the measurement plane. The 2D-2C is incapable of estimating the out of plane velocity component. For highly three-dimensional flow such as turbulent flow in a ribbed

channel, this unmeasured out of plane component can result in a substantial error in the measured in-plane components with a non-orthogonal camera and the measurement plane arrangement. Stereoscopic PIV can measure all 3-components of velocity in the measurement plane. In this arrangement, two cameras are placed at two different viewing direction to acquire projections of the velocity vectors in two planes. Then, using the combination of these two 2D-2C vector fields, the 2D-3C (all three velocity components) PIV velocity vector field is reconstructed. A calibration of the camera system is essential to determine the viewing directions of both cameras with respect to the orientation of the light sheet. Calibration also helps to rectify for the image distortion in the lenses and the plexiglass walls of the duct.

Reynolds Averaged Navier-Stokes Equation (RANS)

The equations of instantaneous motion of an incompressible fluid are as follows [58]

$$\frac{\partial u_i}{\partial x_i} = 0 \tag{1}$$

$$\frac{\partial u_i}{\partial t} + u_j \frac{\partial u_i}{\partial x_j} = f_i - \frac{1}{\rho}\frac{\partial p}{\partial x_i} + \vartheta \frac{\partial^2 u_i}{\partial x_j \partial x_j} \tag{2}$$

The velocity u_i is decomposed into a mean flow $\overline{u_i}$ and velocity fluctuation u_i' such that

$$u_i = \overline{u_i} + u_i' \tag{3}$$

Where,

$$\overline{u_i} = \frac{\mathbf{1}}{\Delta \boldsymbol{t}} \int_0^{\Delta t} u_i(t)dt \tag{4}$$

The time average of the fluctuating components is zero.

$$\overline{u_i'} = \frac{\mathbf{1}}{\Delta \boldsymbol{t}} \int_0^{\Delta t} u_i'(t)dt = 0 \tag{5}$$

The pressure and other variables are also decomposed into mean and fluctuating components.

Applying these decompositions, the equations for mean flow are obtained [58].

$$\frac{\partial \bar{u}_i}{\partial x_i} = 0 \tag{6}$$

$$\bar{u}_j \frac{\partial \bar{u}_i}{\partial x_j} = \bar{f}_i + \frac{1}{\rho}\frac{\partial}{\partial x_j}\left[-\bar{p}\delta_{ij} + \mu\left(\frac{\partial \bar{u}_i}{\partial x_j} + \frac{\partial \bar{u}_j}{\partial x_i}\right) - \rho\overline{u_i' u_j'}\right] \tag{7}$$

This equation also can be written as,

$$\bar{u}_j \frac{\partial \bar{u}_i}{\partial x_j} = \bar{f}_i + \frac{1}{\rho}\frac{\partial}{\partial x_j}\left[-\bar{p}\delta_{ij} + 2\mu\bar{S}_{ij} - \rho\overline{u_i' u_j'}\right] \tag{8}$$

Where, $\bar{S}_{ij} = \frac{1}{2}\left(\frac{\partial \bar{u}_i}{\partial x_j} + \frac{\partial \bar{u}_j}{\partial x_i}\right)$

These equations are known as Reynolds Averaged Navier-Stokes (RANS) equations. The additional terms $\left(\rho\overline{u_i' u_j'}\right)$ which have evolved in the mean momentum equation are known as the Reynolds stresses. To solve these equations, the nonlinear Reynolds stress terms involve additional modeling for closure. Different turbulence models have been developed to close the RANS equation. These models are categorized into two main types, namely 1) Eddy viscosity models (EVM), and 2) Reynolds stress model (RSM).

Eddy Viscosity Models (EVM)

In this method, the Reynolds stress terms are modeled using the Boussinesq hypothesis. This hypothesis assumes that the turbulent Reynolds stress terms are proportional to the mean velocity gradient similar to the viscous stresses.

The viscous stresses are proportional to the rate of deformation of the fluid element.

$$\tau_{ij} = \mu\left(\frac{\partial \bar{u}_i}{\partial x_j} + \frac{\partial \bar{u}_j}{\partial x_i}\right) \tag{9}$$

Joseph Boussinesq introduced the concept of turbulent eddy viscosity ν_t and correlated the Reynolds stresses and the deformation rate of the fluid element using it [59].

$$-\overline{u_i' u_j'} = \nu_t \left(\frac{\partial \overline{u}_i}{\partial x_j} + \frac{\partial \overline{u}_j}{\partial x_i} \right) - \frac{2}{3} k \delta_{ij} \tag{10}$$

where,

ν_t = turbulent eddy viscosity

$k = -\frac{1}{2}\overline{u_i' u_i'}$ = turbulent kinetic energy

δ_{ij} is the Kronecker delta.

The ν_t is calculated using a single length and velocity scale. There are several models established based on the Boussinesq hypothesis which are known as eddy viscosity models or EVM's, such as, *k*-*ε*, *k*-*ω*, Mixing Length Model and Zero Equation Model, etc. The models are often called by the number of transport equations associated with them. For example, the *k*-*ε* is referred to as a "Two Equation" model as it solves two transport equations (one for *k* and one for ε). The major drawback of EVM models is that it assumes an isotropic turbulent viscosity which is not often realistic.

k-*ε* Turbulence Model

The *k*-*ε* turbulence model is the most common two equation EVM model. The first transport equation this model solves is for turbulent kinetic energy (*k*) in the flow. The turbulent kinetic energy is used to determine the velocity scale. The second transport equation is for the turbulent dissipation (*ε*) of the turbulent kinetic energy which is used to determine the length scale. The turbulent viscosity μ_t is modeled as,

$$\mu_t = \rho C_\mu \frac{k^2}{\epsilon} \tag{11}$$

The transport equations for k and ε are as following [60].

$$\frac{Dk}{Dt} \approx \frac{\partial}{\partial x_j}\left[\frac{\vartheta_t}{\sigma_k}\frac{\partial k}{\partial x_j}\right] + \vartheta_t \frac{\partial \bar{u}_i}{\partial x_j}\left(\frac{\partial \bar{u}_i}{\partial x_j} + \frac{\partial \bar{u}_j}{\partial x_i}\right) - \varepsilon \tag{12}$$

$$\frac{D\varepsilon}{Dt} \approx \frac{\partial}{\partial x_j}\left[\frac{\vartheta_t}{\sigma_\varepsilon}\frac{\partial \varepsilon}{\partial x_j}\right] + C_1 \vartheta_t \frac{\varepsilon}{k}\frac{\partial \bar{u}_i}{\partial x_j}\left(\frac{\partial \bar{u}_i}{\partial x_j} + \frac{\partial \bar{u}_j}{\partial x_i}\right) - C_2 \frac{\varepsilon^2}{k} \tag{13}$$

$C_\mu, C_1, C_2, \sigma_k, \sigma_\varepsilon$= empirical constants

Since molecular viscosity and sublayer damping effects are not considered in the model, this model is well suited only for predicting the outer and overlap layer.

Realizable *k*-*ε* Turbulence Model (RKE)

The standard *k*-*ε* model is unsuitable for resolving the flow region very close to the wall since it is developed based on turbulent core flows. The Realizable *k*-*ε* model is a variant of the standard *k*-*ε* model. It applies an improved method for calculating turbulent viscosity. It also incorporates a new transport equation for the dissipation rate which is formulated using an exact equation for the transport of the mean-square vorticity fluctuation. This model exhibits better prediction capability than the standard *k*-*ε* model for boundary layers under strong adverse pressure gradients, flows involving rotation, separation, and recirculation [61].

k-*ω* Turbulence Model

The *k*-*ω* turbulence model is another two-equation model developed by Wilcox and Rubesin et al. [62]. This model solves the transport equations for k and ω, where k and ω denote the turbulent

kinetic energy and the specific rate of dissipation, respectively. The length and velocity scales of the turbulence is evaluated using the ω and k, respectively. The prediction capability of the k-ω model is very good for simulating the flow in the viscous sublayer.

SST (Shear Stress Transport) k-ω Turbulence Model

The standard k-ω model can resolve flow through the boundary layer. SST k-ω is a hybrid model that combines the k-ω turbulence model and k-ε turbulence model. This model ensures that the appropriate model is used in every part of the flow field (k-ω in the wall region and the k-ε away from the wall) [61].

v^2-f Turbulence Model

The v^2-f model is similar to the standard k-ε model but solves two additional transport equations. This model includes some near-wall turbulence anisotropy as well as non-local pressure-strain effects. Hence, it should be capable of predicting the near wall turbulence more accurately. Researchers have recommended this model for simulating flows which are highly dominated by separation [63].

Large Eddy Simulation (LES)

Turbulent flow involves an ample range of time and length scales which makes the numerical simulation of turbulent flows solving the Navier–Stokes equations very difficult. Only Direct Numerical Simulation resolves all the scales which is computationally very expensive and

currently impractical for real-world problems. On the other hand, RANS based turbulence models do not resolve any of the length scales. It does not first compute the full time-dependent flow field to calculate the mean flow. Instead, it models the effect of all the scales on the mean flow motion which reduces the computational cost greatly.

In the LES technique, a low pass filtering operation of the Navier-Stokes equations is executed to remove the smallest scales of the flow. Only the large-scales of the flow are solved and the subgrid scale (SGS) models are used to model the effect of the removed small scales. In this way, LES reduces the computational expense incurred by the smallest scales. Thus, LES is much more computationally expensive than RANS but is remarkably economical than DNS. The classical motivation for LES is that the modeling large scales is problem dependent and difficult since the boundary conditions directly affect the largest eddies. They carry most of the Reynolds stresses and are anisotropic in behavior. It is easier to model smaller scales as they have less contribution to the turbulent Reynolds stresses and are universal and isotropic in nature.

Governing Equations

In LES, the filtering operation in Navier Stokes equations decomposes the velocity field (u_i) into a resolved ($\overline{U}_i$) and sub-grid part (u_i'). The resolved part and the subgrid part represent the "large" eddies and small scales, respectively. The effect of the subgrid part on the resolved field is included through the SGS models [59].

$$u_i(\mathrm{x},\mathrm{t}) = \overline{U}_i(\mathrm{x},\mathrm{t}) + u_i'(x,t) \tag{14}$$

The filtered continuity and momentum equations are as follows [59].

$$\frac{\partial \overline{U_i}}{\partial x_i} = 0 \tag{15}$$

$$\frac{\partial \overline{U_i}}{\partial t} + \frac{\partial \overline{U_i}\,\overline{U_J}}{\partial x_j} = -\frac{1}{\rho}\frac{\partial \bar{P}}{\partial x_i} + \vartheta \frac{\partial^2 \overline{U_i}}{\partial x_j \partial x_j} - \frac{1}{\rho}\frac{\partial \tau_{ij}}{\partial x_j} \tag{16}$$

The term τ_{ij} is residual (SGS) stress tensor and requires to be modeled for the closure of the equations. Subgrid-scale turbulence models generally use the Boussinesq hypothesis to determine the SGS stress using the following equation [59].

$$\tau_{ij} = -2\mu_{SGS}\overline{S_{ij}} \tag{17}$$

where μ_{SGS} is the SGS turbulent viscosity. Substituting into the filtered Navier-Stokes equations,

$$\frac{\partial \overline{U_i}}{\partial t} + \frac{\partial \overline{U_i}\,\overline{U_J}}{\partial x_j} = -\frac{1}{\rho}\frac{\partial \bar{P}}{\partial x_i} + \frac{\partial}{\partial x_j}\left[|\vartheta + \vartheta_{SGS}|\frac{\partial \overline{u_i}}{\partial x_j}\right] \tag{18}$$

The formulation of ϑ_{SGS} depends on the applied SGS models. In the case of the Smagorinsky (1963) model (classical LES model): $\mu_{SGS} = (C_s\Delta)^2\sqrt{S_{ij}S_{ij}}$ where Δ is a measure of the grid spacing of the numerical mesh, $S_{ij} = \frac{1}{2}\left(\frac{\partial u_i}{\partial x_j} + \frac{\partial u_j}{\partial x_i}\right)$ and C_s is a constant.

One of the downsides of the eddy viscosity SGS model is that it assumes constant C_s which is not ideal. The coefficient C_s depends on flow behavior. Additionally, the Smagorinsky model does not permit the negative C_s value; therefore it does not allow energy backscatter. These drawbacks were addressed in the dynamic Smagorinsky model in which C_s is calculated dynamically as the solution progresses and allows energy backscatter [64].

The Adapting Local Eddy-viscosity (WALE) subgrid model [65] is an improvement of the Smagorinsky model. Both strain rate and the rotation rate effect of the smallest resolved turbulence

fluctuations is considered in this model. The subgrid-scale viscosity is calculated in the following method [65].

$$\mu_{SGS} = C_w \Delta^2 \rho \frac{OP1}{OP2} \tag{19}$$

$$OP1 = \left(S_{ij}^d S_{ij}^d\right)^{1.5} \tag{20}$$

$$OP2 = \left(S_{ij}^d S_{ij}^d\right)^{2.5} + \left(S_{ij}^d S_{ij}^d\right)^{1.25} \tag{21}$$

$$S_{ij}^d = \frac{1}{2}\left(\bar{g}_{ij}{}^2 + \bar{g}_{ji}{}^2\right) - \frac{1}{3}\delta_{ij}\bar{g}_{kk}^2 \tag{22}$$

$$\bar{g}_{ij} = \frac{\partial \bar{U}_i}{\partial x_j} \tag{23}$$

The WALE SGS model was used for the current study.

Periodic Fully Developed Flow

The formulation for periodic fully developed flow and heat transfer have been described by Patankar et al. [66]. They developed the equations for fully developed flow and heat transfer for a duct with the periodic cross-sectional area in the streamwise direction. For their analysis, they considered a two dimensional or axisymmetric duct flows with *x* as the streamwise coordinate and *y* as the wall normal coordinate. Let *L* is the period of the variation.

The velocity field for the periodic fully developed regime is as follows.

$$u(x, y) = u(x + L, y) = u(x + 2L, y) = \cdots \tag{24}$$

$$v(x, y) = v(x + L, y) = v(x + 2L, y) = \cdots \tag{25}$$

Periodicity condition for pressure:

$$p(x, y) - p(x + L, y) = p(x + L, y) - p(x + 2L, y) = \cdots \tag{26}$$

$$\frac{p(x,y)-p(x+L,y)}{L} = \beta \quad (27)$$

The pressure field can be expressed as:

$$p(x,y) = -\beta x + P(x,y) \quad (28)$$

The βx term is associated with the global mass flow. $P(x,y)$ is associated to the detail local motions and periodic in nature.

$$P(x,y) = P(x+L,y) = P(x+2L,y) = \cdots \quad (29)$$

The β term acts as a source term in the momentum equation in the *x* direction.

Periodic Fully Developed Heat Transfer

The periodic fully developed temperature depends on the thermal boundary condition a) Uniform heat flux, b) Uniform wall temperature.

Uniform Heat Flux

For the thermally fully developed region in a duct with uniform heat flux can be characterized as the following equations.

$$\frac{\partial T}{\partial x} = constant \quad (30)$$

$$T(x+L,y) - T(L,y) = T(x+2L,y) - T(x+L,y) = \cdots \quad (31)$$

The temperature field can be expressed as:

$$\frac{T(x+L,y)-T(x,y)}{L} = \gamma \quad (32)$$

The constant γ can be determined by the following equation.

$$\gamma = \frac{Q}{\dot{m} C_p L} \tag{33}$$

where Q is the heat rate per unit span in the fluid over the period L. The temperature field can be divided into two parts.

$$T(x,y) = \gamma x + \mathcal{T}(x,y) \tag{34}$$

$$\mathcal{T}(x,y) = \mathcal{T}(x+L,y) = \mathcal{T}(x+2L,y) = \cdots \tag{35}$$

Uniform Wall Temperature

For the thermally fully developed region in a duct with uniform wall temperature can be characterized as following equations.

$$\frac{T(x,y)-T_w}{T_{bx}-T_w} = f(y) \tag{36}$$

$$\frac{d(T_{bx}-T_w)/dx}{T_{bx}-T_w} = \text{constant} \tag{37}$$

where, T_{bx} denotes the local bulk temperature. The non-dimensional temperature can be defined as the following equation.

$$\theta(x,y) = \frac{T(x,y)-T_w}{T_{bx}-T_w} \tag{38}$$

$$T_{bx} - T_w = \frac{\int_{y_1}^{y_2} (T-T_\infty)|u|dy}{\int_{y_1}^{y_2} |u|dy} \tag{39}$$

The periodicity condition for θ:

$$\theta(x,y) = \theta(x+L,y) = \theta(x+2L,y) = \cdots \tag{40}$$

The energy equation (not shown here) in terms of θ shows that the λ is also periodic.

$$\lambda(x) = \frac{dT_{bx}/dx}{T_{bx}-T_w} = \frac{d(T_{bx}-T_w)/dx}{T_{bx}-T_w} \tag{41}$$

$$\lambda(x) = \lambda(x + L) = \lambda(x + 2L) = \cdots \tag{42}$$

The presence of the unknown function $\lambda(x)$ complicates the solution. It requires an iterative method to determine θ and λ. The λ needs to be such that the resultant θ holds the equation below.

$$\int_{y_1}^{y_2} \theta|u|\, dy = \int_{y_1}^{y_2} |u|\, dy \tag{43}$$

CHAPTER 4: EXPERIMENTAL SETUP

Heat Transfer and Pressure Drop Investigation

The average heat transfer and friction behavior of a square channel with 45˚ ribs were studied at a wide range of Re (6,000-135,000). The investigations were conducted in three different configurations. Those are- a) Sharp-edged ribs on two opposite walls, b) Rounded-edge ribs on two opposite walls, and c) Sharp-edged ribs on one wall. The preliminary results of these studies were published in references [67, 68, 69]. The details of the experiments are described in the following sections.

Experimental Setup and Procedure

The ratio of rib height to channel hydraulic diameter ($\frac{e}{D_h}$) and the ratio of pitch to rib height (P/e) were 0.0625 and 10, respectively for all the configurations. The test sections had a square cross section ($AR = 1$). The channel height and width were equal to 2 inches (0.0508 m) and hence, the hydraulic diameter was 2 inches (0.0508 m) as well. The channels were made of four 43.85 inches (1.114 m) long continuous aluminum plates, and the length of the channel was ~ $22D_h$. Figure 4 shows the schematic diagram of the test section with two opposite ribbed walls. The ribs of the two opposite walls were arranged in parallel fashion, while the side walls were kept smooth. Figure 5 shows the cross-section of the one ribbed wall case. The bottom wall was roughened with the ribs while the other walls were kept smooth. All other arrangements were the same for all the three cases. A thin strip of cork was used to separate the adjacent walls which helped to reduce heat conduction between two adjacent walls.

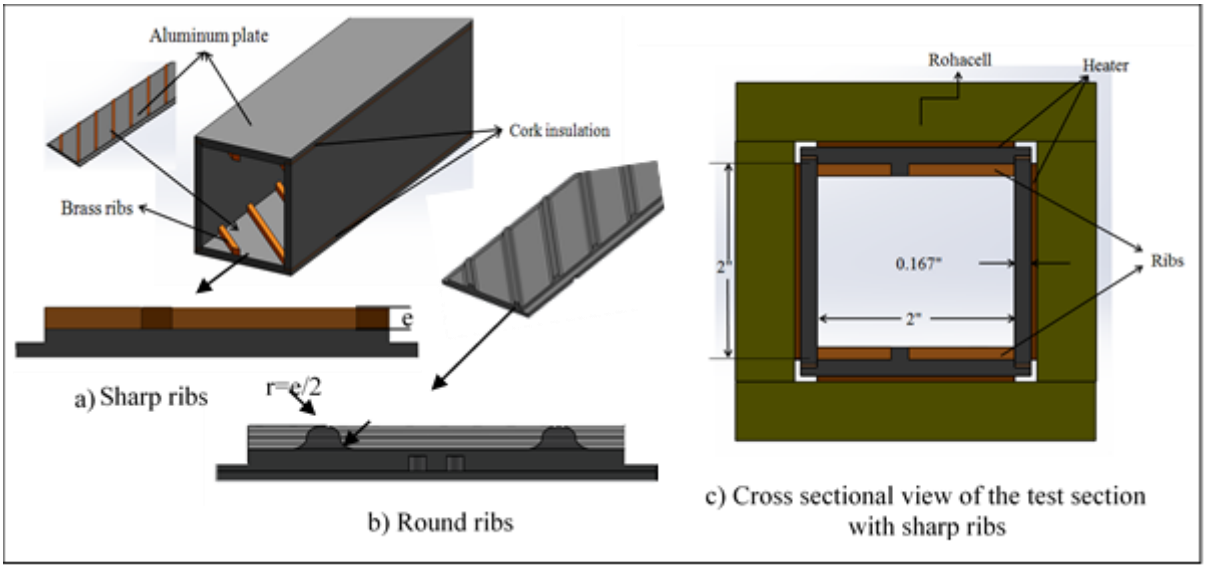

Figure 4 Schematic diagram of the test section (a) Sharp ribs (b) Round ribs (c) Cross sectional view of the two ribbed wall case

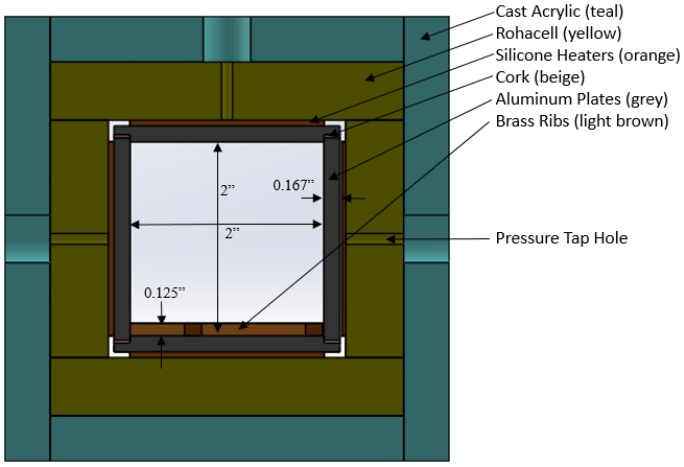

Figure 5 Cross-sectional view of the one ribbed wall case

The ribs were of a square cross section with a height (*e*) of 0.125 inches (0.003175 m) and spaced 1.25 inches (0.03175 m) from the next rib resulting in a pitch-to-height ratio (*P*/*e*) of 10.

Hereinafter, the sharp and rounded-edge ribs are referred to as, sharp and round ribs, respectively. Figure 4 shows the rib features for both sharp and round cases. The fillet radius of the round ribs is equal to half of the rib height (e/2). The experimental setup and procedures for all the cases were identical, except that in the cases (both two wall study and one wall study) of sharp ribs, brass ribs were bonded on the aluminum plates with LOCTITE 384 Adhesive. For the round ribs case, the ribs were machined directly from the aluminum base plate.

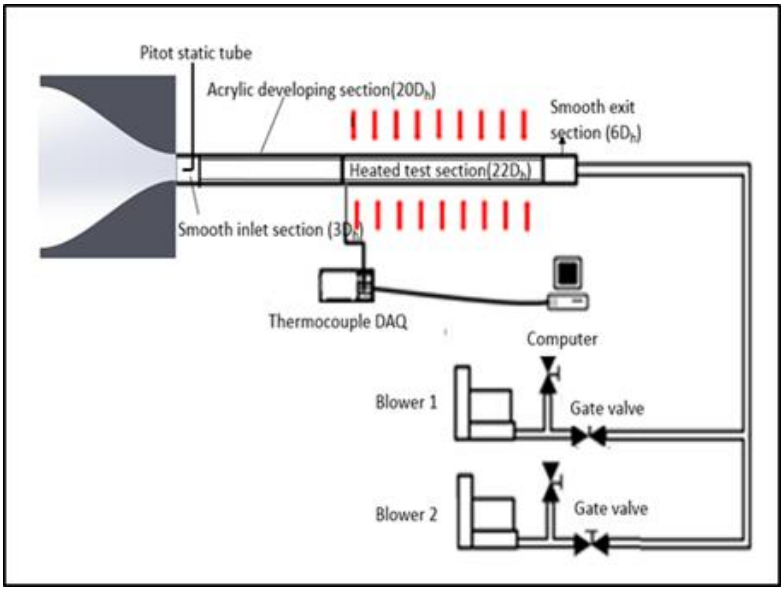

Figure 6 Experimental layout for heat transfer test

Figure 4 (c) and Figure 5 shows the cross section of the test sections. The aluminum test section was surrounded by four Rohacell walls for insulation. Rohacell is a good insulating material, which has very low thermal conductivity (~ 0.03W/m-K). The entire test section with the Rohacell walls was placed in an acrylic outer housing to support the structure of the rig. Figure 6 shows the schematic diagram of the heat transfer test setup. An acrylic $20D_h$ long entrance section was used

to ensure hydro-dynamically fully developed flow before entering the heated section. The interior of the entrance section was the same as that of the test section. There was a contraction (8:1) nozzle followed by a $3D_h$ smooth inlet section prior to the ribbed entrance section. Additionally, there was a $6D_h$ long smooth exit section which helps to prevent backflow effects in the test section. To measure the average velocity U_b of the flow, a pitot static tube was placed in the middle of the channel's cross section at $1D_h$ downstream from the contraction nozzle. This velocity measurement was used to determine the mass flow rate and Reynolds number using the following two equations.

$$\dot{m} = \rho_{air} A_c U_b \tag{44}$$

$$\mathrm{Re} = \frac{U_b D_h}{\vartheta} \tag{45}$$

For heat transfer tests, the four walls of the test section were maintained at isothermal conditions (within ±1˚C). To achieve isothermal conditions on the aluminum plate surfaces, 14 etched foil heaters (3.1in×2 in) were attached to the outer surface of each aluminum plate with double-sided Kapton® tape. There was a small gap ~ 0.1 inch (~ 2.5 mm) between the heaters to accommodate the pressure taps. Each heater location contained two thermocouples inserted into machined holes from the outer side of the aluminum plate to measure the wall temperature under the heater. The thermocouple holes were placed at the center of each heater locations. The ends of the thermocouple holes were ~ 1mm from the flow surface of the aluminum plate. The thermocouples were held in place with high conductivity thermal cement. The schematic diagram for the heater arrangement is shown in Figure 7. The location of the thermocouples is listed in Table 4. The voltage applied to each heater or heater group was controlled individually by using a rheostat and variac. For this purpose, a total of thirty six rheostats and ten variacs were used. Each individually controlled heater/heater group will be referred to as a module hereinafter. There were nine modules

per wall or 36 (= 9×4) for four walls in total. Additionally, two thermocouples were placed at the inlet and exit of the test section to measure the inlet and exit bulk air temperature. This measured exit bulk air temperature was used to cross-check the thermal energy balance of the system.

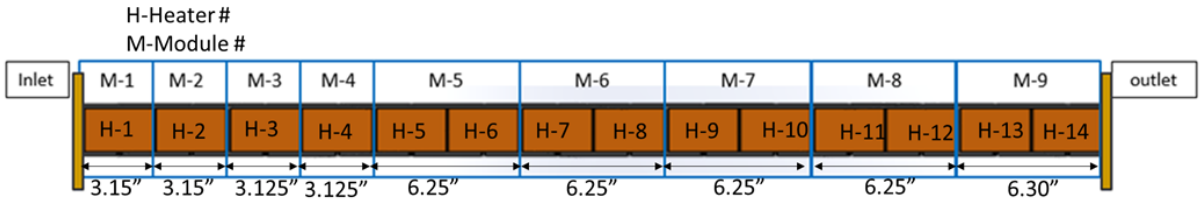

Dimensions are in inches

Figure 7 Schematic diagram of the heaters arrangement

Table 4 Thermocouple locations from the inlet of the aluminum test section

Heater #	1	2	3	4	5	6	7
TC locations, in	1.53	4.63	7.78	10.88	14.03	17.13	20.28
Heater #	8	9	10	11	12	13.	14
TC locations, in	23.38	26.53	29.63	32.78	35.88	39.03	42.13

Heat Leakage Test

The amount of heat leakage to the surroundings from each module was determined by separate experiments, namely heat leakage tests. The heat leakage tests were performed under a no-flow condition. Some insulation material was inserted into the inlet and outlet sections to prevent air flow. The heat was supplied by the heaters to maintain all the wall’s temperature at a specific value. After reaching steady state, the temperature, voltage, and resistance of each module were recorded. Three different wall temperatures were tested. A linear curve fit for heat leakage to the

surroundings from each module as a function of temperature difference between wall and ambient was constructed by using these data. Additionally, another linear curve fit of resistance as a function of wall temperature was also established.

$$Q_{leakage_x} = \frac{V_x^2}{R_x} = fn\left(T_{w_x} - T_{amb}\right) \quad (46)$$

$$R_x = fn(T_{w_x}) \quad (47)$$

Here, *x* denotes a module number.

During the heat leakage test, all the walls of the channel were maintained at an isothermal condition and were insulated from all the sides. At steady state, the air and wall temperatures should be equal which makes the possibility of natural convection inside the channel negligible.

Heat Transfer Test

Heat transfer tests began with setting up the flow rate to obtain the desired Re. Two Spencer VB110 vortex blowers were used to draw the air flow from the ambient. The blowers were connected in parallel fashion and operated under suction. The tests were conducted at nine different Re in the range from 6,000 to 135,000. The Re mentioned here is based on the hydraulic diameter of the channel and the bulk velocity of the channel. The test matrix for the heat transfer tests is shown in Table 5. Heat supplied to each module was individually regulated by variacs and rheostats to attain an isothermal wall temperature throughout the channel walls. After the modules reached steady state, the temperature and voltage of each module were recorded.

Table 5 Test matrix for heat transfer test

Number of ribbed walls	Ribs type	Nominal Re								
Two	Sharp ribs	6k	20k	30k	50k	55k	65k	90k	118k	134k
	Round ribs	6k	26k	36k	51k	66k	75k	90k	120k	143k
One	Sharp ribs	-	23k	45k	57k	69k	84k	97k	106k	-

Friction Test

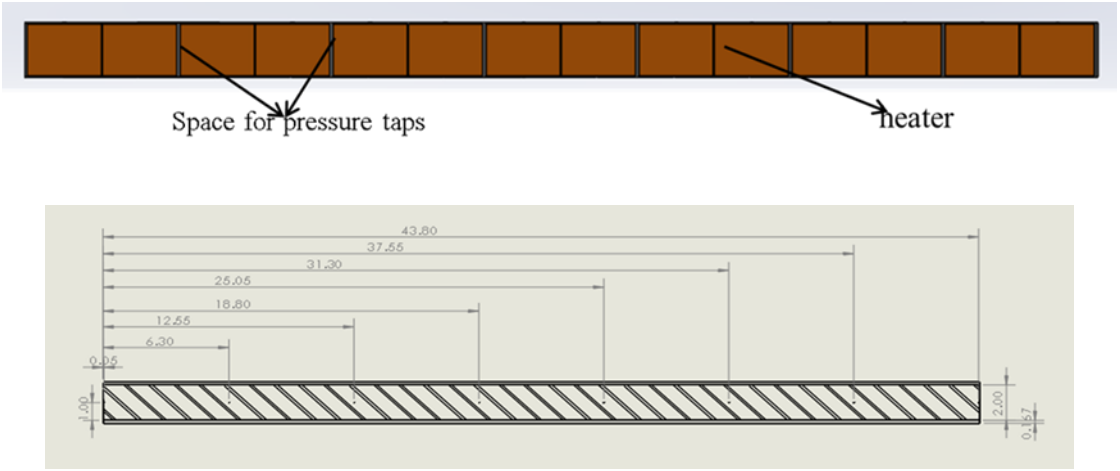

All dimensions are in inches

Figure 8 Location of the pressure taps

Friction tests were conducted under unheated conditions. Eight equally spaced pressure taps were implemented on each of the left, right, and top walls (8 pressure taps on each wall, for a total of 24 pressure taps) of the test section. As mentioned earlier, there was a small gap between the heaters to place the pressure taps.

The schematic diagram for the pressure taps locations is shown in Figure 8. The streamwise distances for the pressure taps from the inlet of the test section were the same for all the three walls. The pressure tap locations are tabulated in Table 6. Additionally, there were 14 more pressure taps on the right-side wall of the acrylic developing section (which are not shown here). The pressure distribution of this section was monitored to ensure that the flow becomes hydrodynamically fully developed before it reaches to the metallic test section. The static pressure at all these locations was measured by a Scanivalve, which is a mechanically multiplexed pressure transducer. The friction tests were performed for several Re ranging from 6,000-150,000.

Table 6 Pressure tap locations from the entrance of the aluminum test section

Pressure tap #	1	2	3	4	5	6	7	8
Locations, inch	0.05	6.30	12.55	18.80	25.05	31.30	37.55	43.80

Data Reduction

To determine the regional /module average heat transfer results, first, the amount of heat supplied to the module was calculated using the following equation.

$$Q_{input_x} = \frac{V_x^2}{R_x} \tag{48}$$

where *x* denotes a module number (starts from 1), V and R are the voltage and resistance for the module, respectively. Resistance of each module, R_x was determined by the resistance curve fit equation for the measured wall temperature.

The actual heat supplied was calculated by subtracting the amount of heat leakage from the supplied heat to the module, as shown in the following equation.

$$Q_{actual_x} = Q_{input_x} - Q_{leakage_x} \tag{49}$$

$Q_{leakage_x}$ was calculated from the heat leakage curve fit for measured temperature differences between the aluminum wall and ambient. Since the walls were maintained at isothermal conditions, lateral heat conduction between the modules was disregarded.

The bulk temperature of the air at the end of each module in the channel was determined using a bulk temperature marching starting from the inlet using an energy balance.

$$T_{f_x} = \frac{\sum_{walls} Q_{actual_x}}{\dot{m} C_p} + T_{f_{x-1}} \tag{50}$$

where, T_{f_0} is the recorded inlet fluid temperature.

Module-average heat transfer coefficient can be calculated as follows using the bulk temperature of the air at the beginning and the end of each module, wall temperature and the actual heat supplied to the flow at each module.

$$h_x = \frac{Q_{actual_x}}{A_x (LMTD_x)} \tag{51}$$

$$LMTD_x = \frac{(T_{w_x} - T_{f_{x-1}}) - (T_{w_x} - T_{f_x})}{ln \frac{(T_{w_x} - T_{f_{x-1}})}{(T_{w_x} - T_{f_x})}} \tag{52}$$

where, A_x is the projected area of the module.

The module/regional average Nusselt and friction factor *f* were calculated by using the following equations.

$$\mathrm{Nu_x} = \frac{h_x D_h}{k_{air}} \tag{53}$$

$$f = \frac{\frac{\Delta P}{\Delta Z} D_h}{0.5\, \rho_{air} {U_b}^2} \tag{54}$$

The relative benefit of the heat transfer enhancement to the increase in pumping power (due to the ribs application) is indicated by thermal performance. The following equations [70, 71] were used to calculate the thermal performance.

$$\eta = \frac{(\mathrm{Nu}/\mathrm{Nu}_0)}{(f/f_0)^{1/3}} \tag{55}$$

where, Nu_0 and f_0 are the smooth channel Nusselt number and friction factor, respectively. Nu_0 was determined by the Dittus-Boelter correlation as follows.

$$\mathrm{Nu}_0 = 0.023 Re^{0.8} Pr^{0.4} \tag{56}$$

f_0 was determined by the Blasius correlation.

$$f_0 = \frac{0.316}{(Re)^{0.25}} \tag{57}$$

Uncertainty Estimates in Heat Transfer and Pressure Drop Measurement

Experimental uncertainties have been estimated by the methods described in ASME PTC 19.1-2005 [72], Kline and McClintock [73] and Moffat [74]. All the uncertainties are calculated for 95% confidence level. The uncertainty in Re measurement is estimated to be less than 4% in all cases at Re ≥ 10k. The uncertainty in velocity measurement by the pitot static tube contributes primarily to the uncertainty calculation of the Re. The relative uncertainty in bulk velocity calculation is higher at the lowest tested Re ≈ 6k which causes higher uncertainty ~ 7.5% in the resulted Re as well.

Uncertainties in parameters such as voltages, resistances, temperatures, and mass flow rate measurements are the main contributors to the Nu uncertainty. Unlike the round ribs case, the sharp ribs were made of brass and glued to the aluminum plates in this experiment. In this case,

the contact resistance caused by the adhesive layer (Loctite 384, $k \sim 0.76$ W/m.K) can cause a bias uncertainty in the measured Nu. The effect of the contact resistance has been quantified by the order-of-magnitude analysis as shown in Rallabandi et al. [12]. The thickness of the adhesive layer is assumed as ~ 0.1 mm for this calculation. The highest Re (or the highest HTC) case has the maximum uncertainty due to this effect (~ 2% higher for the both two and one ribbed wall cases). For this reason, the sharp ribs case has higher measurement uncertainty for ribbed wall Nu than the round ribs case. The maximum uncertainty quantified for ribbed wall Nu in the sharp case is ~ 6% at the highest Re for both two walls and one wall cases. The uncertainty in Nu for the smooth walls or ribbed wall for the round case have lower measurement uncertainty. The maximum uncertainty in ribbed wall Nu for round ribs ~ 4.5% the lowest Re ≈ 6k. The other Re shows 3.6% - 3.9% uncertainty in the ribbed wall Nu of the round ribs case. The uncertainty in Nu of the smooth walls is less than ~ 3.3% and ~ 4% for two wall sharp and round ribs, respectively at Re ≥ 20,000. The uncertainty in smooth wall Nu for the two ribbed wall study is higher (~ 5.3%) at Re ≈ 6k. The uncertainty in Nu of the smooth wall and the top wall of the one wall study is less than ~ 3.8% and ~ 5.5%, respectively.

The uncertainty in pressure and the average velocity measurements are the dominant contributors to the friction factor uncertainty estimation, which is less than 7% for Re ≥ 20,000. The uncertainty in the friction factor is as high as ~ 15% for the lower range of Re values (i.e., 6,000 ≤ Re ≤ 20,000). The uncertainty tress for Re, friction factor and Nu are shown in the Appendix A.

Turbulent Flow Investigation Using Stereo PIV

The detail flow field for the one ribbed wall case was investigated using PIV. The PIV measurements were conducted at a fully developed flow region for multiple Re in the range of Re = 10,000-150,000. To confirm the flow is fully developed, the investigation was done on and between three ribs starting after 54 ribs at the streamwise midplane ($\frac{X}{W}$ = 0.5) up to $\frac{Y}{D_h}$ = 0.4 of the channel.

(a)

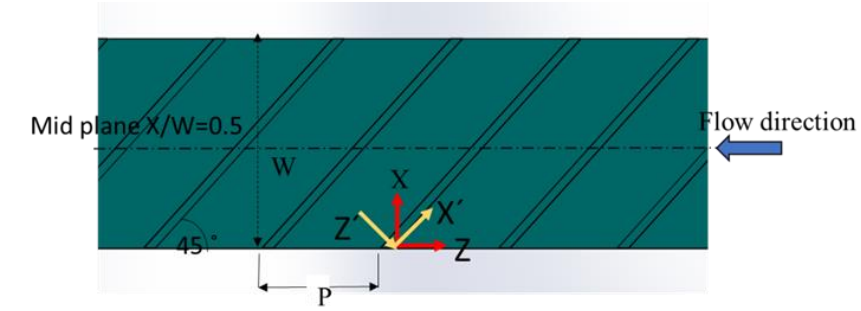

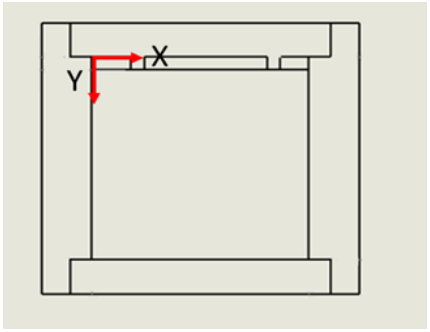

(b)

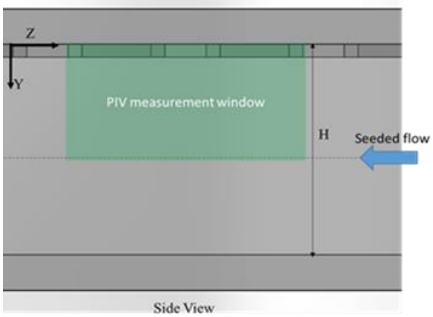

(c)

Figure 9 (a)-(b) Coordinate system of PIV test (c) PIV test window

The coordinate system for the PIV tests is shown in Figure 9. Stereoscopic (2D-3C) PIV was used for the investigation. Stereo PIV can determine all the three velocity components as well as all the six Reynolds stresses. Table 7 shows the test matrix of the PIV tests.

Table 7 Test matrix for PIV test

Nominal Re	10k	30k	50k	70k	100k	150k
Actual Re	10171	29089	535489	68836	105943	145503

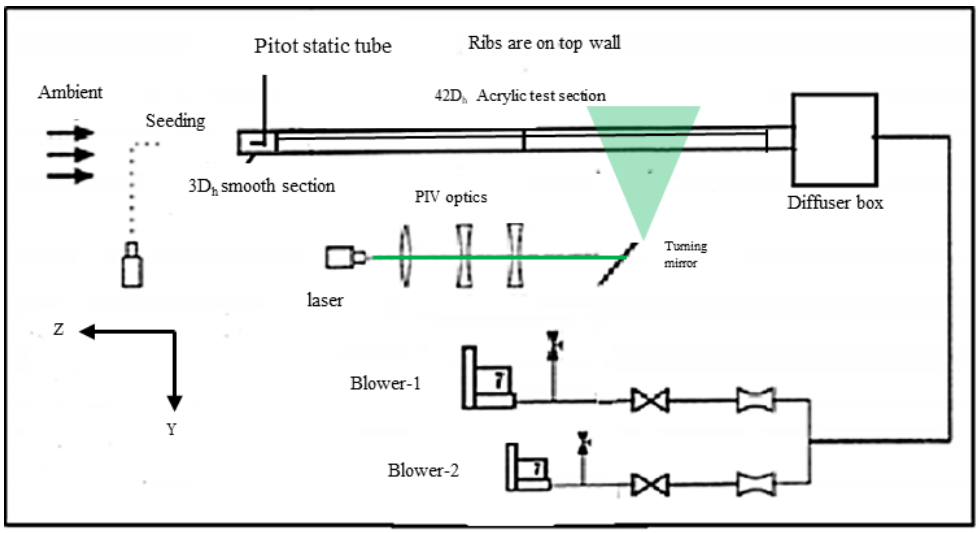

Figure 10 Schematic of the PIV rig set up

The PIV experiments were conducted in an open-circuit turbulent channel-flow facility. The setup used for the current study is a modification of the previously used heat transfer and friction experiment. The experimental setup had a $22D_h$ metallic section for heat transfer tests. Additional $20D_h$ long entrance Polymethyl methacrylate PMMA (commercially known as Plexiglass) section

was used to ensure hydro-dynamically fully developed flow before entering the heated section. The interior of the entrance section was the same as that of the test section. For PIV tests, the heated section was replaced by another similar PMMA section. The ribbed wall was placed at the top to allow the laser light sheet to go through the bottom wall without any disturbance. Figure 10 shows the modified open loop wind tunnel for the current flow investigation.

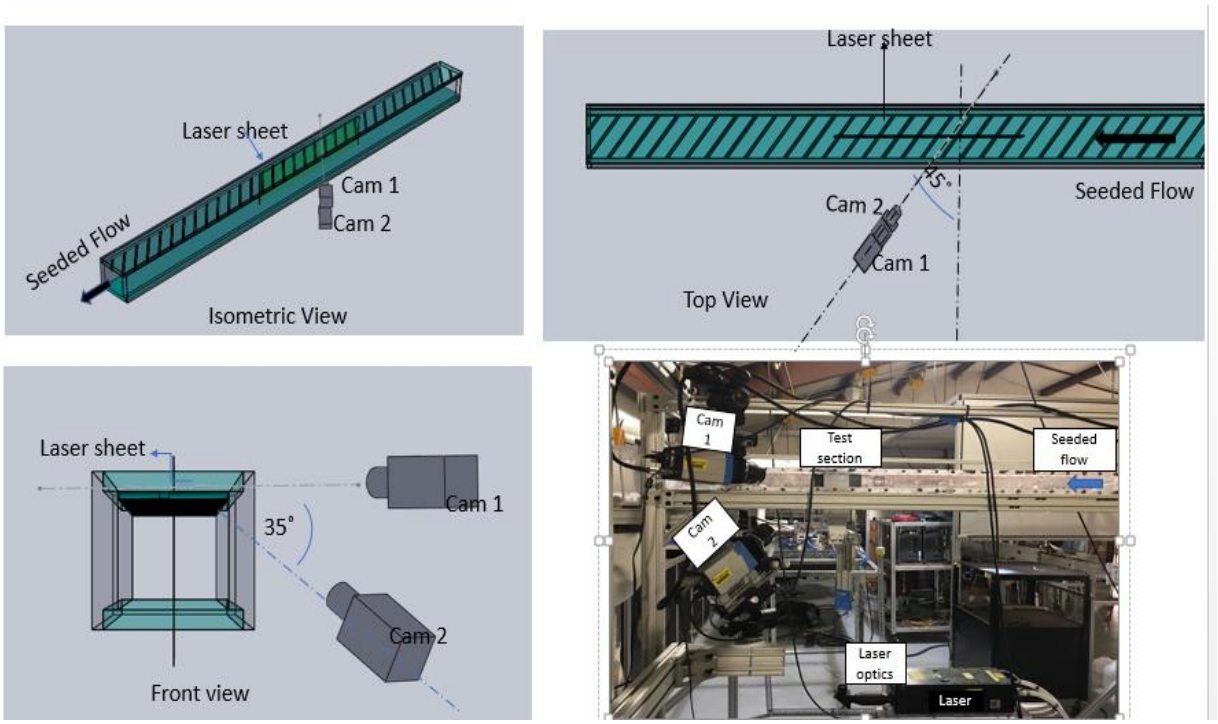

Figure 11 Schematic of stereoscopic PIV setup

Ambient air was drawn through the test section using two Spencer VB110 vortex blowers. The blowers were connected in parallel fashion and operated under suction. A $3D_h$ long smooth channel was connected before the developing section. A pitot static tube is installed at channel center and

at a $1D_h$ axial distance from inlet to calculate the bulk velocity in the channel using measured dynamic pressure. The tests were conducted at seven different Re ranging from 10,000 to 150,000.

The arrangement for stereo PIV measurement is shown in Figure 11. The imaging system uses two Andor Zyla CMOS 5.5-megapixel cameras. Due to the oblique ribs at 45˚, both cameras were placed with an oblique angle of ~ 45˚ from the light sheet normal. The two cameras were placed with ~35˚ angle between them. A 55 mm camera lens was used for each camera. The Scheimpflug adapter on each camera was adjusted in such a way that both cameras focused across the entire plane. A careful adjustment of the magnification and the camera-to-measurement plane distance allowed us to obtain a resultant particle image size of ~ 2-3 pixels. A calibration of the camera system was performed to determine the viewing directions of both cameras with respect to the light sheet, as well as the real-world scaling in the measurement location. Calibration is also useful to rectify the image distortion in the lenses and the plexiglass passage walls. For this purpose, a LaVision dual plane calibration plate was used for the calibration as shown in Figure 12. Unlike the common flat calibration targets, it does not need to take several views in the out-of-plane-direction; only a single view from one target location is adequate for the calibration of the stereo set up.

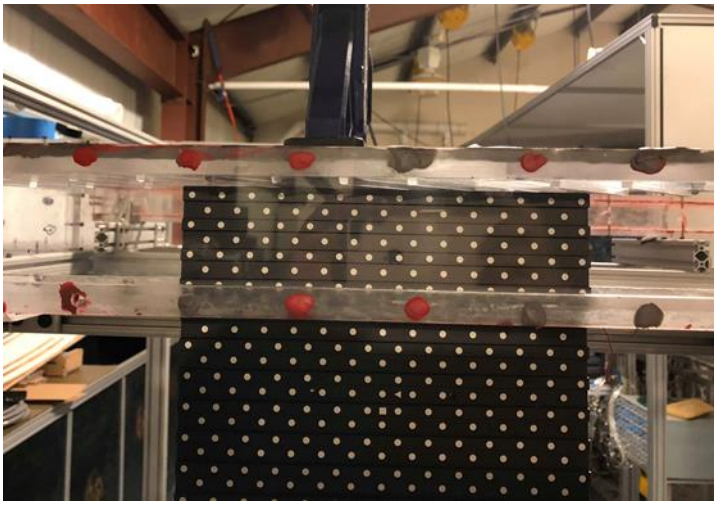

Figure 12 LaVision dual plane calibration plate

The flow was seeded with Di-Ethyl-Hexyl-Sebacate droplet (1-2 μm) since these particles offer good scattering efficiency and a small associated velocity lag. A Laskin nozzle-based atomizer was used to generate the Sebacate particles and were introduced at the inlet of the channel bellmouth. A Quantel Evergreen Nd: YAG (532 nm) double pulsed laser with up to 200 mJ per pulse was used to generate the laser beam. The optical system consists of a pair of spherical lenses with a variable distance between them, a cylindrical lens to spread the beam into a sheet, and a 45 degree mirror which bends the sheet up into the test section; the pair of spherical lenses allows for a variable focal length. The focal length is then varied, so that the resultant laser sheet, is ~ 2 mm thick at the measurement location. Cameras were synchronized with the laser at specifically timed pulses. The fluid with entrained particles was illuminated twice in short succession and an image pair of particle patterns for each camera were obtained. The time delay between the two successive pulses was changed from 6 to 200 μs on the basis of the flow Reynolds number. These pulse separations were chosen so that at the largest particle displacement does not exceed ~ 1/4 of the

interrogation window size. Around 1,500 image pairs (3,000 images) for each camera were obtained and used to process the data; this is enough to ensure fully converged statistical quantities. The stereoscopic PIV vector fields are generated from two, 2D velocity fields, which are obtained from the displacement of the seeding particles, and the time lag between the successive image pairs of each camera. Next, the 3D PIV velocity vector field is reconstructed from the combination of the two-2D vector fields, and knowledge of the relative camera angles to the measurement plane.

During the post processing, a high interrogation window overlap scheme was used to achieve increased spatial resolution. Therefore, high particle image density was provided, on the order of 8 to 12 particles per 32 x 32 pixel interrogation window. LaVision DaVis 8.3 software was used for velocity field correlation. After image pre-processing, a multi-pass algorithm was used. At first two initial passes of 64 x 64 windows at 50% overlap were performed, which were followed by 4 final passes at the interrogation window size of 32 x 32 with a 75% overlap. The adaptive window shape was used for the final passes, as implemented in DaVis 8.3. Additionally, the universal outlier detection scheme implemented within DaVis 8.3 was used to minimize the numbers of spurious vectors in the final resultant velocity fields. After vector correlation, an ensemble average of the ~ 1,500 velocity fields is performed to yield the statistical quantities of interest. Final vector resolution is 0.25 mm x 0.25 mm.

Coordinate Transformation of Vector Components

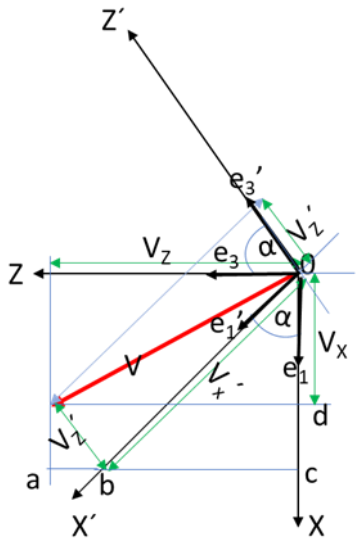

Figure 13 Coordinate transformation of vector components

The direction of the coordinate system XYZ for the PIV experiment and CFD is shown in Figure 9 (a)-(b). Vectors can exist independently of any coordinate system. For example, the vector V in Figure 13 can be expressed as:

$$\vec{V} = V_X e_1 + V_Y e_2 + V_Z e_3 = V_X' e_1' + V_Y' e_2' + V_z' e_3' \tag{58}$$

A new coordinate system $X'Y'Z'$ is created by a rotation of the base vectors by α about the Y axis. To transform any vector components from the XYZ to the $X'Y'Z'$ coordinate system, the following method has been used.

For two-dimensional transformation, only $X-Z$ and $X'-Z'$ are considered here. The vector components in X and Z coordinates can be expressed as:

$$V_Z = V_Z' \cos\alpha + V_X' \sin\alpha \tag{59}$$

$$V_X = V_X' \cos\alpha - V_Z' \sin\alpha \tag{60}$$

$$\begin{bmatrix} V_Z \\ V_X \end{bmatrix} = \begin{bmatrix} \cos\alpha & \sin\alpha \\ -\sin\alpha & \cos\alpha \end{bmatrix} \begin{bmatrix} V_Z' \\ V_X' \end{bmatrix} \tag{61}$$

where, transformation matrix $[Q] = \begin{bmatrix} \cos\alpha & \sin\alpha \\ -\sin\alpha & \cos\alpha \end{bmatrix}$

Multiplying the above equation with the inverse matrix $[Q]^{-1}$, the components in X´ and Z´ can be determined by the following equations.

$$\begin{bmatrix} V_Z' \\ V_X' \end{bmatrix} = \begin{bmatrix} \cos\alpha & -\sin\alpha \\ \sin\alpha & \cos\alpha \end{bmatrix} \begin{bmatrix} V_Z \\ V_X \end{bmatrix} \tag{62}$$

$$V_Z' = V_Z \cos\alpha - V_X \sin\alpha \tag{63}$$

$$V_X' = V_Z \sin\alpha + V_X \cos\alpha \tag{64}$$

Uncertainty in PIV Experiment

The uncertainties of the vector components mean V_Z, V_Y, V_X obtained by the PIV were calculated using LaVision DaVis 8.3 software. This software uses the Wieneke's correlation statistics method [75, 76, 77] to calculate the uncertainties. In this method, the two images are overlapped on each other by the computed displacement vector field. In an error free measurement, these paired images exactly match which does not happen in real experiments. The particle image size, seeding density, displacements, shear, etc. influence the accuracy of the experiment. Using the statistical analysis of the disparity between the two images the uncertainty of a displacement vector is estimated.

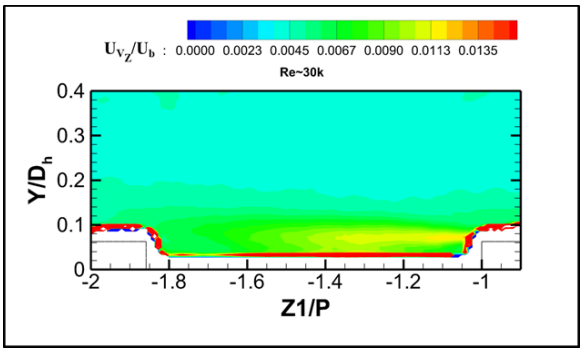

(a) Uncertainty in V_Z

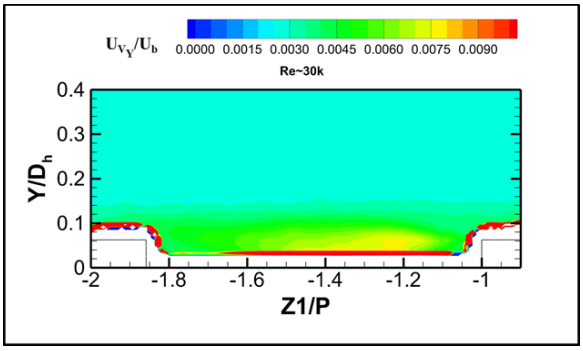

(b) Uncertainty in V_Y

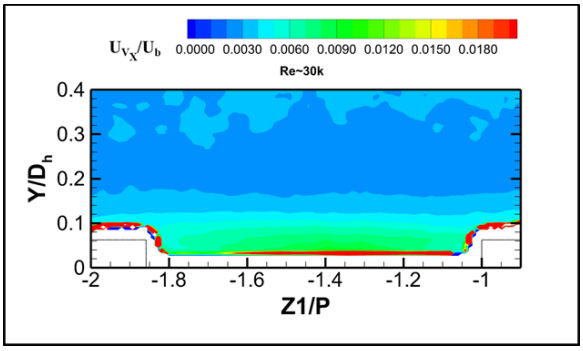

(c) Uncertainty in V_X

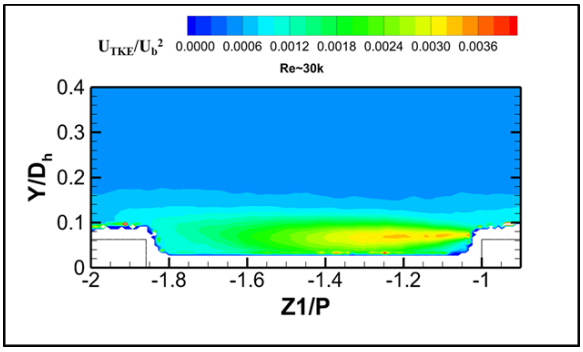

(d) Uncertainty in TKE

Figure 14 Uncertainties in PIV experiment at Re ≈ 30k

Figure 14 (a)-(c) shows the uncertainties in mean velocity components at Re ≈ 30k. The uncertainties are calculated for 95% confidence level. The bulk velocity U_b has been used for normalizing all the uncertainties. It was determined that the uncertainties in the mean velocities vary between 1% - 2% of U_b, respectively, depending on the flow turbulence. The uncertainties values are higher near the ribs due to high three-dimensional flow and high turbulence in this zone. The uncertainty in the turbulent kinetic energy is shown in Figure 14 (d). The maximum uncertainty in turbulent kinetic energy is ~ 0.4% of U_b^2. Figure 15 shows the normalized uncertainties in Reynolds normal and shear stresses at Re ≈ 30k. The high uncertainties are presents

in the separated shear layer generated from the ribs. The uncertainties for other Reynolds numbers are shown in the Appendix B.

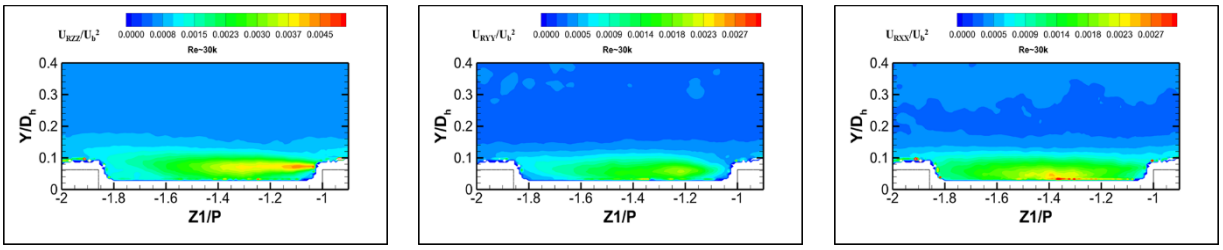

(a) Uncertainties the Reynolds normal stresses

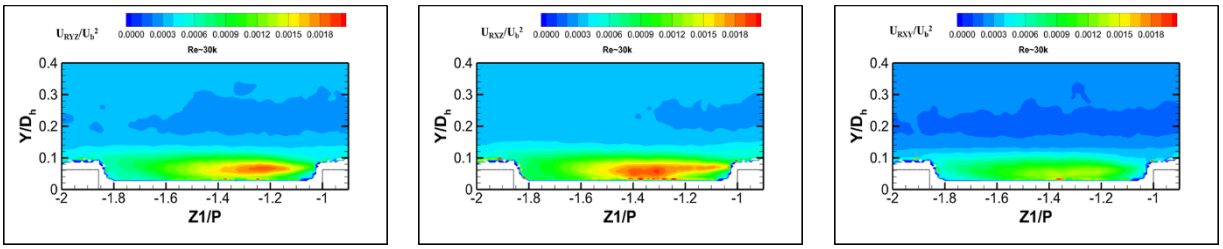

(b) Uncertainties in Reynolds shear stresses

Figure 15 Uncertainties in PIV experiment at Re ≈ 30k

CHAPTER 5: NUMERICAL SETUP

CFD studies were conducted for all the three configurations by using a commercial CFD software STAR-CCM+. One ribbed wall case was investigated using LES as well as RANS. The two ribbed wall cases were studied by RANS only. Three different EVM turbulence models were used to solve the RANS equations. They are as follows: a) Realizable k-ε model (RKE), b) SST k-ω, and c) v^2-f. All the three turbulence models as well as the SGS model for LES were used with default settings given in STAR CCM+ 10.06.010-R8.

Boundary Conditions

A comprehensive comparative study has been conducted between the numerical and experimental results. The setup of the numerical simulation resembled the experimental setup completely, except for the length of the channel. In the numerical simulations, the periodic fully developed flow condition at the inlet and outlet was applied, which allowed the calculation domain to be only one pitch, 1.25 inch (31.85 mm) of the test section. The periodic fully developed flow condition assumes that the flow repeats itself cyclically from one rib to the next. The experimental results corroborate this assumption as the flow becomes fully developed after $8D_h$ length from the entrance of the heated section. A study was performed to determine the sensitivity of the number of pitches in the computational grid. The sensitivity tests were done for a domain with three pitches and one pitch for the current geometry with the same mesh settings. Both cases showed very similar results. Therefore, only one rib pitch has been considered for the current study which is a common practice for these kind of geometries [28, 46, 56]. The assumption of a periodic fully

developed flow condition helped to achieve a reasonable number of nodes in the computational grid, thus reduced the computational time and cost. For this purpose, a periodic FDI boundary condition with a constant mass flow rate was applied at the inlet and outlet. All the walls including the ribs were specified as isothermal. The temperature of the walls was set to the temperature identical to the experiments. The test matrix for the CFD is listed in Table 8. Experimental results showed that flow became fully developed after $8D_h$ (will be discussed in the following section) from the starting point of the heated section. All the experimental fully developed heat transfer results presented here were located at $\left|\frac{Z}{D_h}\right| \approx 11.0$. Therefore, for consistency, the bulk temperature at the inlet in the CFD simulation was taken from the experimental bulk temperature data at $\left|\frac{Z}{D_h}\right| \approx 11.0$. Additionally, for the two ribbed wall cases, a symmetry condition was enforced at half of the channel height to reduce the domain further. The computational domain for CFD for two and one ribbed wall cases is shown in Figure 16 (a) and Figure 18 (a). The boundary conditions for the CFD simulations are listed in Table 9.

Table 8 Test matrix for CFD

		Nominal Re				
Ribbed wall	Ribs type	LES	RANS			
Two walls	Sharp ribs	-	20k	52k	95k	145k
	Round ribs	-	20k	52k	95k	145k
One wall	Sharp ribs	30k	30k	-	-	-

Table 9 Boundary conditions for CFD

Boundary condition	Two ribbed wall cases	One ribbed wall case
Walls	No-slip, Isothermal (~ 80°C)	No-slip, Isothermal (~ 70°C)
Inlet-Outlet	FDI with a const. mass flow rate	FDI with a const. mass flow rate
Symmetry	At the half of the rib height	N/A
Inlet bulk temperature	~ 35° C	~ 30° C

Mesh for RANS

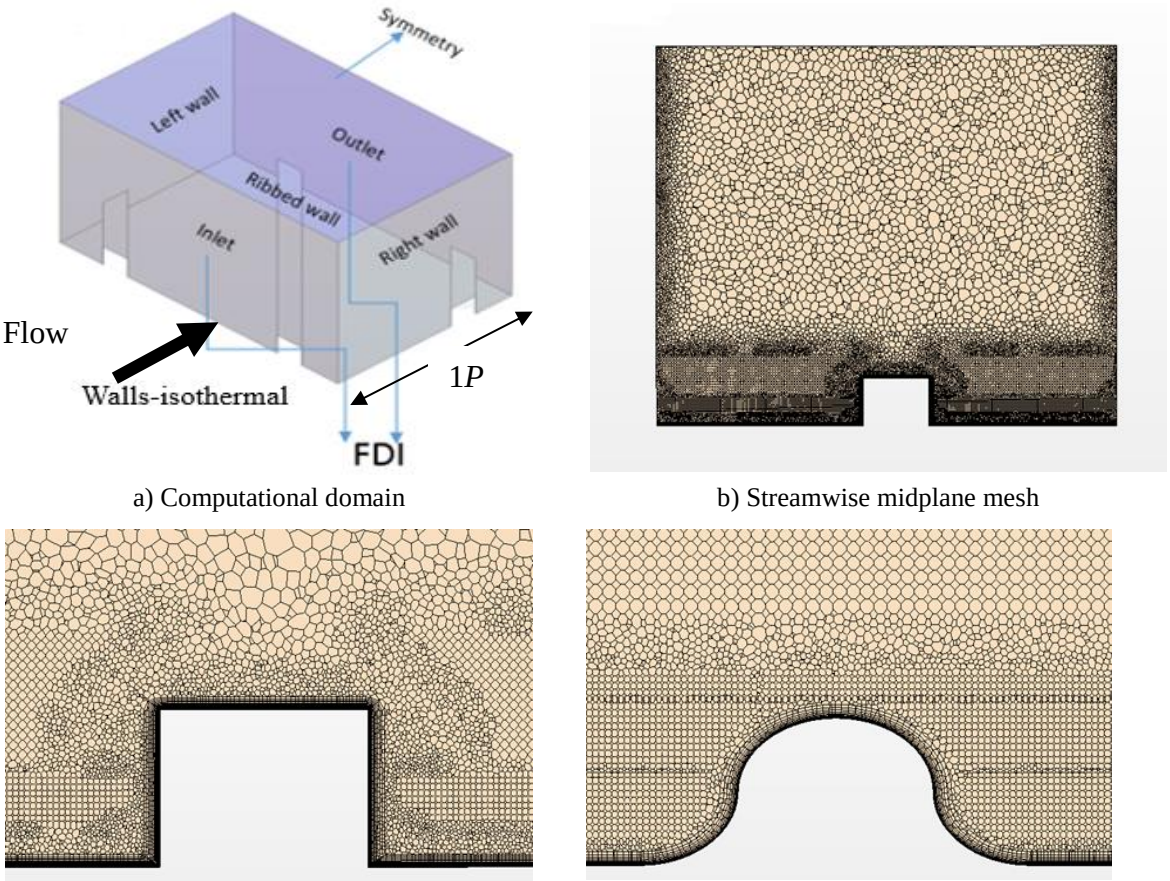

a) Computational domain

b) Streamwise midplane mesh

c) Grid topology near ribs

Figure 16 Computational domain and grid topology for two ribbed wall cases

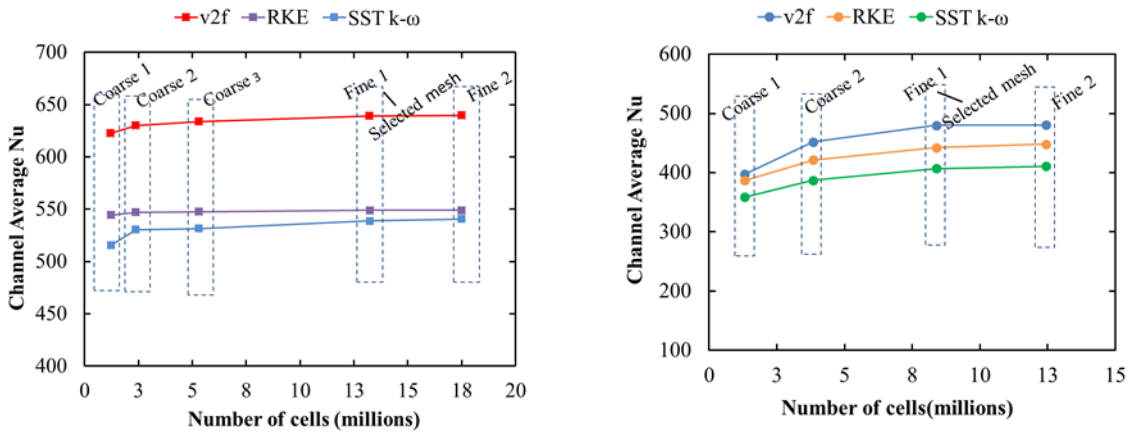

a) Sharp ribs b) Round ribs

Figure 17 Grid convergence study at Re ≈ 145k for two ribbed wall cases

Table 10 Mesh parameters for the computational grid for two ribbed wall cases

	Sharp ribs	Round ribs	
	Fine 1	Fine 1	Fine 2
Prism layer thickness (mm)	0.25	0.3	0.25
Number of prism layers	18	12	15
Stretching factor	1.14	1.24	1.16
First layer *y*+	< 1	< 1	< 1
Total number of cells (million)	~ 13.5	~ 8.4	~ 12.5

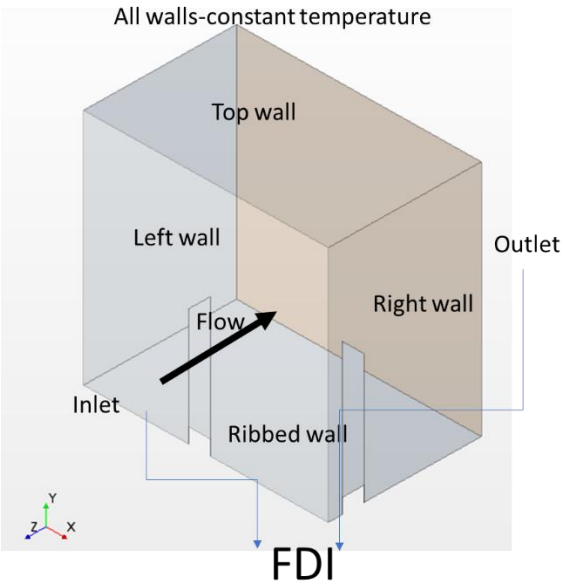

a) Computational domain

b) Streamwise midplane mesh (LES)

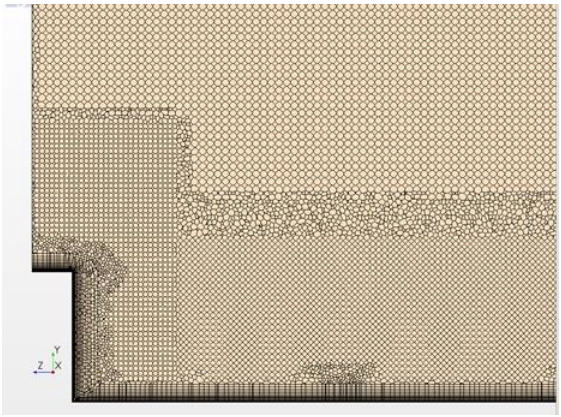

c) Grid topology near ribs in LES domain

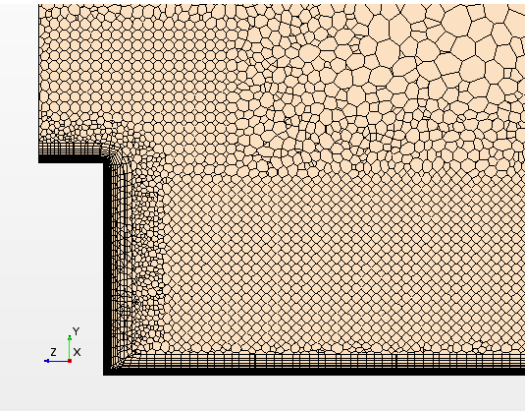

d) Grid topology near ribs in RANS domain

Figure 18 Computational domain and grid topology for CFD for one ribbed wall case

The computational grid consisted of unstructured hybrid meshes generated by STAR-CCM+. The near wall discretization was done with prism layers, while the main flow area was discretized using a polyhedral mesh. The grid topology for two ribbed wall cases is shown in Figure 16 (b) and (c). The grid topology for the RANS simulation for the one ribbed wall case is shown in Figure 18 (d).

By using a conscientious volumetric control and proper surface size, a very refined mesh was developed around the ribs and the walls. Strategical selection of the density and growth cell rate was helped to reduce the total number of cells. The smooth transition between the volume control and the regular polyhedral mesh growth was assured by using the proper blending factors. The mesh was designed to satisfy the first layer $y+$ values less than one for all the Re cases. Table 10 shows the parameters used to generate the prism layers in the simulation grid for both two ribbed wall cases.

Grid Convergence for Two Ribbed Wall Cases

The mesh resolution around the ribs and on the walls is very critical for precise prediction of heat transfer and pressure drop in such turbulated channels. Hence, a mesh sensitivity analysis was conducted to obtain a mesh independent solution for all the three turbulence models at the highest investigated Re ≈ 145k for both two ribbed wall cases which are shown in Figure 17. The overall base size of the mesh was modified to achieve the finer grid. The left picture in Figure 16 (c) shows the grid topology for the sharp ribs case for Fine 1 mesh referred to Figure 17. To determine if the mesh refinement near the ribs and the walls in Fine 1 mesh were enough, more refinement was done around this zone in Fine 2 mesh. The sensitivity study (Figure 17 (a)) shows that change in channel average Nu is only about 0.2%, 0.03% and 0.36% from 13.5 million (Fine 1) to 17.5 million (Fine 2) cells for v^2-f, RKE, and SST k-ω turbulence models, respectively. Therefore, the Fine 1 (13.5 million) mesh was selected for the present study. Similarly, Figure 17 (b) shows the grid convergence study for the round ribs case. It shows that the channel average Nu changes about 0.1%, 1.4%, and 1% from 8.4 (Fine 1) to 12.5 (Fine 2) million cells for v^2-f , RKE, and SST k-ω

models, respectively. The Fine 1 grid for the round ribs case has a slightly high stretching factor ~1.24 for prism layers (Table 10). However, the prism layers of Fine 2 mesh have a stretching factor ~1.16 and the results with this mesh show an excellent agreement with the Fine 1 results. Therefore, Fine 1 (~ 8.4 million) mesh was chosen for the round ribs case.

Grid Convergence for One Ribbed Wall Case

The mesh sensitivity analysis for the computational grid of the RANS for the one ribbed wall case was also conducted. The overall base size of the mesh was modified to achieve the finer grid which can be seen in Figure 19. The smooth transition was ensured between the prism layers and the regular polyhedral mesh as well as between the volume controls for all the three meshes (coarse 1, Fine 1 and Fine 2). The smooth transition was achieved by the strategical selection of the different mesh setting parameters, such as surface size, mesh density, and growth factor, surface growth rate, volume growth rate, and the volumetric control blending factor.

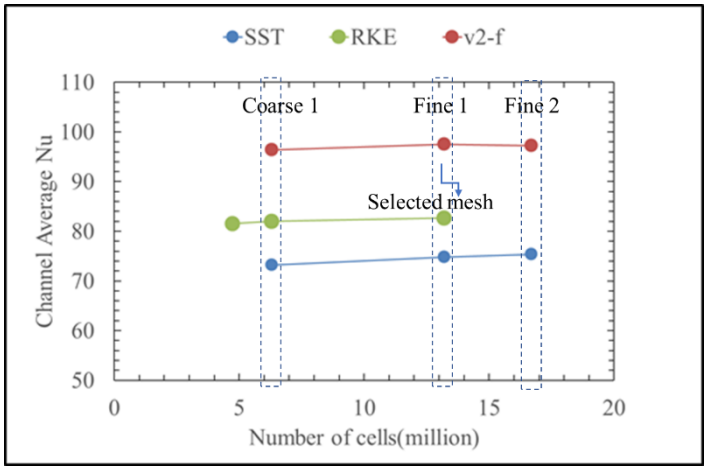

Figure 19 Grid convergence study for one ribbed wall case at Re ≈ 30k

The sensitivity study (Figure 19) shows that change in channel average Nu is only about 0.3%, 0.7% from 13.2 million (Fine 1) to 16.7 million (Fine 2) cells for v^2-f and SST k-ω turbulence models, respectively. The change in channel average Nu is only about 0.8% from 6.3 million cells (coarse 1) to 13.2 million cells (Fine 1) for RKE. Therefore, the Fine 1 (13.2 million) mesh was selected for the RANS simulations of the one wall study case.

Table 11 Numerical settings for RANS for two ribbed wall cases

Parameters	Settings		
Space	3D		
Time	Steady		
Viscous	SST k-ω	RKE	v^2-f
Wall treatment	All y+	Two-layer all y+	All y+
Pressure-velocity Coupling	SIMPLE		
Equations solved	Flow, Energy		
Solver for flow	Segregated flow		
Solver for energy	Segregated fluid temperature		
Discretization scheme for momentum	2nd order		
Discretization scheme for energy	2nd order		

The working fluid of the simulations was air and used the ideal gas law for the simulation. The temperature of the walls was set to the temperature identical to the experiment for each Re. The settings for the RANS simulation for two ribbed wall cases are listed in Table 11. The post

processing of the CFD results was performed with the same methodology as that of the experiments. Unlike the experiments, friction investigations were conducted simultaneously with the heat transfer in the CFD analysis. A separate CFD friction investigation was performed at Re ≈ 100,000 for the cold condition by setting adiabatic boundary conditions at all the walls, and inlet bulk temperature to 23°C. The result indicates only ~ 1% variation in friction result with the heated case.

LES Mesh

Like the RANS meshes, the computational grid for LES also consisted of unstructured hybrid meshes. The near wall discretization was done by prism layers while the main flow area was discretized using a polyhedral mesh. Figure 18 (c) shows the grid topology near the ribs for LES. The volumetric control and the surface size were chosen very meticulously to obtain a very fine mesh near the ribs and the walls. A carefully chosen blending cell factor helped to achieve a smooth transition among the control volumes and regular polyhedral mesh growth. A good boundary layer resolution is required to capture the physical behavior accurately. The mesh was designed to satisfy the first layer y+ values less than 1 and the total thickness of the prism layers contained the entire boundary layer. Table 12 shows the mesh criterion for wall-bounded LES calculation proposed by Piomelli and Chasnov [78]. These criteria are provided for the structured mesh. Since the mesh for the current study was unstructured mesh, the grid size was chosen such that $\Delta d+$ < 3-16 everywhere in the domain and the first layer $y+$ < 1. Here, Δd is each nominal cell size ($\sqrt[3]{}$ (cell volume)).

Table 12 Mesh criteria for wall-bounded LES calculation [78]

Dimensionless grid spacing	Piomelli and Chasnov [78]	Current study	
$\Delta x+$	< 100-300	$\Delta d+$	<3-16
$\Delta z+$	< 100-600		
$y+$	< 25-30	$y+$	< 1

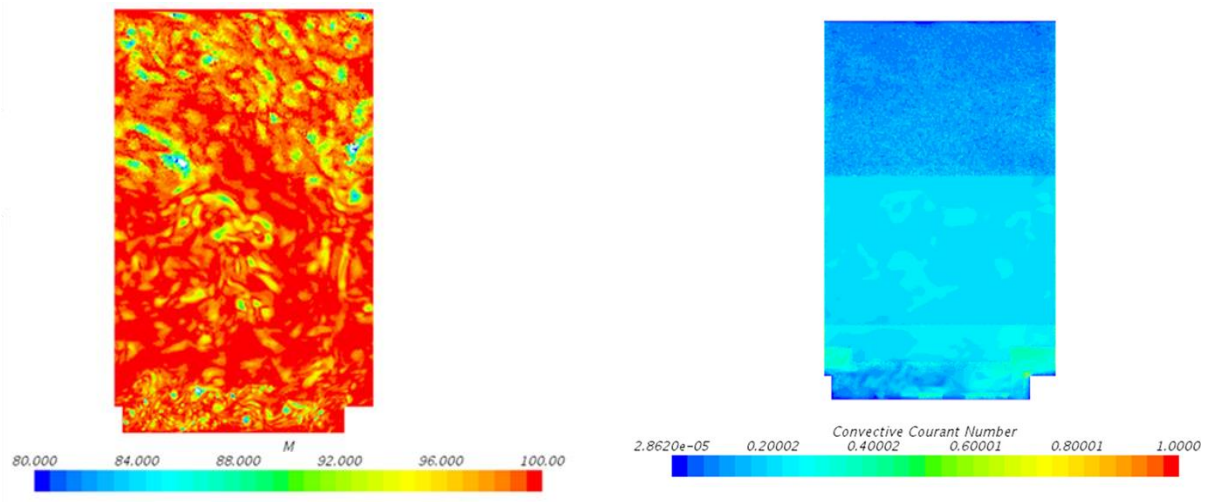

a) b)

Figure 20 a) The ratio of resolved turbulent kinetic energy to the total kinetic energy b) Convective Courant number in the streamwise midplane

Pope [59] describes that the ratio (M) of the resolved turbulent kinetic energy to the total kinetic energy is crucial to determine the resolution of the LES. He suggests that the ratio M needs to be greater than 80% to obtain a well resolved LES results. The grid was refined to satisfy this condition everywhere. Figure 20 (a) displays the ratio M in the streamwise midplane in terms of percentage. To satisfy this condition, the computational grid of LES needs a high refinement, which resulted in ~ 23million cells in the computational domain. Due to unstructured mesh, to

achieve the value of M ratio greater than 80% in the full domain, the grid needs to be more refined which will cause massive cell counts. To avoid this, the current grid was chosen where only 0.33% of total cell counts show M < 80%. The minimum M for the domain is ~ 55%. Figure 20 (a) shows the ratio M in the streamwise midplane. The mesh parameters for the computational grid of the one ribbed wall case are listed in Table 13.

Table 13 Mesh parameters for the one ribbed wall case

	LES	RANS
Prism layer thickness (mm)	0.44	0.3
Number of prism layers	20	20
Stretching factor	1.15	1.18
Prism layer near wall thickness, mm	4E-3	2E-6
First layer *y*+	< 1	< 1
Total number of cells (million)	~ 23.4	~ 13.2

Solvers and Solution Method

For LES, a steady RANS model was performed at first and then LES was carried out. An implicit time stepping was used. The time step (Δt) is required to be small enough to achieve the Convective Courant number ($\frac{u\Delta t}{\Delta d}$) smaller than one in the whole domain. The time step Δt = 2E-6 s used for the simulation. Due to the unstructured nature of the grid, ~ 0.1% cells showed Courant number > 1. To achieve the Courant number < 1 in the whole domain, the Δt needs to be even

smaller, which makes the computational cost very high. Figure 20 (b) shows the Convective Courant number values in the streamwise midplane of the channel.

Table 14 Numerical settings for the one ribbed wall case

Model	LES	RANS		
Space	3D	3D		
Time	Unsteady, 2nd order implicit	Steady		
Viscous	LES	RANS		
Sub-Grid Scale Model	WALE	N/A		
Turbulence Model	N/A	RKE	SST k-ω	v^2-f
Wall treatment	All y+	Two-layer all y+	All y+	All y+
Pressure-Velocity Coupling	SIMPLE	SIMPLE		
Equations solved	Flow, Energy	Flow, Energy		
Discretization Scheme				
Momentum	Bounded Central Differencing	2nd order		
Energy	2nd order	2nd order		
Temporal	2nd order	N/A		
Unsteady Calculation Parameters				
Time Step (s)	2.0E-6 s	N/A		
Maximum iterations per time step	25	N/A		
Total Time (s)	0.38s	N/A		

The LES simulation was allowed to run 25 flow through times until the flow reached to statistically stationary state. Once stationary conditions were accomplished, acquisition of samples to determine mean and turbulent quantities was performed for ~ 85 flow through times to achieve statistical convergence. Table 14 shows the list of the numerical settings for both the LES and RANS simulation for one ribbed wall case.

Convergence Criterion

For all RANS cases, the continuity, momentum, and energy residuals for the solution were reached below 10^{-5}. Apart from residuals, the convergence of primitive variables like pressure and velocities were also monitored. The boundary heat transfer on all four walls was also monitored to assure the convergence of the simulation. Among these models, SST k-ω showed fluctuations in the primitive variables. Once the solution became steady, the average of the last 3000 iterations was calculated to report the final flow field and heat transfer results.

For LES, inner iteration steps were applied at each time step so that a relative reduction of the continuity, momentum, and energy residuals reach to 10^{-3}. Multiple point probes were introduced inside the separated shear layer region near the ribs to check statistical convergence. The mean and the second order statistics of the flow variables ensured statistical convergence. Figure 21 shows some examples of statistical convergence. Some other examples of the statistical convergence have been shown in the Appendix C.

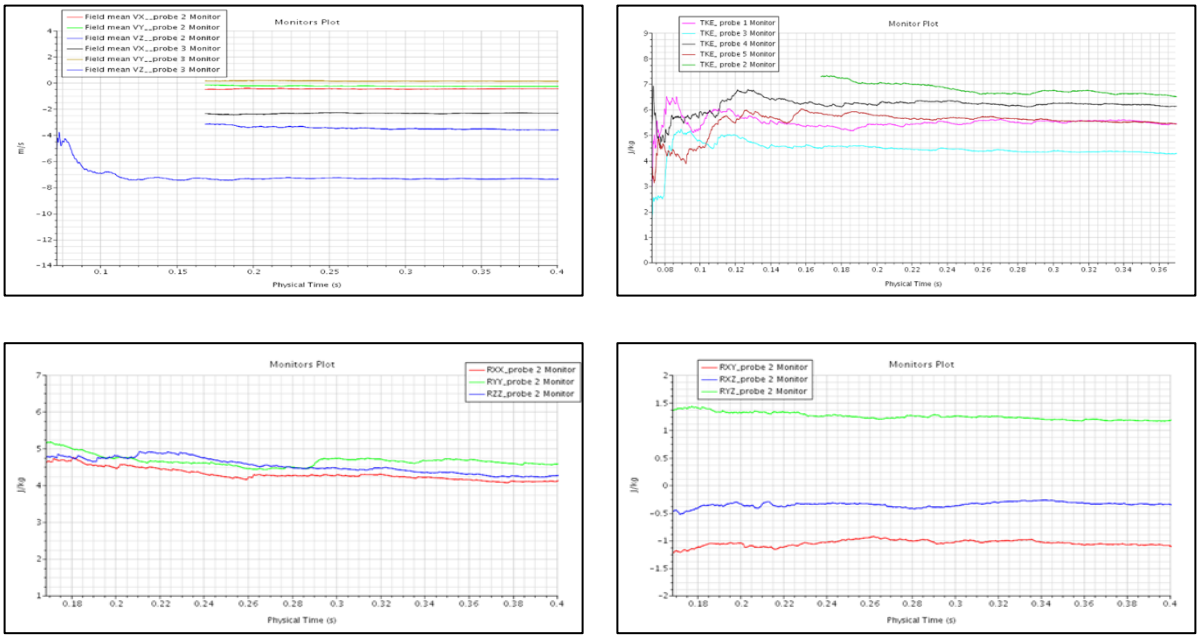

Figure 21 Statistical convergence of LES

CHAPTER 6: HEAT TRANSFER AND PRESSURE DROP RESULTS FOR SHARP AND ROUND RIBS

Several heat transfer and pressure drop experiments for the two ribbed wall cases with sharp and round ribs were performed at different Re ranging from 6,000 to 135,000. Measurements for sharp ribs were first collected for Re ≈ 6,000 to 70,000 to benchmark the results against data presented in Han et al. [18]. Then, experiments were extended up to Re ≈ 135,000 for both sharp and round cases. Note that, the results discussed in this chapter are of two ribbed wall cases.

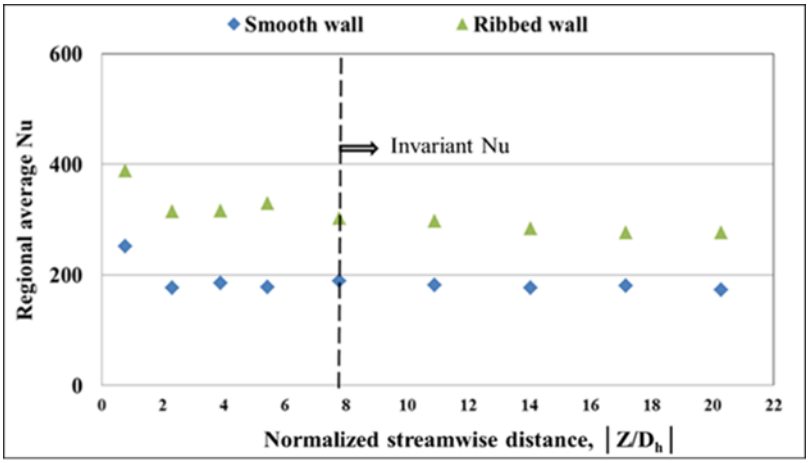

Figure 22 Module average Nu for the sharp ribs at Re ≈ 55,000

The module/regional average Nu distribution along the streamwise direction shows that the beginning of the test section has a higher value of Nu because of the developing thermal boundary layer. After a distance of $8D_h$ from the heated test section entrance, Nu becomes almost constant and this phenomenon is consistent for all the Re cases for all the configurations. For instance, the regional average Nu distribution along the channel for Re ≈ 55,000 is shown in Figure 22, where the regional average Nu for both smooth and ribbed walls become almost invariant around 200

and 315, respectively after $\left|\frac{Z}{D_h}\right|$ =8.0. The abscissa of Figure 22 denotes the distance of the center of each module from the beginning of the heated section. The average smooth wall Nu denotes the average Nu value of the two opposite smooth side walls. Similarly, the average ribbed wall Nu denotes the average Nu of two opposite ribbed walls.

Comparative Study with Literature

A detailed comparison was conducted for the heat transfer and friction results for the sharp ribs case with the results presented in Han et al. [18]. Figure 23 (a) shows the comparative results of fully developed average Nu of two opposite smooth (SW) and ribbed walls (RW) for sharp ribs. Note that the Re numbers reported in Han et al. [18] and the current study were not the same. For a fair comparison, the results of the current studies are correlated with Re and reported at the same Re values as in Han et al. [18]. For validating the experimental results, fully developed average Nu at $\left|\frac{Z}{D_h}\right| \approx 11.0$ are compared with the results at the similar location in Han et al. [18]. All the Re reported in this article are the local Re at $\left|\frac{Z}{D_h}\right| \approx 11.0$. The local Re denotes the Re calculated at the local air bulk temperature. The results of both smooth and ribbed walls (Figure 23 (a)) are in excellent agreement with Han et al. [18] within measurement uncertainties. Note that, Han et al. [18] reported the maximum experimental uncertainty in their Nu and friction results, are 6.8% and 6.6 %, respectively at Re > 10,000. When Re is greater than 20,000, the maximum observed difference between the current study and Han et al. [18] is around 4% and 8% for ribbed and smooth walls, respectively. Higher deviations have been observed for Re ≈ 6,000 and 20,000. Higher experimental uncertainty at low Re results from both the current study and Han et al. [18],

may have caused these deviations. Moreover, the flow physics is also not well understood at such low Re and needs further investigation. Figure 23 (b) presents the comparative results of fully developed channel average Nu (average of smooth and ribbed wall Nu) for sharp ribs between the experiments, and Han et al. [18] in log-log scale. This figure demonstrates an excellent match between the results of the current experimental study and Han et al. [18]. Both these results fit within the measurement uncertainty. The maximum deviation between the two studies is around 4% beyond Re ≈ 20,000.

The friction factor in a smooth channel is caused by skin friction only. On the other hand, friction in a ribbed channel is primarily caused by the ribs produced form drag. In a ribbed channel, flow separation occurs behind and top of the ribs which in turn results in form drag. Ribs also cause flow separation of the boundary layer, which contribute to higher pressure losses as well. Figure 23 (c) and (d) presents the comparative study of the friction factor and friction augmentation for the sharp ribs between the experiments and Han et al. [18]. Friction augmentation is the friction enhancement caused by the application of ribs compared to that of the smooth channel of equal hydraulic diameter. For this reason, the friction factor is normalized with the smooth channel f_0 value. In Figure 23 (c), the vertical error bars represent the experimental uncertainties in the friction factor. Similarly, the horizontal error bars represent the experimental uncertainties in Re. The friction results of the current study show very good agreement with Han et al. [18] (within measurement uncertainties). The current study also confirms the friction vs. Re curve trend observed in Han et al. [18]. Both studies show that the friction factor increases with Re at very low

Re (6,000-15,000). After that, it decreases as Re increases and settles to a value beyond Re = 30,000. Friction factor remains unchanged with Re larger than 30,000.

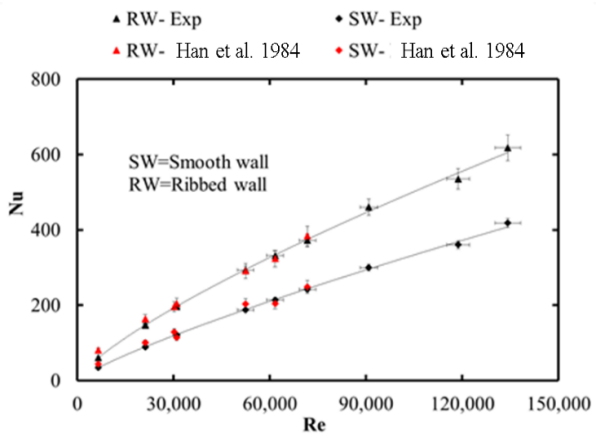

a) Fully developed smooth and ribbed wall Nu vs. Re

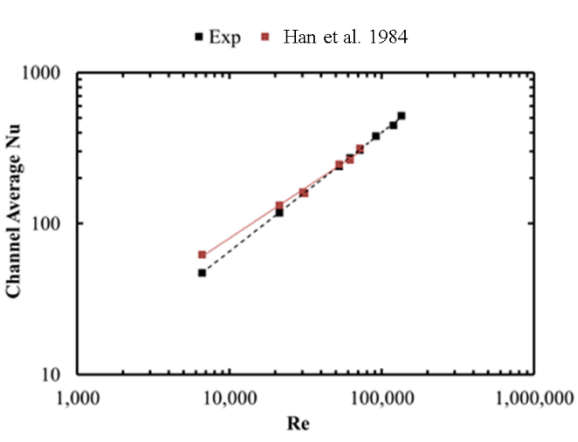

b) Fully developed channel average Nu vs. Re

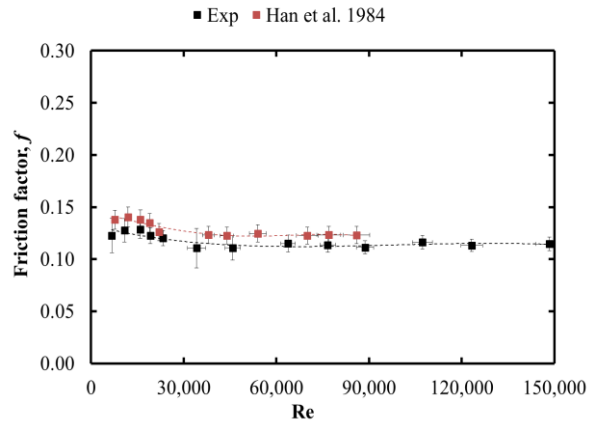

c) Friction factor vs. Re

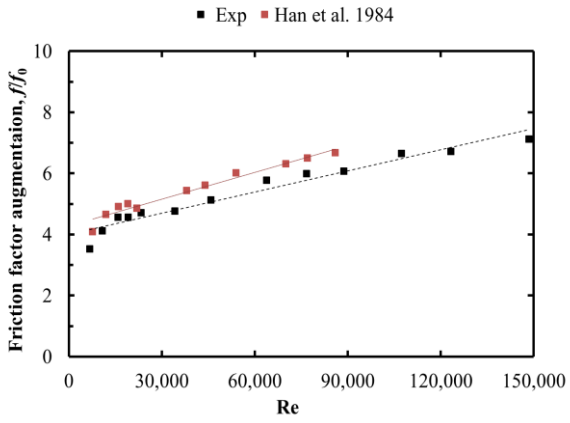

d) Friction augmentation vs. Re

Figure 23 Comparative study between the experiment and Han et al. 1984 for the sharp ribs

Comparative Study between Sharp and Round Ribs

In this study, a detailed comparative analysis of the sharp and round ribs was conducted both experimentally, and numerically. Similar to the sharp ribs, the heat transfer and friction

experiments for the round ribs were performed for several different Re values in the range of 6,000 to 135,000. Numerical simulations for both sharp and round ribs were performed at Re ≈ 20,000, 52,000, 95,000, and 145,000.

Heat Transfer Results

Figure 24 shows the comparative results of experimental fully developed heat transfer results for sharp and round ribs at different Re.

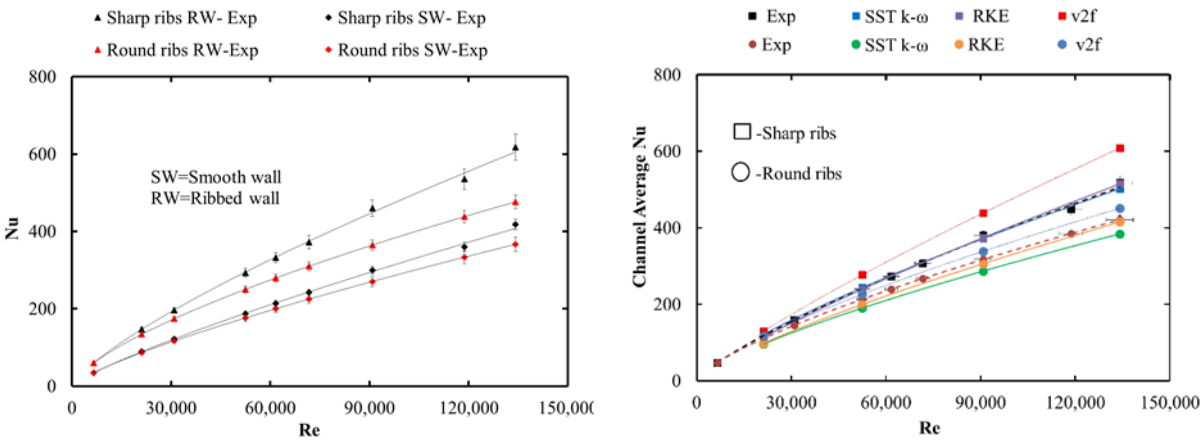

a) Smooth and ribbed wall Nu vs. Re b) Channel average Nu vs. Re

Figure 24 Comparative fully developed heat transfer results between the sharp and round ribs

Both Figure 24 (a) and (b) show that the sharp ribs case, possesses a significantly higher heat transfer capacity than that of the round ribs case, especially on the ribbed walls at high Re. The enhancement of Nu with the sharp ribs over the round ribs increases with increasing Re. For instance, at the lowest tested Re ≈ 6,000, both sharp and round ribs show very similar heat transfer

results. After that, sharp ribs result in more heat transfer than the round ribs with increasing Re. For instance, sharp ribs show 9% to 23% and 1% - 13% higher heat transfer capability on the ribbed and smooth wall, respectively. This leads to 7% - 23% higher channel average (average of smooth and ribbed wall Nu) heat transfer for sharp ribs than the round one, which is demonstrated in Figure 24 (b). This figure presents the comparative results of channel average Nu for both sharp and round ribs between the experiments, and the CFD results using SST k-ω, RKE, and v^2-f turbulence models at different Re. The CFD results also establish the fact that round ribs cause lower heat transfer than the sharp ribs. It is found that the v^2-f turbulence model highly overpredicts the measured heat transfer results for sharp ribs by 10% - 17% for all Re cases. The percentage of overprediction by v^2-f increases as Re increases. The possibility of overprediction by this turbulence model on heat transfer and pressure drop in a turbulated channel is well documented in the literature (e.g., Schüler et al. [79]). They studied different turbulence models including v^2-f for investigating the heat transfer and friction behavior in a two-pass ribbed channel with 45° ribs and found that the v^2-f turbulence model overpredicts their experimental results by 25% - 80% which agrees with the results in this study. However, the v^2-f turbulence model does not overpredict by a large margin for round ribs, compared to the sharp ribs. It shows 5% - 7% overprediction from the experimental data of round ribs. For sharp ribs, both RKE and SST k-ω show very similar Nu results and predict the measured data very well with a maximum overprediction of ~ 4%. Similarly, RKE also shows a very good match for the round ribs' measured data (maximum under prediction ~ 6% beyond Re > 20,000). However, SST k-ω model underpredicts the round ribs' results by approximately 9% - 13%.

Figure 25 (a) presents the comparative results of the fully developed channel average Nu augmentation ($\frac{Nu}{Nu_0}$) between the sharp and round ribs. For this, the fully developed channel averaged Nu is normalized with the smooth channel Nu_0 value. The Dittus-Boelter correlation for smooth circular tubes has been used to calculate Nu_0. The experimental results show that both types of the ribs cause similar heat transfer augmentation at Re ≈ 6,000. The sharp ribs produce higher heat transfer augmentation than the round ribs in all other Re cases. The Nu augmentation of the sharp ribs remains almost constant with the increasing Re. However, the round ribs show a decreasing trend of $\frac{Nu}{Nu_0}$ with Re. As Re value is changed from 6,000 to 135,000, the $\frac{Nu}{Nu_0}$ value decreases from 2.09 to 2.05 and 2.09 to 1.66 for sharp and round cases, respectively. It concludes that at lower Re, the heat transfer augmentation capabilities of both types of ribs are similar, but sharp ribs perform better at high Re. In contrast with the experiment, the v^2-f turbulence model shows an increasing trend of Nu augmentation with Re for sharp ribs. For the same case, RKE also shows a slightly increasing trend of Nu augmentation with Re. Only SST k-ω conforms to the experimental trend for this case. On the other hand, all three turbulence models show the decreasing trend for Nu augmentation for round ribs.

Friction Results

Figure 25 (b) presents the comparative friction augmentation ($\frac{f}{f_0}$) results caused by both sharp, and round ribs. Both sharp and round cases depict that friction augmentation increases linearly with increasing Re. Results show that round ribs cause only 6% - 9% lower friction than sharp ribs in the experimented Re range. On the other hand, the round ribs experience a much greater reduction

in heat transfer, compared to the sharp ribs especially at higher Re. The round ribs cause ~ 10% - 20% reduction in heat transfer than sharp ribs at Re ≥ 50,000. This is also shown in Figure 25 (c). For the current geometry ($\frac{e}{D_h}$ = 0.0625), rounding the rib corners does not reduce the friction to a great degree, but reduces heat transfer especially at high Re. This finding is in contrast with the results found with high blockage ratio ribs [12, 7].

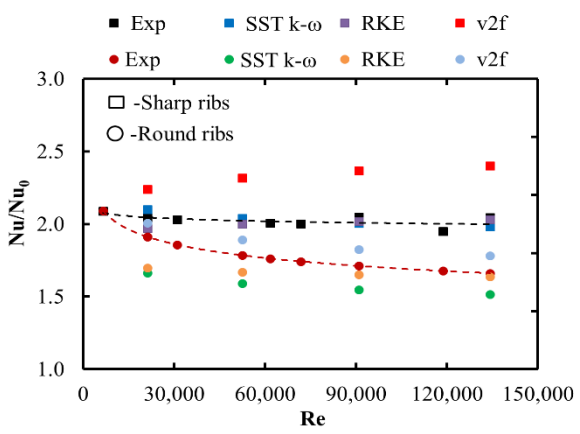

a) Nu augmentation vs. Re

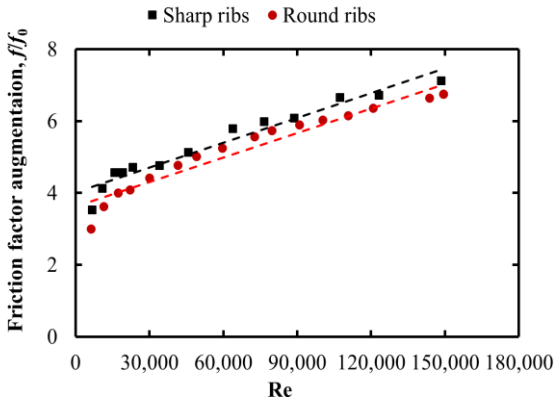

b) Experimental friction augmentation vs. Re

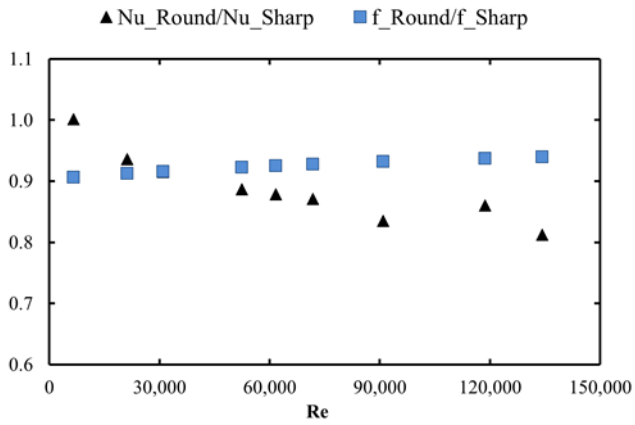

c) Reduction of Nu and f with round ribs compared to the sharp ribs

Figure 25 Comparative results of sharp and round ribs at different Re

Figure 26 presents the comparative results of friction augmentation between experiment and CFD. Similar to the experimental data, all three turbulence models suggest that rounding the edges of the ribs helps in lowering the pressure drop/friction. CFD data indicates that both types of ribs cause similar friction at very low Re. The round ribs produce less and less friction augmentation compared to the sharp ribs with the increasing Re. All three turbulence models are found to overpredict the friction for both types of ribs. Among them, v^2-f shows the maximum overprediction by ~ 13% - 18% and 6% - 30% for sharp and round ribs, respectively. RKE and SST k-ω predicts similar friction augmentation for both cases. These models display better match with the experimental results of the sharp ribs with maximum ~ 9% (RKE) and 13% (SST k-ω) overprediction at the lowest Re. At the higher Re, both models match the experimental data even more. Similarly for the round ribs, these models show higher deviation at lower Re (maximum ~ 20%) but match its data well (within ~ 6% deviation) at higher Re (Re > 50,000).

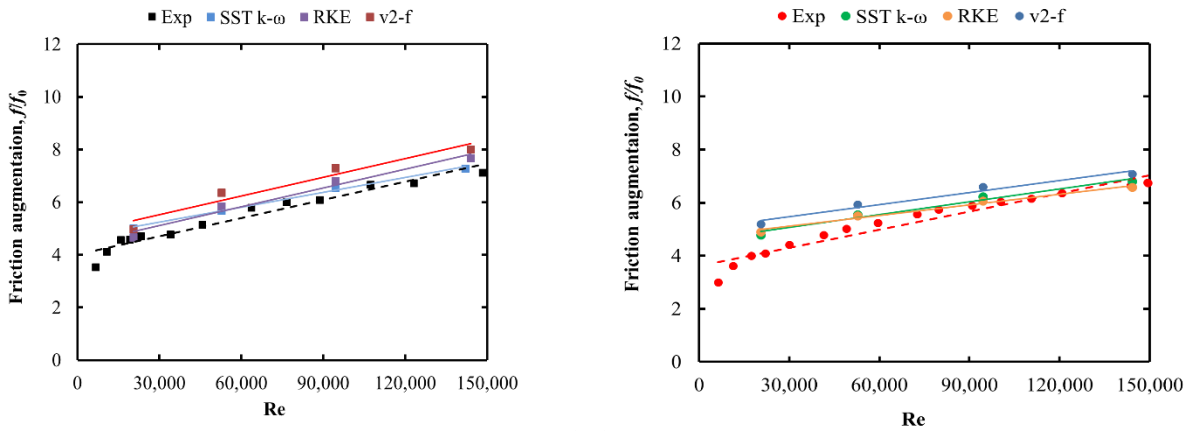

a) Sharp ribs b) Round ribs

Figure 26 CFD results of friction augmentation at different Re

Thermal Performance Results

Figure 27 (a) and (b) shows the comparative thermal performance results of sharp and round ribs at different Re, respectively. As mentioned earlier, both heat transfer and friction experiments were conducted for several Re in the range of 6,000 to 135,000, but not at the exact Re. Therefore, a linear curve fit for friction augmentation to Re was constructed to determine friction factor at any Re for both sharp and round ribs cases. Similarly, separate power curve fits were also constructed to correlate the channel average Nu with Re. Then, these curve fits were utilized to find the Nusselt number and friction factor during the thermal performance calculation.

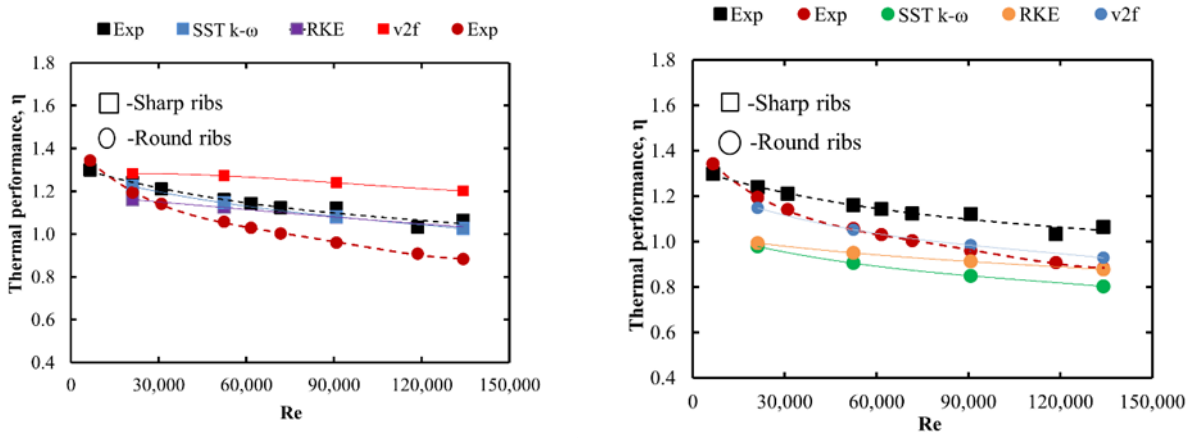

a) Sharp ribs b) Round ribs

Figure 27 Comparative results of thermal performance for sharp and round ribs at different Re

In Figure 27 (a) and (b), both CFD and experimental results show that the thermal performance value is higher due to the lower friction augmentation at lower Re. With increasing Re, the friction augmentation increases linearly while the Nu augmentation value remains almost the same for all

the Re cases (slightly decreases with Re as shown in Figure 25 (a)), which causes a gradual decrease in thermal performance for both sharp and round ribs. It has been found that both types of ribs show similar thermal performance at very low Re (≈ 6,000). Beyond 6,000, the sharp ribs show higher thermal performance for all other tested Re. As the Re increases, the difference between the thermal performances curves of the two cases diverges. The thermal performance curve for the round ribs is steeper than that of the sharp case. Consequently, the thermal performance of the round ribs becomes lower than unity at comparatively lower Re ≥ 90,000. However, thermal performance of the sharp ribs remains above unity in the tested Re range. The trend of the thermal performance curve indicates that it falls below unity at Re ≥ 180,000.

The CFD results show that the v^2-f turbulence model overpredicts the sharp rib's thermal performance result by 3% to 13%, whereas it shows a good match with the round ribs case (deviation ~ 1% - 5%). The overprediction by v^2-f for the sharp case increases with the increasing Re. On the other hand, both RKE and SST k- ω display very similar results for sharp ribs and agree with the experimental data very well (maximum deviation ~ 6%). However, both models overly underpredict the round case's experimental data; i.e., RKE and SST k-ω results deviate from the data by 1% - 16% and 9% - 19%, respectively.

CHAPTER 7: AEROTHERMAL ANALYSIS OF SHARP RIBS

This chapter presents the flow study results of the one ribbed wall case obtained by stereo PIV at different Re. A detailed comparison of the aerothermal behavior was also made between the experimental data and the numerical results at Re ≈ 30,000. The discussion starts with a detailed comparison between the flow field results obtained with PIV, LES, and RANS. Next, a comparative analysis of heat transfer and the pressure drop behavior has been conducted between the experiment, LES as well as the RANS. It follows up with a detailed analysis of flow, especially the secondary flow behavior and the heat transfer behavior of the walls obtained by LES. Finally, the stereo PIV results at different Re are presented focusing on the change of flow field with the increasing Re.

Mean Velocity Results

Figure 28 (a)-(d) present the non-dimensional mean velocity and turbulent kinetic energy contour plots in the streamwise midplane at Re ≈ 30k obtained by Stereo PIV. The bulk velocity U_b is used for normalization. Note that the main axial flow goes in $-Z$ direction. Consequently, the mean $\frac{V_Z}{U_b}$ is negative in the streamwise direction. A new local coordinate $Z1$ is introduced along the Z axis. The $Z1$ = -1 is located at the trailing edge of the first rib in the plane. Hereinafter, the wall-normal and streamwise coordinates are normalized with the channel's hydraulic diameter, D_h and rib pitch, P, respectively. In these figures, the results are presented for the two rib pitches between the three ribs. It is clearly observed that flow characteristics between both the pitches are identical

which confirms that flow is fully developed at the point of measurement. This finding applies to all the tested Re cases.

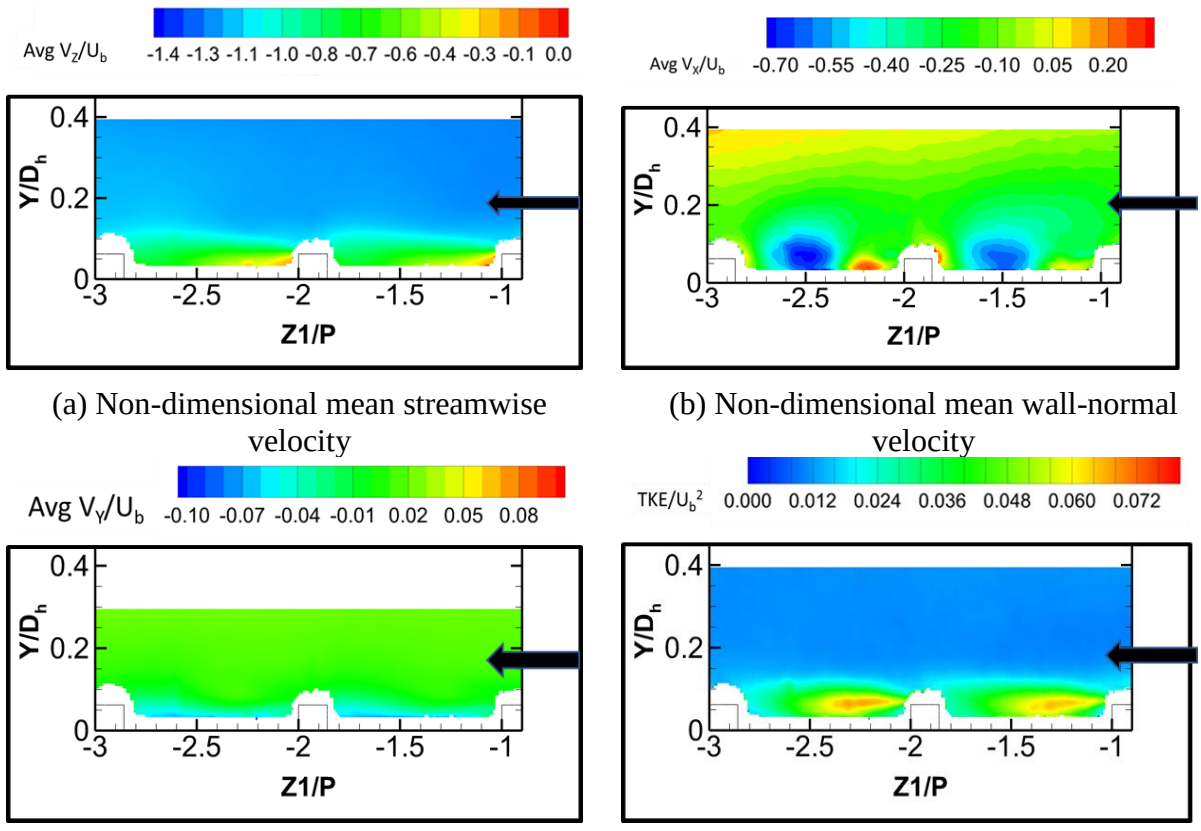

(a) Non-dimensional mean streamwise velocity

(b) Non-dimensional mean wall-normal velocity

(c) Non-dimensional mean spanwise velocity

(d) Non-dimensional mean turbulent kinetic energy

Figure 28 Fully developed flow between two rib pitches at Re ≈ 30k

Figure 29 (a)-(c) show the comparative results of non-dimensional mean velocity components between stereo PIV and LES in the streamwise mid-plane at Re ≈ 30k. The top row shows the PIV results. Since PIV results confirm that the flow is fully developed, only the results of the first rib pitch are used for the comparison. Figure 29 (a)-(c) clearly show that the flow is highly three dimensional near the inter-rib area.

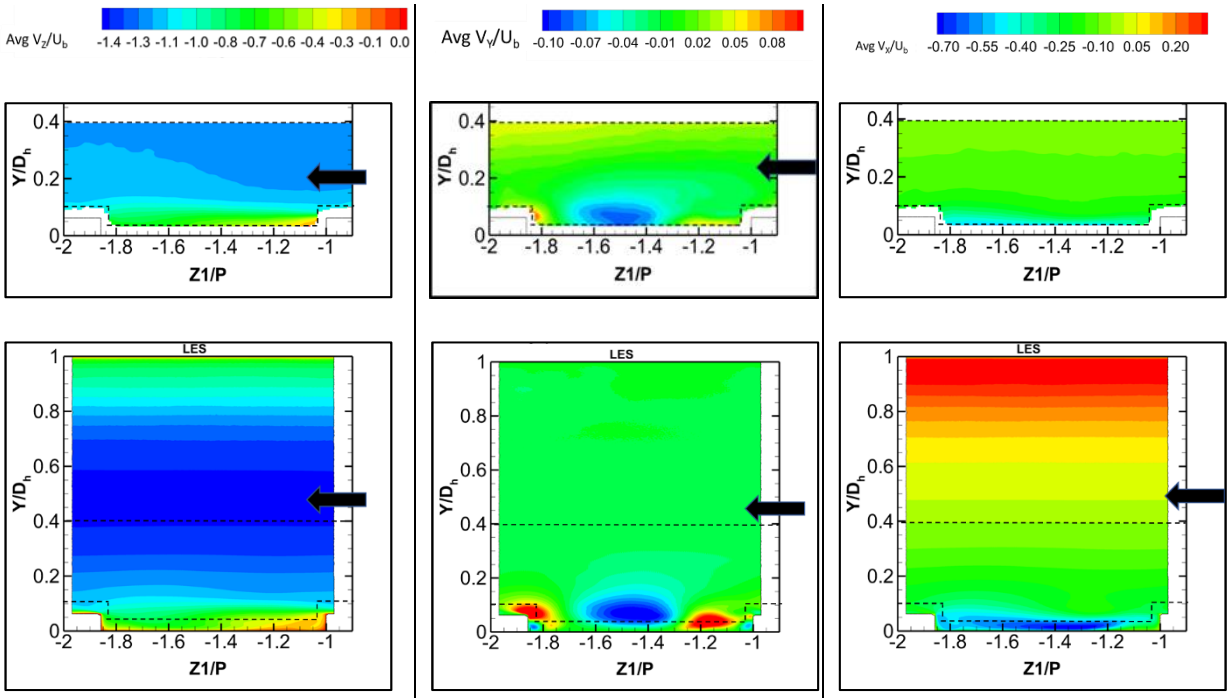

(a) Non-dimensional mean streamwise velocity

(b) Non-dimensional mean wall-normal velocity

(c) Non-dimensional mean spanwise velocity

Figure 29 Comparative results of mean velocity components between PIV and LES at Re ≈ 30k at the streamwise midplane.

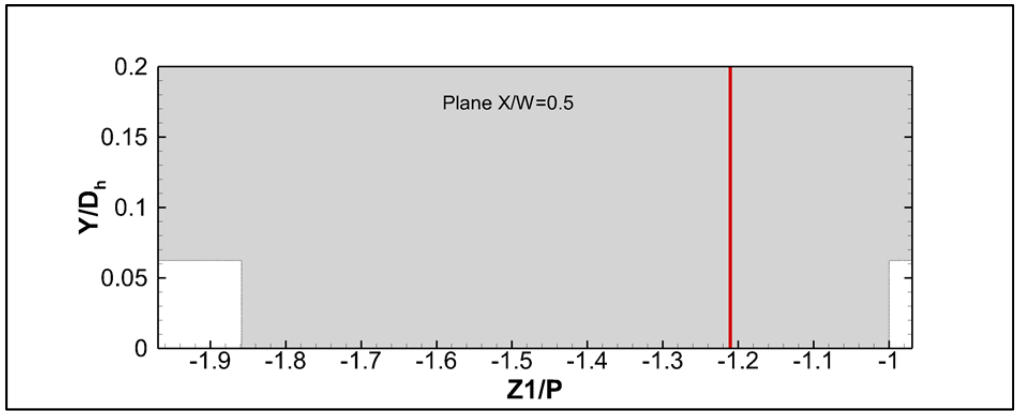

Figure 30 Location for |*Z1/P*| = 1.21

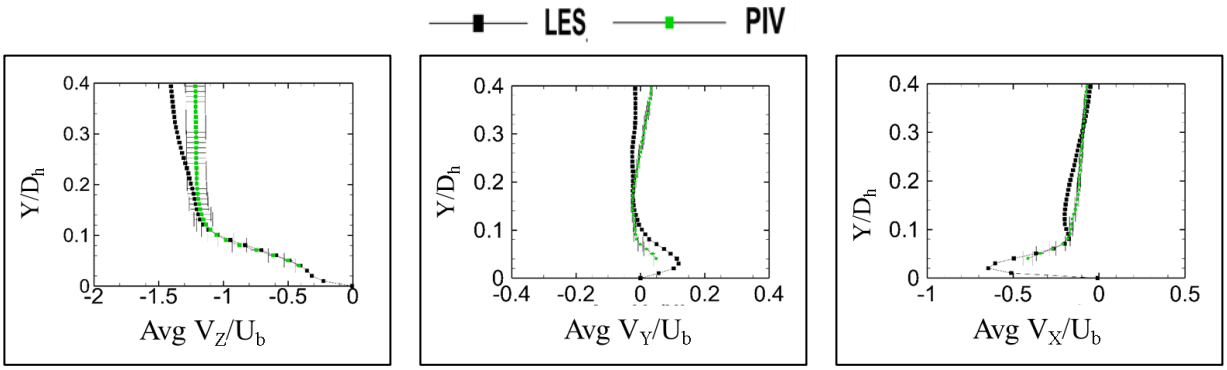

Loc $\left|\frac{Z1}{P}\right|$ = 1.21 at the streamwise midplane

Figure 31 Comparative mean velocity results between LES and PIV at Re ≈ 30k

Figure 31 shows the comparative time average velocity results between LES and the experiment at $\left|\frac{Z1}{P}\right|$ = 1.21. The location of the $\left|\frac{Z1}{P}\right|$ = 1.21 has been shown in Figure 30. This location lies in the separated shear layer region which is shown in the later section. The LES results match the experimental data of mean streamwise velocity well, especially near the rib region. However, LES shows a larger gradient of V_Z in the Y direction, which is not observed in the experimental results. The velocity profiles obtained by stereo PIV are very flat, shows almost no gradient in the Y direction above $\frac{Y}{D_h}$ = 0.15. LES shows a higher (~ 15.5%) core velocity than the PIV data. Experimental results show that the core velocity is ~ 1.2U_b, whereas, LES predicts the core velocity ~ 1.4U_b. The different RANS turbulence models also show similar results to LES data which is shown in Figure 32 (a). To ensure the accuracy of the stereo PIV results, another 2D PIV experiment was conducted for the streamwise midplane. In this 2D PIV set up, the camera was placed orthogonally to the measured plane which is an ideal set up for planer PIV measurement and provides the most accurate results. Due to the obstacles created by the ribs, the measurement

could not be achieved in the inter-rib space with this setup, but the flow field away from the ribs was measured. The streamwise mean velocity V_Z of the 2D planer PIV results corroborate to the stereo PIV data. The set up for the planer PIV and its results are presented in the Appendix D. We conjecture that the LES, as well as, all RANS predicts more parabolic shape streamwise velocity profile due to the applied fully developed interface at the inlet and outlet of the CFD domain.

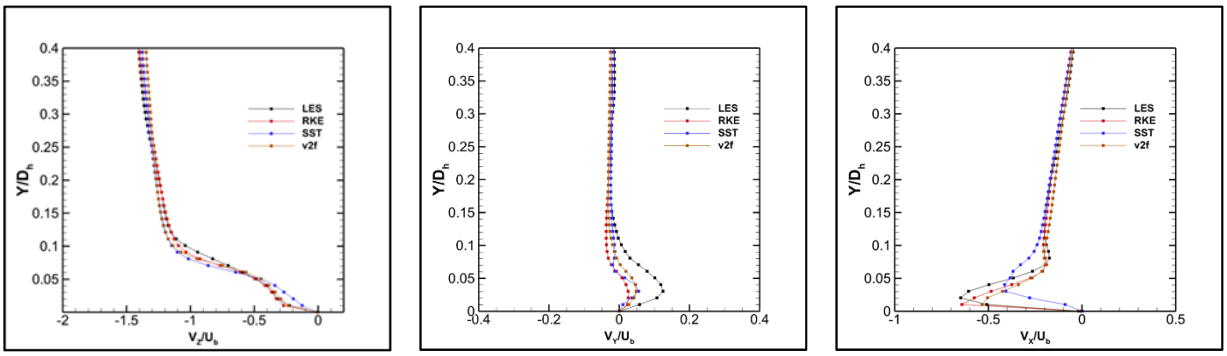

(a) (b) (c)

Loc $\left|\frac{Z1}{P}\right|$ = 1.21 at the streamwise midplane

Figure 32 Comparative mean velocity results between LES and different RANS models at Re ≈ 30k

The basic characteristics of the flow in a ribbed channel are found in different literatures [33, 38, 45]. As the ribs cause a reduction of the cross-sectional area, the flow acceleration occurs on top of them. Afterward, the flow encounters a sudden expansion and forms a recirculation zone behind the ribs. Then if there is enough space, flow reattaches and the boundary layer develops in the direction of the next rib. Figure 29 (a) shows the contour plot of the non-dimensional streamwise velocity at the streamwise midplane. In this figure, the expected recirculation zone (no reverse flow of V_Z) is not seen, but a flow retardation is evident behind the ribs. This is because, in such

angled ribs, the separated recirculating vortex moves along the ribs and the X - Z coordinate system is not a proper representative coordinate system to capture it. To detect the recirculating secondary flow structure, a new coordinate system $X' - Z'$ is introduced. The direction of X' and Z' is parallel and normal to the ribs, respectively as shown in Figure 33.

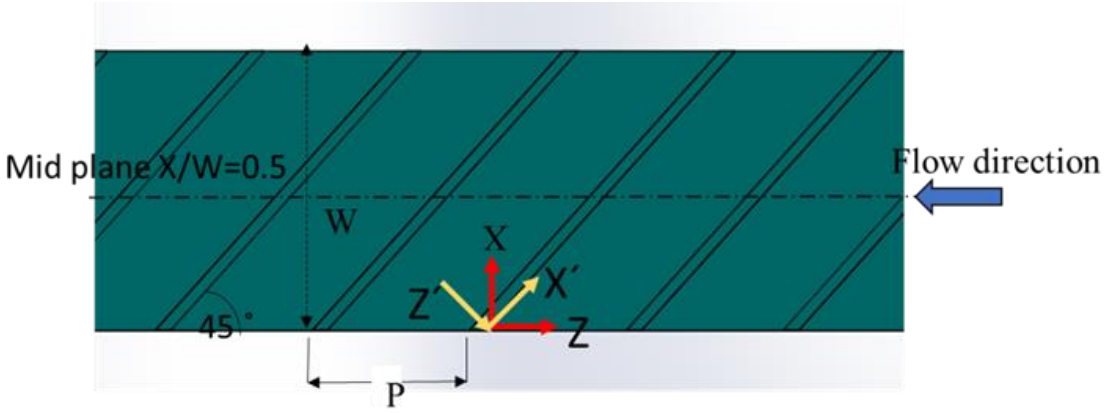

Figure 33 Coordinate system X'-Z'

The velocity components V_X' (in the X' direction) and V_Z' (in the Z' direction) were determined by the coordinate transformation of vector components method using the velocity V_X (in the X direction) and V_Z (in the Z direction). The method for the two-dimensional coordinate transformation of vector components is described in Chapter 4. Figure 34 shows the contour plot of mean V_Z' in the streamwise midplane obtained by LES. The streamlines clearly display the recirculation regions in Figure 34. As mentioned earlier, flow experiences an acceleration on the ribs' top surface with a subsequent sudden expansion behind the ribs. Consequently, the flow separation occurs and a wide recirculation zone V1 behind the ribs is observed. This is called rib induced vortex often mentioned in the literature. This vortex is accompanied with another small

counter-rotating vortex V2 at the lower corner behind the ribs. There is another flow separation region V3 is detected in front of the next rib. Later the flow hits the next rib, the flow deflects and another separated zone V4 forms on top of the ribs.

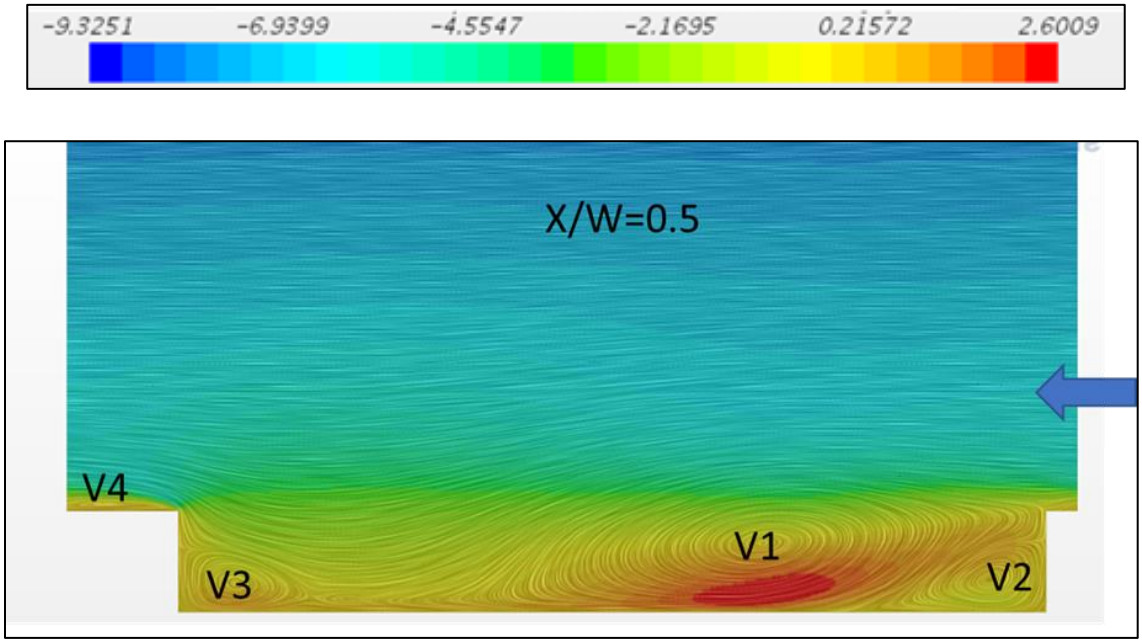

Figure 34 LES results of mean velocity $V_Z^{'}$ in the streamwise midplane at Re ≈ 30k

The LES results of non-dimensional wall normal velocity component shown in Figure 29 (b) display consecutive positive-negative velocity zones which are associated with the rib induced secondary vortices. There is a slight negative normal velocity (associated with vortex V2) zone at the lower corner of the ribs followed by a small positive normal velocity zone which is caused by both V1 and V2. Afterward, there is a wide zone of negative normal velocity at the middle of the rib pitch related to the vortex V1. There is again a positive and negative normal velocity zone just upstream of the next ribs associated with the vortex V3. The experimental results corroborate the

LES results very well which is also observed in Figure 31 (b). There is a slight discrepancy in mean normal velocity in the core flow between experiment and LES results. The experiment shows a slight positive normal velocity in the core which can be caused by the unaccounted measurement bias uncertainty due to the unfavorable highly asymmetric camera angle of the current stereo PIV setup.

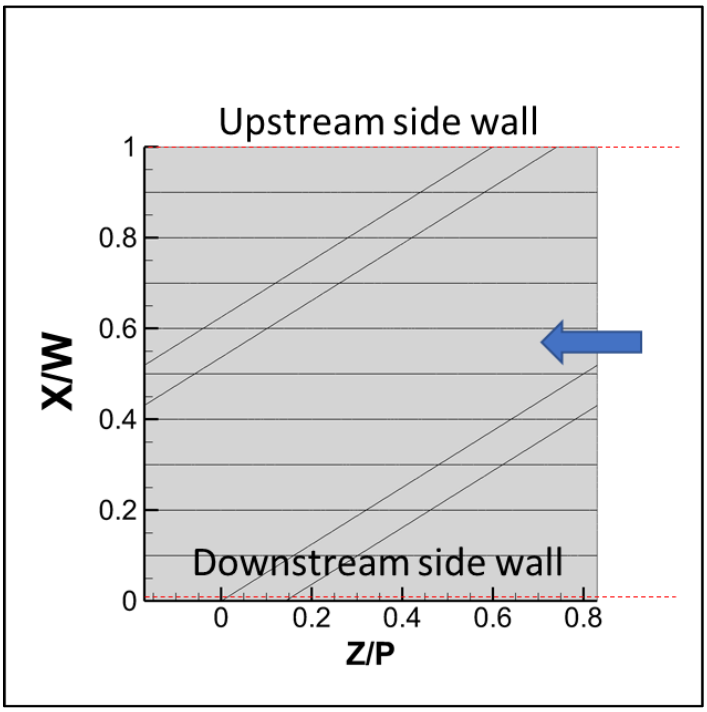

Figure 35 Streamwise plane locations

It is found that rib's inclination angle strongly guides the secondary flow vortices. The vortex, V1 begins from the intersection of the trailing face of the rib and upstream side wall (in this case, right wall), and moves toward the downstream side wall (left wall) diagonally following a spiral path. This is also evident in the nondimensional mean spanwise velocity (V_X) contour plot shown in

Figure 29 (c). There exists a negative zone in the inter-rib space, which indicates that the secondary recirculating flow travels toward the downstream side wall. The streamwise and spanwise mean velocity components in the inter-rib space are very similar in order of magnitude (see Figure 29). This, along with other reasons, limits the current study to use simpler 2D planer PIV measurement by placing the camera axis along the ribs. This high out of plane motion (V_X) can cause an irrecoverable error in the measured data with the 2D planer PIV with a non-orthogonal camera set up. The comparative results of mean normal and spanwise velocity components between LES and different turbulence models are shown in Figure 32 (b) and (c), respectively. It is observed that the RKE and v^2-f turbulence model predict the mean velocity components better than the SST k-ω turbulence model.

The flow data at the nine different streamwise planes ($\frac{X}{W}$ = 0.9-0.1) were extracted from the LES results. The locations of the extracted planes are shown in Figure 35. Among these planes, the $\frac{X}{W}$ = 0.9 is the nearest to the upstream side wall and $\frac{X}{W}$ = 0.1 is the furthest plane from it. The non-dimensional mean velocity $V_Z^{'}$ in the different planes ($\frac{X}{W}$ = 0.9-0.1) are shown in Figure 36. Note that, the local coordinate $Z1$= -1 starts from the trailing edge of the rib for each plane. As the vortex moves along the rib, the center of the vortex V1 moves away from the ribs, causing larger vortex size. Simultaneously, the other vortices, V2 and V3 also grow as those advance toward the downstream side wall. Eventually, the secondary flow approaches close to the downstream side wall, the streamlines impinge on the downstream side wall and merge with the main flow. The dissipation of the vortices is observed to start at $\frac{X}{W}$ = 0.3.

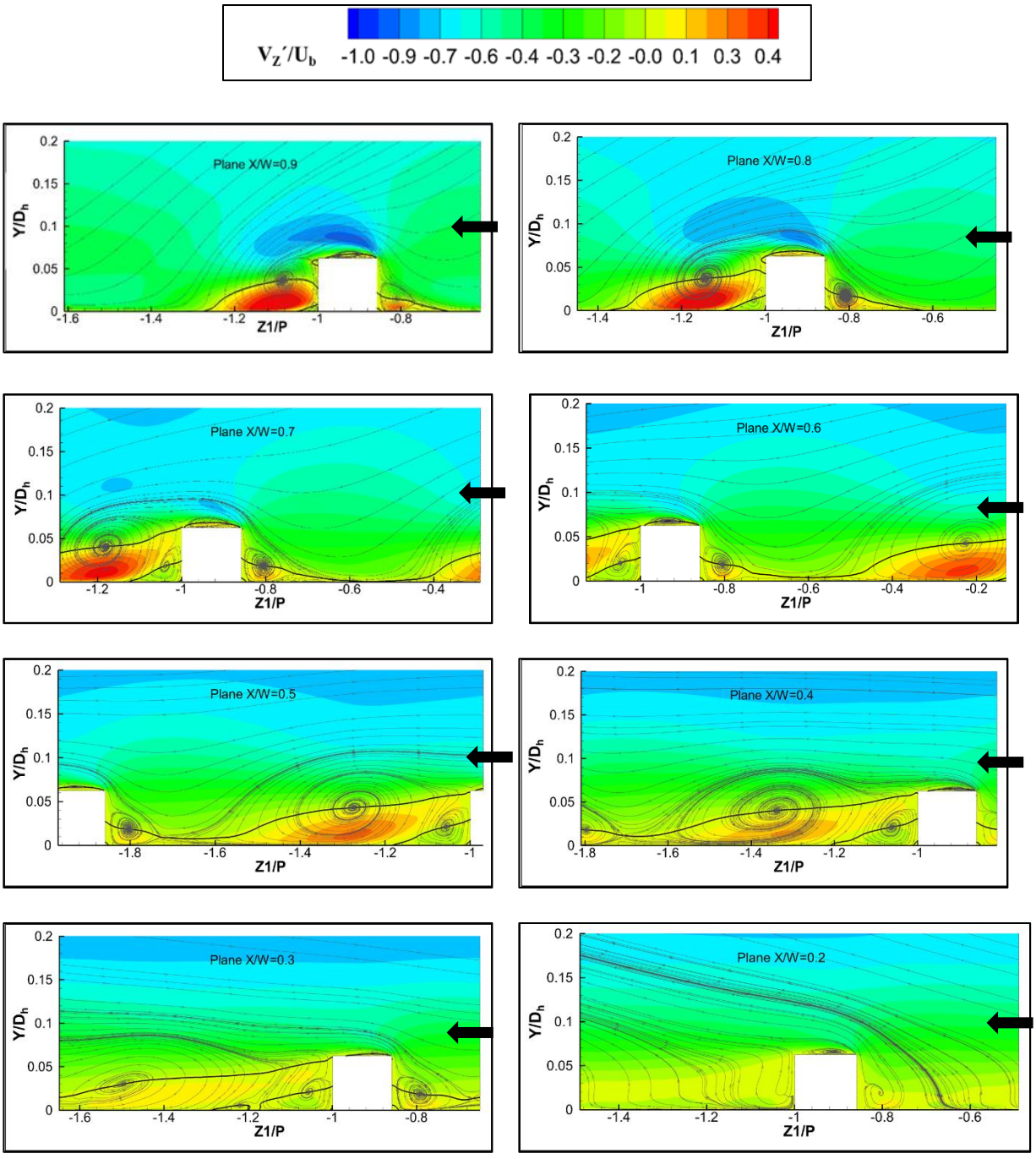

Figure 36 Non-dimensional V_Z' at different streamwise planes obtained by LES

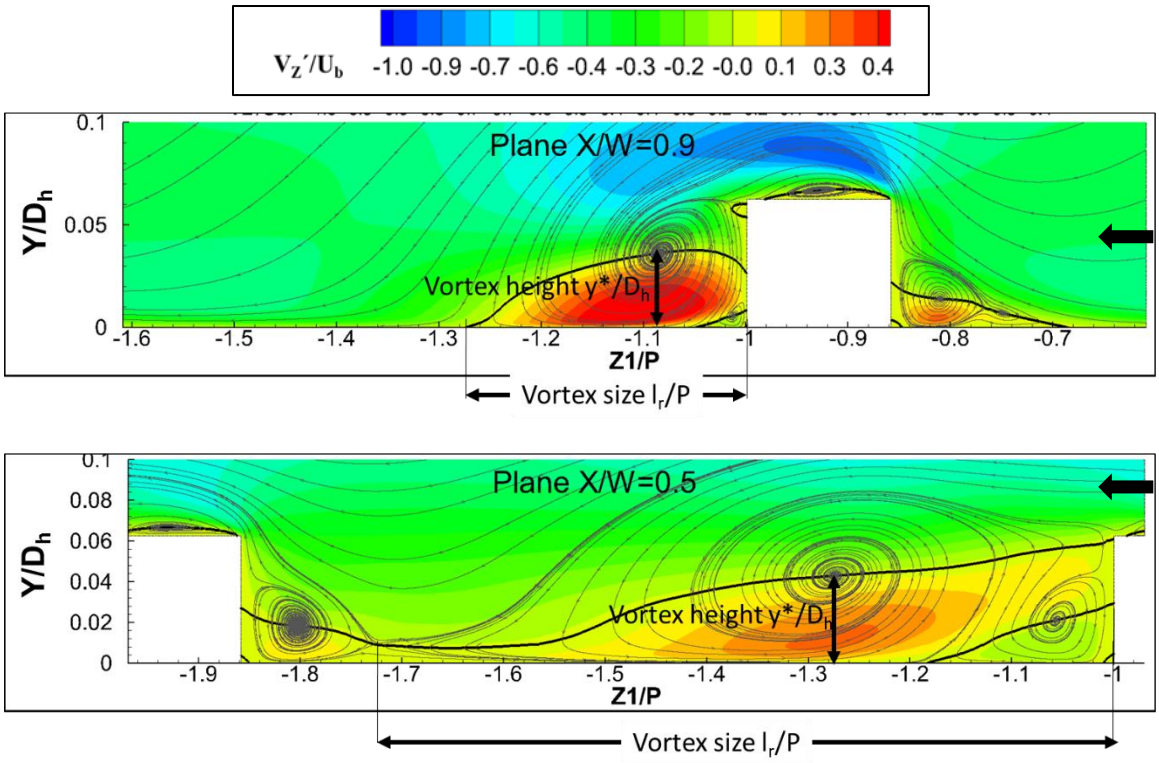

Figure 37 Reattachment length and size of the vortex V1

Figure 37 shows the close view of the recirculation zone in the planes, $\frac{X}{W}$ = 0.9 and $\frac{X}{W}$ = 0.5. An isoline $V_Z^{'}$ = 0 is shown by the solid black line to detect the extent of the vortices. In the plane $\frac{X}{W}$ = 0.9, the recirculation zone V1 is observed to reattach at $\left|\frac{Z1}{P}\right|$ ~ 1.27. However, the recirculation zone V1 is seen not to be reattached in the plane $\frac{X}{W}$ = 0.5. Instead, a saddle point observed between the vortex V1 and V3 at this plane. The recirculation vortex V1 shows a reattachment only for $\frac{X}{W}$ = 0.9-0.8 planes. The rest of the planes do not indicate any reattachment of vortex V1. The extent or size of the vortex V1 is denoted by $\frac{l_r}{P}$. Figure 38 shows the size and the height of the core ($\frac{y^*}{D_h}$) of vortex V1 at different streamwise planes ($\frac{X}{W}$ = 0.9-0.3). The figure clearly depicts that the vortex

V1 grows continuously larger as it advances toward the downstream lateral wall. The height of the vortex core from the wall remains similar for $\frac{X}{W}$ = 0.9 and 0.8 as the vortex V1 reattaches at these planes. Past those planes, the vortex V1 starts to lift off from the wall and results in the taller vortex core from the wall. At $\frac{X}{W}$ = 0.3 vortices are observed to begin dissipation. Consequently, both the size and height of the core of the vortex begins to reduce at this plane.

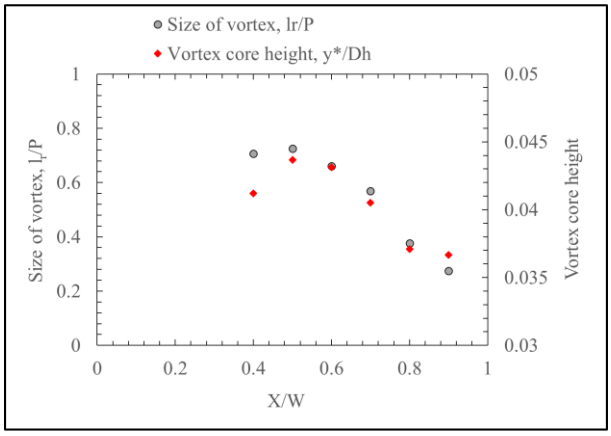

Figure 38 Size and height of vortex V1 at different streamwise planes

One of the most popular method to detect a vortex core in the flow is to determine *Q* criterion [80]. The positive value of *Q* identifies a vortex core.

$$Q = \frac{1}{2}(\|\Omega\|^2 - \|S\|^2) > 0 \tag{65}$$

Here, Ω and S are vorticity and strain rate tensor, respectively. Positive value of *Q* implies where vorticity magnitude dominates over the strain-rate magnitude.

Figure 39 (a) shows the contour of the time-averaged Q criterion values in $\frac{X}{W}$ = 0.9 and $\frac{X}{W}$ = 0.5 planes. It depicts that the vortices lose their strength (indicated by Q criterion) as they travel toward the downstream lateral wall which is displayed in Figure 39 (b).

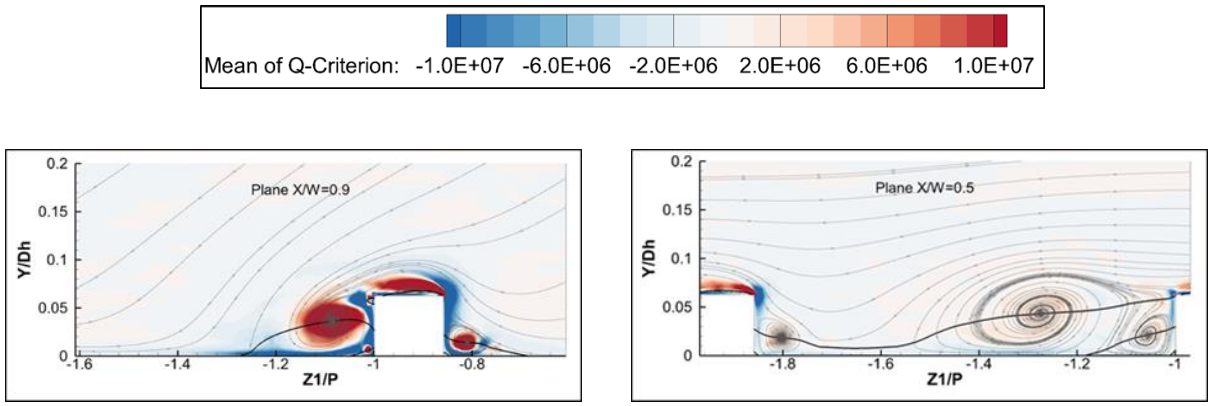

(a)

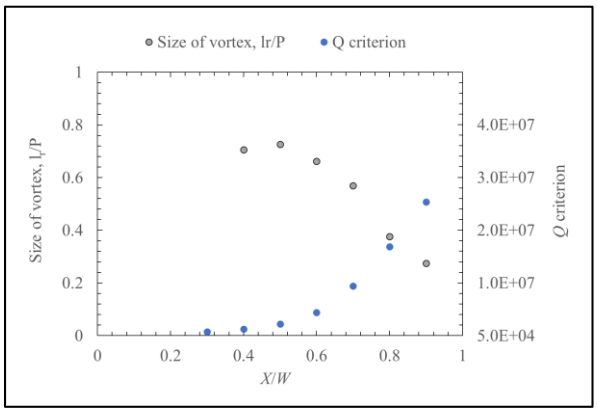

(b)

Figure 39 LES results of time-averaged Q criterion (a) Contour at X/W = 0.9 and 0.5 planes (b) At different streamwise planes

Figure 40 shows the comparative results of non-dimensional $V_Z^{'}$ at the streamwise plane $\frac{X}{W}$ = 0.8 between LES and different RANS models. All the turbulence models show the presence of the

vortices V1, V2, V3, and V4 very clearly. Figure 41 shows the comparative results of non-dimensional $V_Z^{'}$ at the streamwise midplane plane $\frac{X}{W}$ = 0.5. The vortices V1, V2, and V3 are observed to grow than those at the plane $\frac{X}{W}$ = 0.8. However, in this plane, the SST shows very different results in terms of vortex V2 and V3. The vortex V2 breaks into two smaller vortices which are not seen either in the experiment or in LES. The vortex V3 starts to merge with the vortex V1.

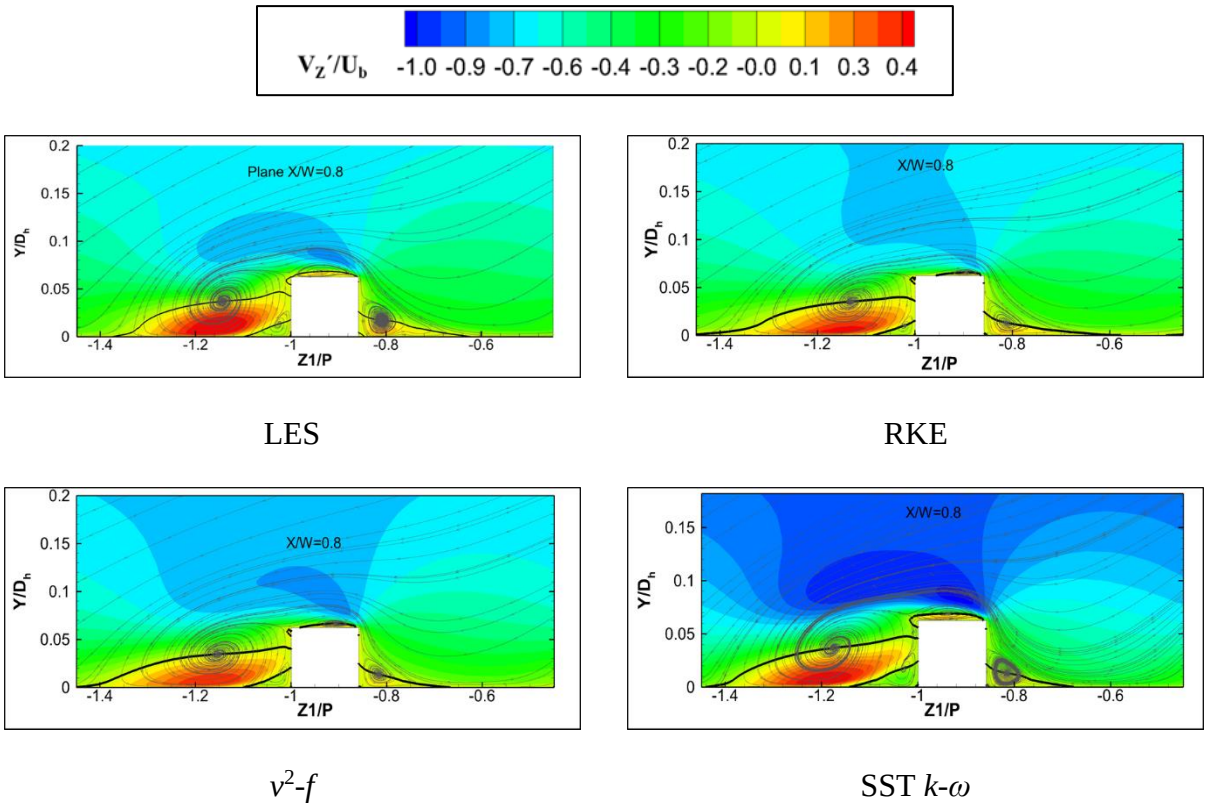

Figure 40 Comparative results of non-dimensional $V_Z^{'}$ at X/W = 0.8 plane between LES and different RANS models

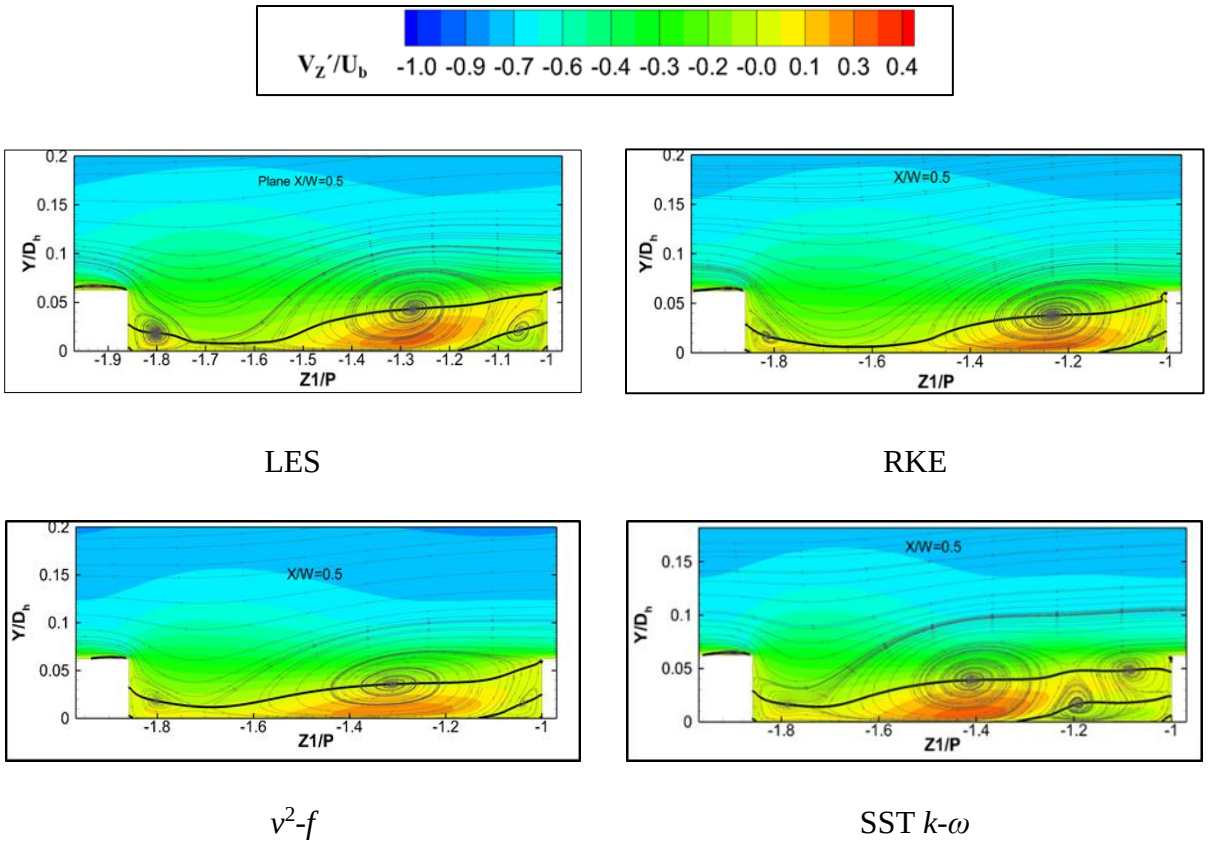

Figure 41 Comparative results of non-dimensional V_Z' at $X/W = 0.5$ plane between LES and RANS models

Table 15 Size of the vortex V1, l_r/P

Streamwise Plane	LES	v^2-f	RKE	SST k-ω
$X/W = 0.9$	0.27	0.33	0.35	0.31
$X/W = 0.5$	0.73	0.72	0.66	0.75

Table 15 presents the size of the vortex V1 predicted by LES and different RANS models at the streamwise planes, $\frac{X}{W} = 0.9$ and $\frac{X}{W} = 0.5$. Results show that all the turbulence models overpredict

the reattachment length (size of vortex V1) at the plane $\frac{X}{W}$ = 0.9. SST *k-ω* and v^2-*f* turbulence models show better match with the LES results of vortex V1 size. As it is already discussed that SST *k-ω* predicts some unphysical behavior of vortex V2 at this plane. Overall, the v^2-*f* turbulence model shows the best agreement with the LES results both quantitively and qualitatively.

Turbulent Kinetic Energy

Figure 42 shows the comparative results of the non-dimensional turbulent kinetic energy at Re ≈ 30k between LES and the PIV experiment in the streamwise midplane. In the core flow, the TKE is as low as ~ 1% of U_b^2. A strong shear layer behind the ribs is clearly observed both in the experiment and LES. The shear layer forms as the flow separates from the rib's upper surface. The shear layer possesses high turbulent kinetic energy due to the periodic flow acceleration-deceleration and separation process. High velocity gradient exists in this high turbulent kinetic energy zone. Both the experiment and LES results depict that the shear layer covers almost the full inter-rib space in this plane. The maximum strength of the shear layer exists from the leading edge of the ribs to the middle of the rib pitch ($\left|\frac{Z1}{P}\right|$ < 1.45). A deep decay of TKE is found at $\left|\frac{Z1}{P}\right|$ > 1.45 up to the leading edge of the next ribs. However, the LES results predict slightly higher maximum TKE than the experiment. Experimental results show a maximum value of TKE is ~ 6.3% of U_b^2, whereas LES predicts the maximum value of TKE ~ 7% of U_b^2 at the location $\left|\frac{Z1}{P}\right|$ = 1.21.

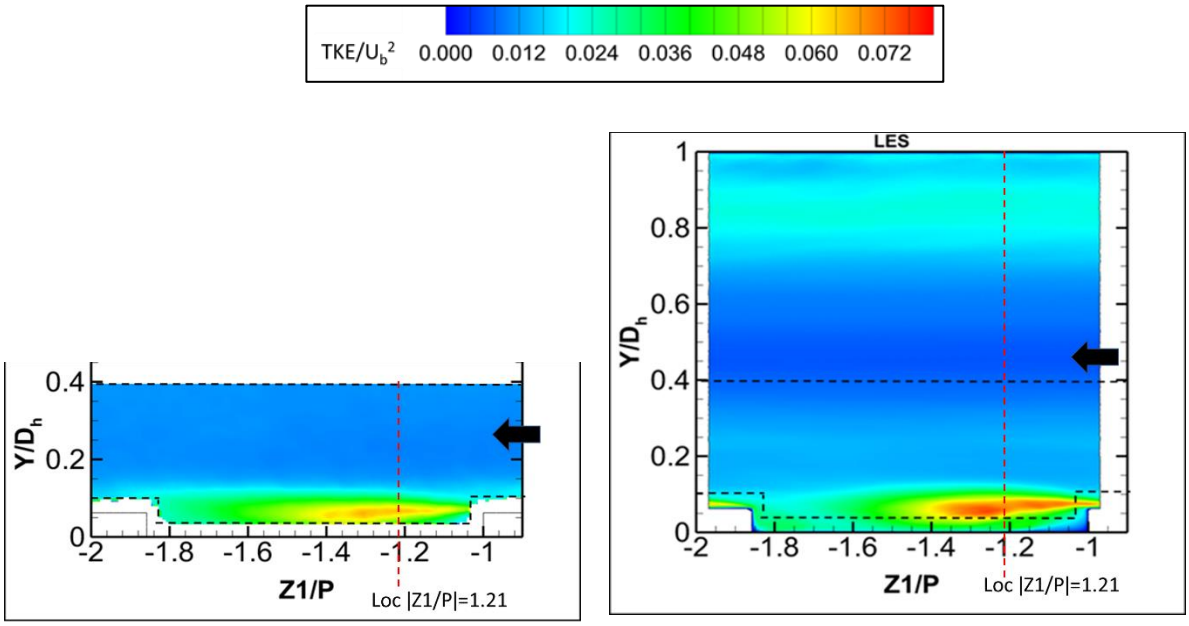

(a) PIV (b)LES

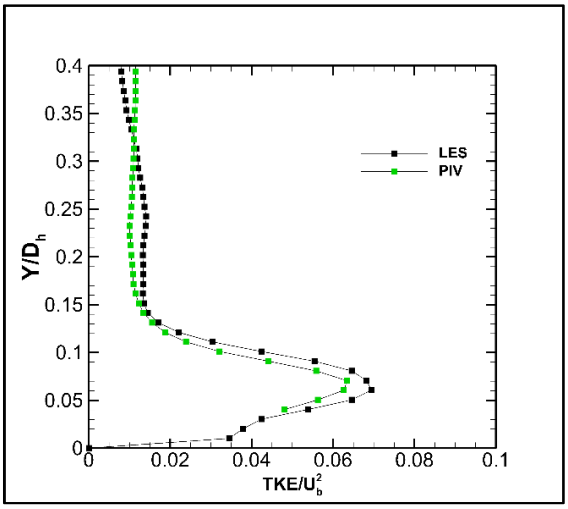

Loc $\left|\frac{Z1}{P}\right|$ =1.21 at the streamwise midplane

(c)

Figure 42 Comparative results of non-dimensional TKE between PIV and LES at Re ≈ 30k

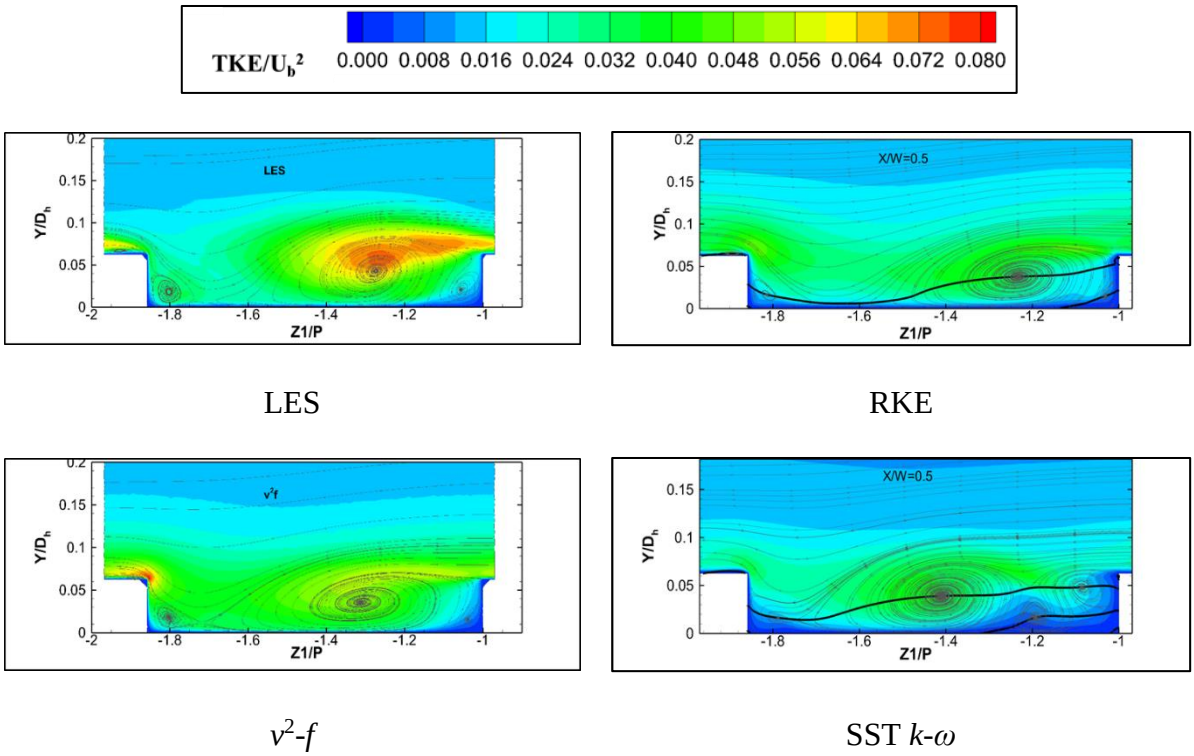

LES RKE

v^2-f SST k-ω

Figure 43 Comparative results of non-dimensional TKE at streamwise midplane between LES, SST k-ω, v^2-f, RKE

Figure 43 shows the comparative non-dimensional turbulent kinetic energy contour plots between LES and different RANS models at the streamwise midplane. All the turbulence models show the presence of a shear layer with high turbulent kinetic energy behind the ribs. The comparative results with LES show that none of the RANS models reproduce the strength of the shear layer well. All of them underpredicts the maximum value of TKE than LES. SST k-ω fails to predict the shape of the shear layer as well. Among them, the v^2-f model shows the reasonably good prediction of the shear layer both quantitatively and qualitatively. Figure 44 shows the comparative results of non-dimensional turbulent kinetic energy at $\left|\frac{Z1}{P}\right|$ =1.21.

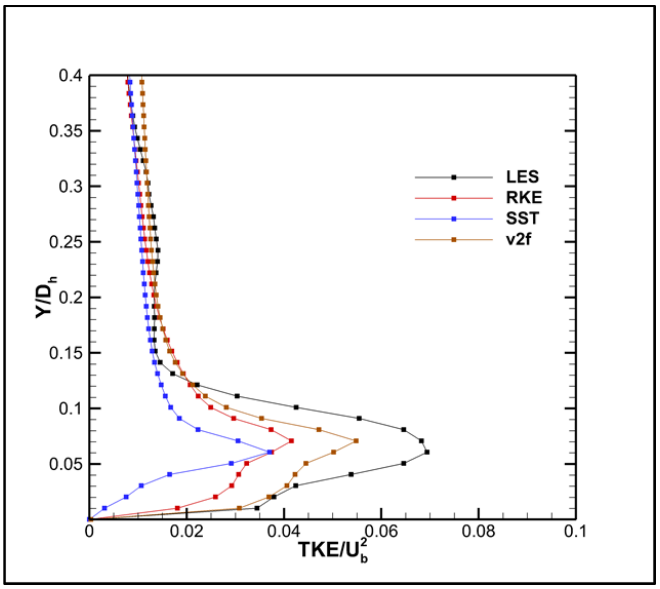

Loc $\left|\frac{Z1}{P}\right|$ =1.21 at the streamwise midplane

Figure 44 Comparative results of non-dimensional TKE between LES and different RANS models

Reynolds Stresses

The experimental and LES results of Reynolds normal stresses are shown in Figure 45 (a)-(c). The Reynolds normal stresses RZZ, RYY, RXX denotes the square of the velocity fluctuations in streamwise ($\overline{w'^2}$), wall normal ($\overline{v'^2}$), and spanwise ($\overline{u'^2}$) direction, respectively. All the velocity fluctuations are higher behind the ribs and form the high TKE shear layer. However, the streamwise fluctuations are much higher than the wall normal and spanwise ones, especially in the region of maximum strength of the shear layer. Figure 46 shows the experimental results of the non-dimensional $\overline{w'^2}$, $\overline{v'^2}$, $\overline{u'^2}$ at the location $\left|\frac{Z1}{P}\right|$ = 1.21. It clearly shows that turbulence is highly anisotropic near the ribs.

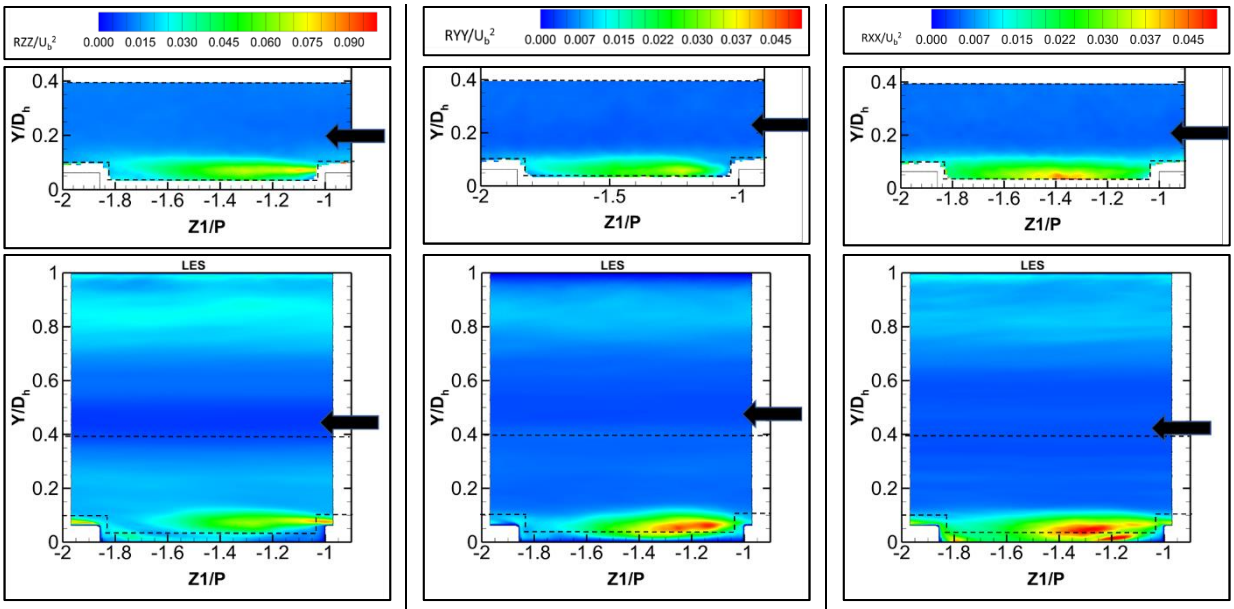

(a) Streamwise (b) Wall normal (c) Spanwise

Figure 45 Comparative results of non-dimensional Reynolds normal stresses between PIV and LES

Figure 47 shows the comparative results of all the six Reynolds stresses between the experiment and LES at $\left|\frac{Z1}{P}\right|$ = 1.21. The LES results are in excellent agreement with the experimental data. However, LES results show slightly higher maximum values for the $\overline{v'^2}$ and $\overline{u'^2}$. Figure 45 shows the maximum strength of the streamwise velocity fluctuation $\overline{w'^2}$ is ~ 8% of U_b^2 in the tested plane. The high strength of the streamwise fluctuation exists from the leading edge of the ribs up to $\left|\frac{Z1}{P}\right|$ ~ 1.25. However, the wall normal ($\overline{v'^2}$), and spanwise ($\overline{u'^2}$) velocity fluctuations shows maximum value (~ 3.5% of U_b^2) slight downstream of the ribs. There is also a higher $\overline{w'^2}$ and $\overline{u'^2}$ observed just ahead of the downstream ribs in the LES results.

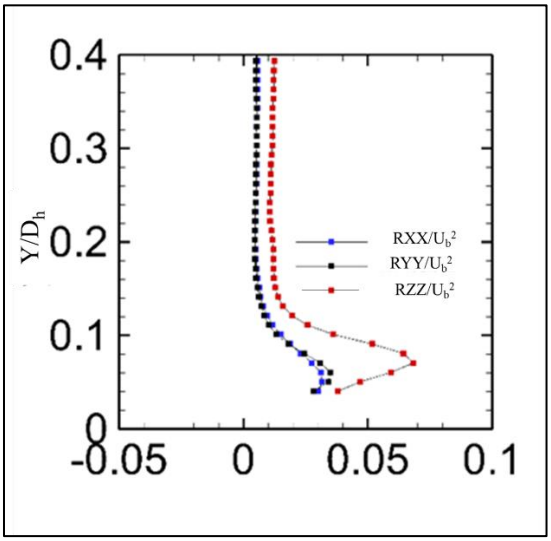

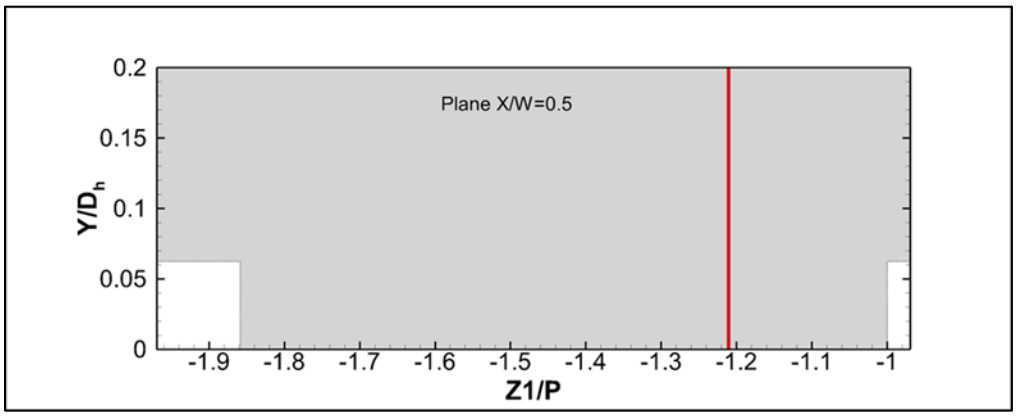

Location $\left|\frac{Z1}{P}\right|$ = 1.21

Figure 46 Turbulence anisotropy

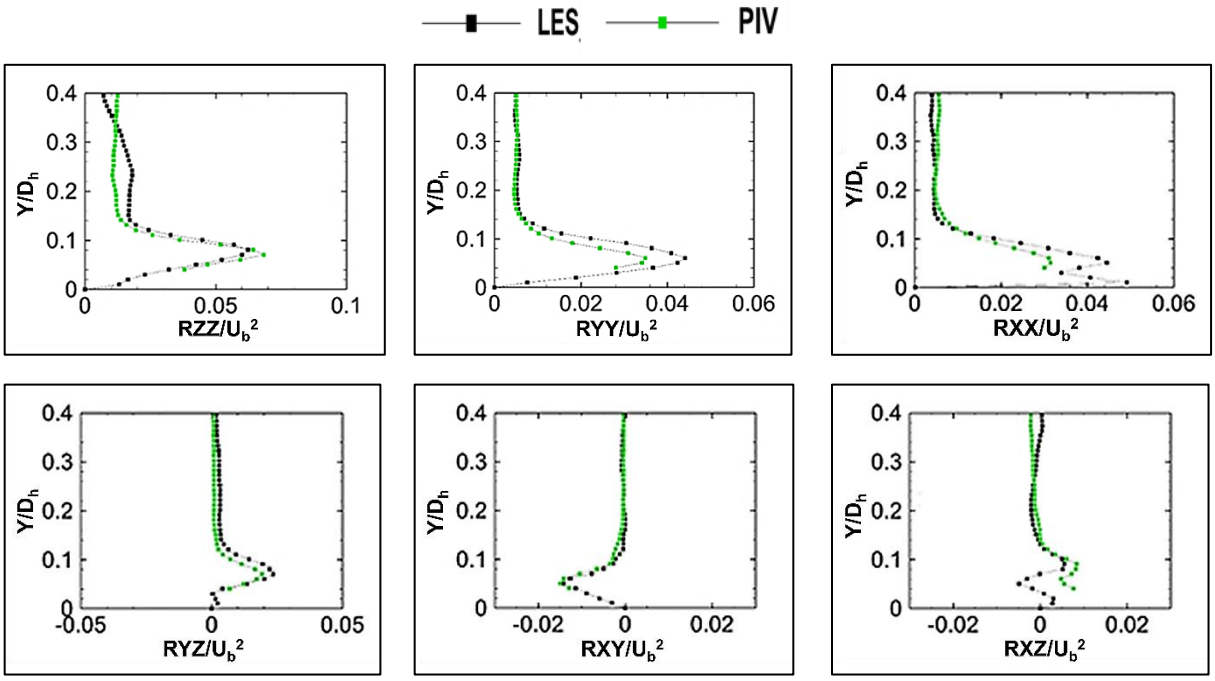

Figure 47 Comparative results of Reynolds stresses between LES and PIV at the location $|Z1/P| = 1.21$

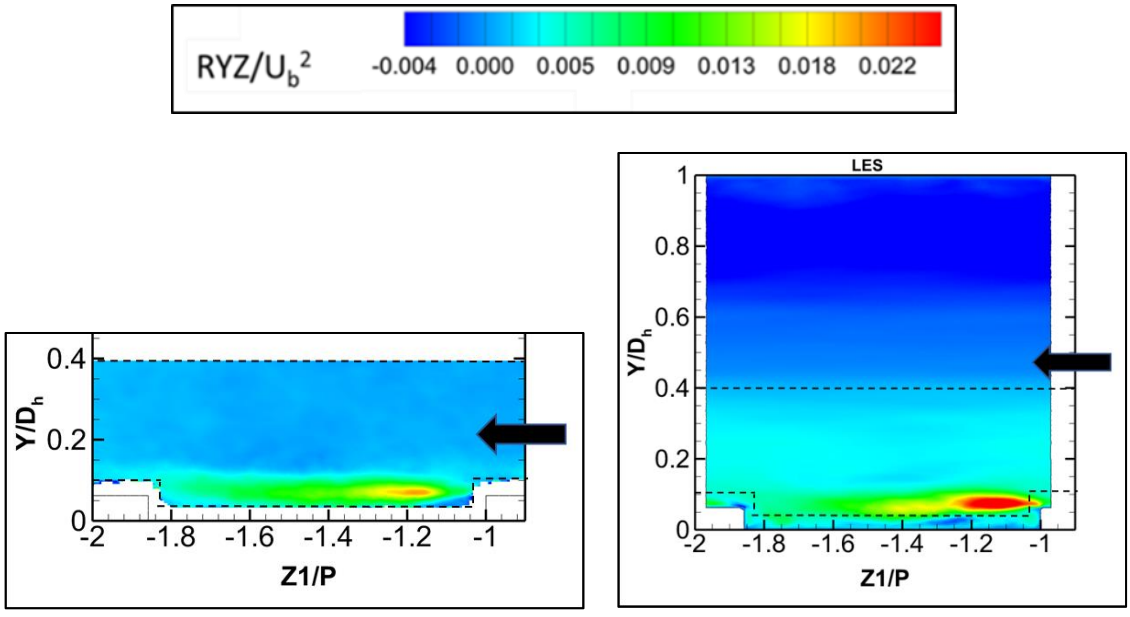

Figure 48 Comparative results of non-dimensional *RYZ* between PIV and LES

The contour of non-dimensional Reynolds shear stress ($RYZ = \overline{v'w'}$) is shown in Figure 48. The $\overline{v'w'}$ is higher in the separated shear layer. In the LES results, the maximum shear stress (~ 2.5% of U_b^2) is observed from the top of the trailing edge of the ribs up to $\left|\frac{Z1}{P}\right|$ ~ 1.25 in the shear layer. However, the experimental results show the maximum value (~ 2.2% of U_b^2) exists little behind the ribs between 1.15 < $\left|\frac{Z1}{P}\right|$ < 1.3. The comparative results of all the three components of Reynold shear stresses ($RYZ = \overline{v'w'}$, $RXY = \overline{u'v'}$, $RXZ = \overline{u'w'}$) between LES and PIV are shown in the bottom row in Figure 47. LES shows an excellent match with the experimental data, especially for RYZ and RXY.

Heat Transfer and Friction Results

The fully developed heat transfer and pressure drop behavior in the one ribbed wall case were investigated at different Re. Figure 49 (a) and (b) show the fully developed average Nu results for all the walls and the friction results, respectively. The friction results of two ribbed wall case for the sharp ribs are shown in Figure 49 (b) as well. For the fair comparison with the numerical study, the experimental results for the exact Re (= 28668) were interpolated from these data and tabulated in Table 16. The experimental uncertainties are also presented in this table.

The comparative LES and RANS results of fully developed average Nu and friction results at the same Re are tabulated in Table 17. LES shows excellent agreement with the experimental data of average Nu of the ribbed and the top wall (~ discrepancy 2%). However, it shows ~ 8% and 12% discrepancy with the Nusselt results of the left wall and right wall, respectively. Note that, the left

and right wall is the downstream and upstream side wall, respectively. The relatively coarser mesh at the side walls may cause this deviation. Note that the experimental uncertainty in the left and the right wall is ~ 4.2%. If the experimental uncertainty is considered, the prediction of LES for the left and right wall are reasonably good. LES predicts the experimental channel average Nu within ~ 5.4% deviation. Friction results also show a very good match between LES and the experiment within the experimental uncertainty.

Table 16 Experimental results of average Nu and friction factor for one ribbed wall case at Re ≈ 30k

	Re	Nu					Friction factor
		Ribbed wall	Top wall	Left wall	Right wall	Channel average	
Experiment	28668	156.4	74.8	104.8	87.1	106.1	0.061
Uncertainty	3.3%	4.6%	4.9%	4.2%	4.2%	2.3%	7.65%

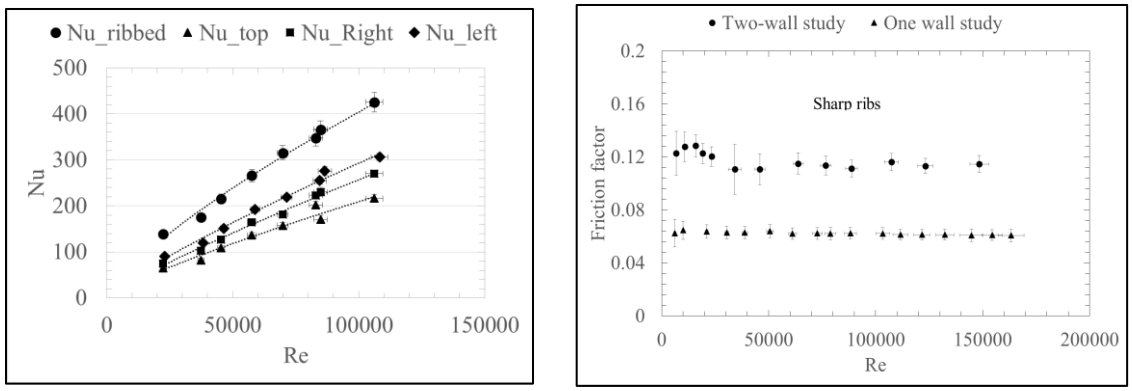

Figure 49 Experimental results of (a) Fully developed Nu (b) Friction factor at different Re for one ribbed wall case

Table 17 shows the comparative results of different turbulence models with the experiment as well as the LES. Note that both SST k-ω and RKE turbulence models underpredict the experimental results to a great extent. Among the RANS models, the v^2-f turbulence model shows the closest results to the experiment. It matches the experimental heat transfer results of the ribbed and top wall very well. This model also displays a very good match with the experimental friction data as well.

Table 17 Comparative results of average Nu and friction factor between experiment, LES and different RANS models at Re ≈ 30k (actual Re 28668)

	Nu					
	Ribbed wall	Top wall	Left wall	Right wall	Channel average	Friction factor
Experiment	156.4	74.8	104.8	87.1	106.1	0.061
LES	154.8	73.9	96.0	76.6	100.3	0.058
SST k-ω	124.9	53.6	61.0	59.8	74.8	0.049
RKE	129.2	62.0	72.8	66.6	82.7	0.054
v^2-f	156.3	72.1	85.3	76.4	97.5	0.059

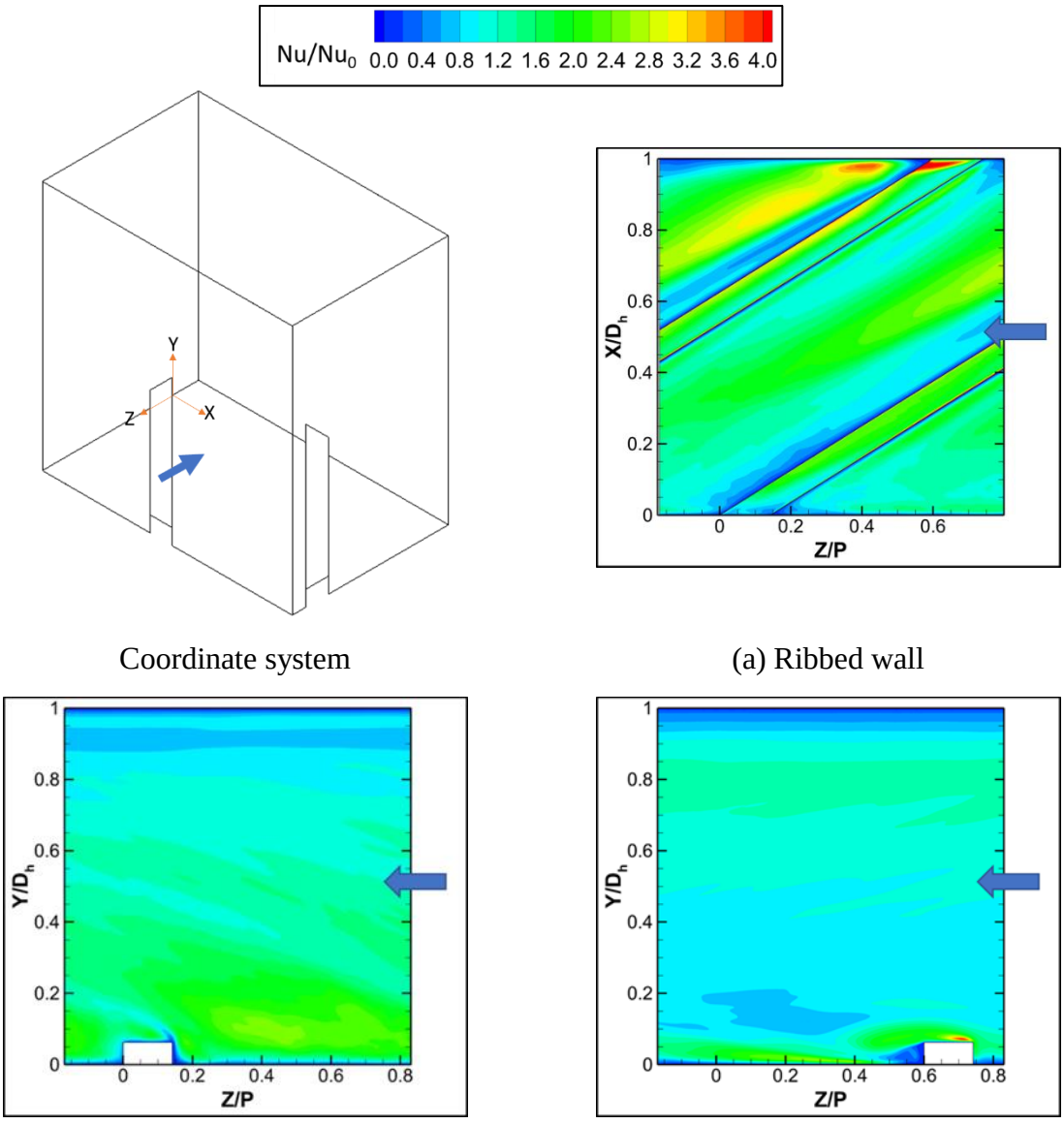

Coordinate system

(a) Ribbed wall

(b) Downstream side/ left wall

(c) Upstream/ right side wall

Figure 50 LES results of local heat transfer augmentation Nu/Nu_0

Figure 50 presents the time-averaged local Nu augmentation contour plot for ribbed and the side walls obtained by LES. The computational domain consists of one pitch only. For a better comprehension, the results are periodically transformed for two more ribs and presented in Figure 51. The Nu_0 for the smooth channel is determined by using the Dittus Boelter equation and used

for normalization of the heat transfer results. It is observed that local heat transfer is highly non-homogenous and influenced by the secondary flow induced by the ribs. The maximum heat transfer augmentation happens at the upper portion of the rib's front face because of the shear layer impingement (Figure 51 (b)). The maximum $\frac{Nu}{Nu_0}$ in this region is above 5.0. There is another high heat transfer (max $\frac{Nu}{Nu_0}$ ~ 3.7) zone noticed near the upstream side wall corner in the inter-rib space. This high heat transfer zone is caused due to the start of the rib induced recirculating vortex V1.

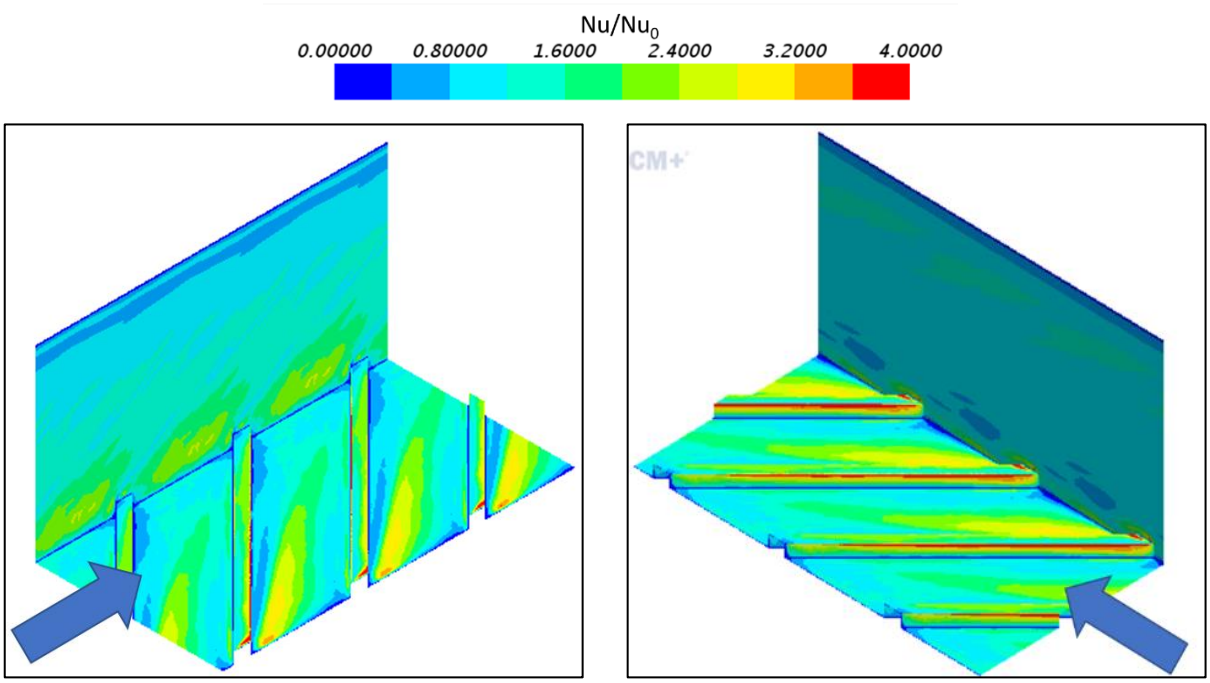

(a) (b)

Figure 51 LES results of local heat transfer augmentation Nu/Nu_0

As mentioned earlier, the recirculating vortex travels diagonally toward the downstream lateral wall following a spiral path. This helps in the exchange of energy and momentum transfer between the recirculating structure and the shear layer behind the ribs and results in high heat transfer zone in the inter-rib space. It is observed that this high heat transfer zone diverts away from the rib in the direction of the downstream side wall. The progressive contact between the flow and the wall while the recirculating structure V1 moves toward the downstream side wall causes the convective heat transfer less effective. This results in a reduction in the augmentation value in this area toward the downstream side wall. There is a narrow portion just behind the ribs where the flow is almost stagnant and moves into the small counter-rotating vortex V2 which causes a lower heat transfer zone. This lower heat transfer zone becomes wider as V2 grows while it travels toward the downstream side wall. However, the vortex V3 created in front of the downstream ribs causes a slight increase in heat transfer in this narrow area. There is a high heat transfer zone observed near the trailing edge of the top surface of the ribs due to the presence of vortex V4. There is a small zone of very high heat transfer augmentation at the corner of the rib's top surface and the upstream side wall which is as high as 5.5.

On the downstream side wall, there is an elongated high heat transfer area exists above and behind the ribs reaching augmentation ratios as high as ~ 2.5. The impingement of the streamlines of the main flow and the secondary flow results in this high heat transfer area. Figure 50 (c) also shows the Nu augmentation on the upstream side wall. The Nu augmentation on the upstream side wall is noticeably lower than the downstream side wall. This also corroborates with the experimental results shown in Table 16. On the upstream side wall, a thin area of high heat transfer ($\frac{Nu}{Nu_0}$ ~ 2.2)

is observed near the ribbed wall behind and on the rib. This is associated with the start of the vortex V1 formation behind the ribs. The maximum heat transfer augmentation (~ 3.8) on this wall occurs at its intersection with leading edge of the ribs.

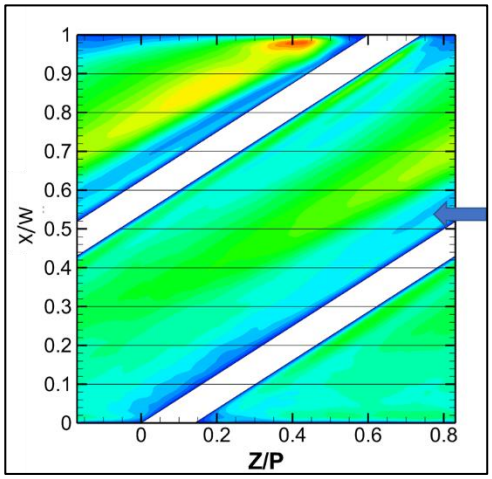

(a) Location for the streamwise polylines

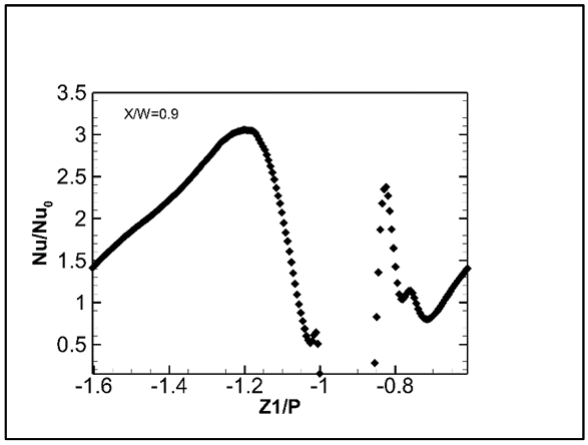

(b) at $X/W = 0.9$

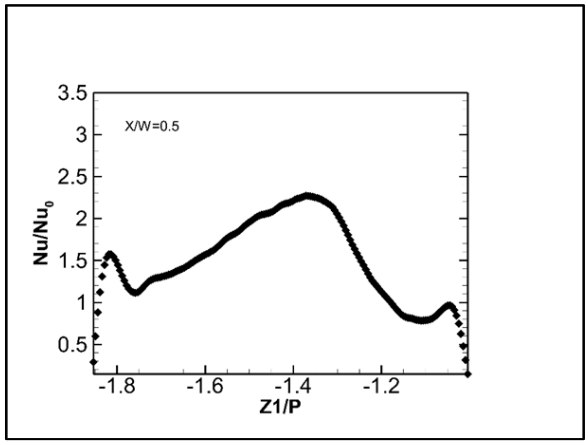

(c) at $X/W = 0.5$

Figure 52 LES results of Nu/Nu_0 on the ribbed wall along the streamwise polylines

The local heat transfer augmentation results of LES at the nine different streamwise polylines ($\frac{X}{W}$ = 0.9-0.1) on the ribbed wall were extracted as shown in Figure 52 (a). The results of the local heat

transfer augmentation for the isolines $\frac{X}{W}$ = 0.9 and $\frac{X}{W}$ = 0.5 are presented in Figure 52 (b) and (c), respectively. In these figures, the local coordinate $Z1$= -1 starts from the downstream point of the ribs for each plane. Recall that, the main flow is in -Z (or -$Z1$) direction.

Integration of the local $\frac{Nu}{Nu_0}$ was performed along the polylines as shown in Figure 53 (a). This integration denotes the total heat transfer augmentation along the polylines. Similarly, another integration was done up to vortex V1 extent on the isoline which is shown in Figure 53 (b). This value indicates the contribution of vortex V1 to the total heat transfer augmentation along the polyline. Both results are presented in Figure 53 (c). The results are calculated for $\frac{X}{W}$ = 0.9 to 0.3 as the vortex V1 starts to dissipate at $\frac{X}{W}$ = 0.2. The average $\frac{Nu}{Nu_0}$ for the polylines are also calculated and shown in Figure 53 (d). It is found that the integrated $\frac{Nu}{Nu_0}$, as well as the average $\frac{Nu}{Nu_0}$ along the polylines, decreases as the flow travel from the upstream to the downstream side wall. As mentioned earlier, the vortex V1 becomes larger while it travels toward the downstream side wall. Consequently, the integrated $\frac{Nu}{Nu_0}$ up to the vortex extent V1 continuously increases from $\frac{X}{W}$ = 0.9 to 0.5. Afterward, the vortex size decreases and results in a reduction in integrated $\frac{Nu}{Nu_0}$ up to vortex extent as well. However, the average $\frac{Nu}{Nu_0}$ up to the vortex V1 extent also shows a continuous reduction from $\frac{X}{W}$ = 0.9 to 0.3. Close to the upstream side wall at $\frac{X}{W}$ = 0.9, the contribution of vortex V1 is ~ 37% to the total heat transfer augmentation. While $\frac{X}{W}$ moves from 0.9 to 0.5, the contribution of vortex V1 to the total heat transfer increases continuously. At $\frac{X}{W}$ = 0.5, almost 90%

of total heat transfer is associated with the vortex V1. Past $\frac{X}{W}$ = 0.5, the vortex V1's contribution starts to reduce again.

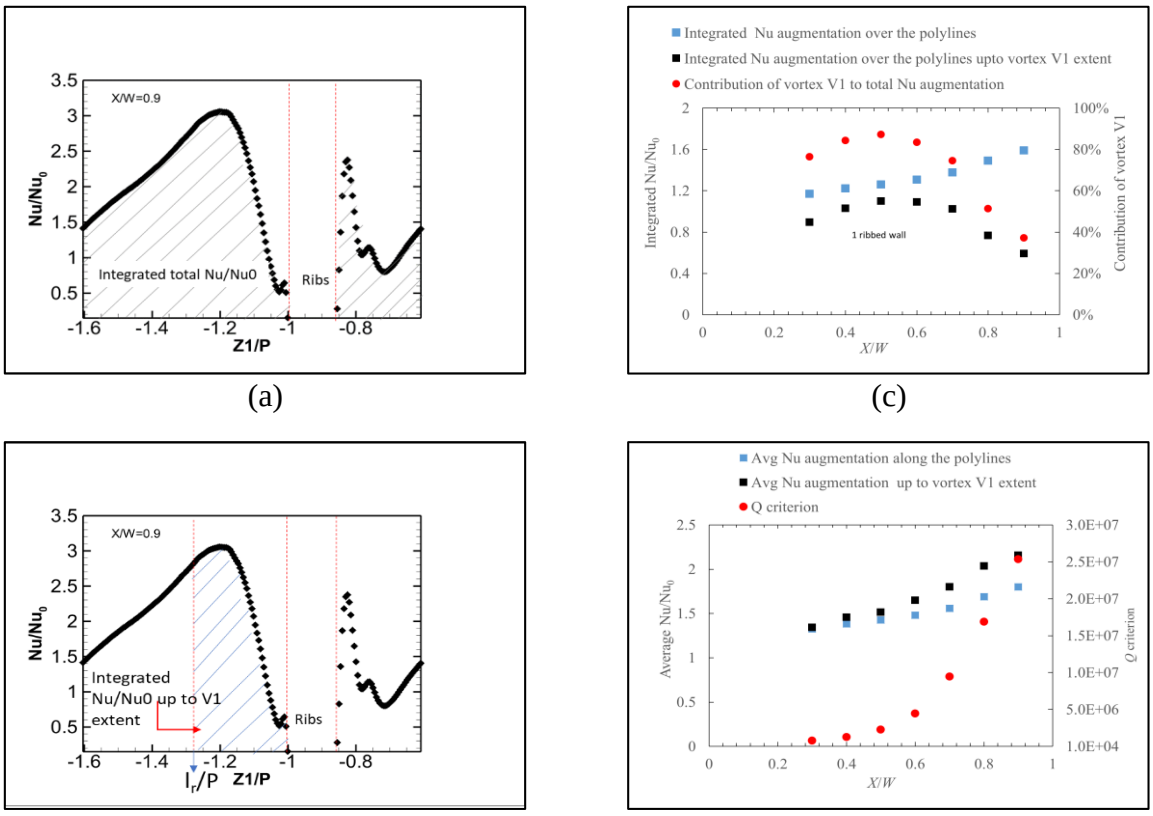

Figure 53 (a)-(b) Area under Nu/Nu_0 vs. $Z1/P$ curve (c) Integrated Nu/Nu_0 (d) Average Nu/Nu_0 along the streamwise polylines

Effect of Re

The in-plane velocity components of the streamwise mid-plane were measured by PIV for Re ≈ 10,000-150,000. The velocity components were transformed to $X' - Z'$ coordinates as shown in Figure 33. Figure 54 presents the non-dimensional V_Z' at the different Re. The rib induced vortex

V1 is clearly visible for all the Re. The other vortices, such as V2, V3, and V4 could not be captured due to lack of data measured very close to the wall. As Re increases from Re ≈ 10k to 70k, the vortex V1 shrinks toward the rib's trailing edge, yielding in smaller vortex size. The height of the vortex core also observed to move up slightly as Re increases from Re ≈ 10k to 70k. The size and height of the vortex core remain invariant at Re ≥ 70k.

Figure 55 shows the experimental non-dimensional turbulent kinetic energy in the streamwise midplane for different Re. The core flow shows similar TKE for all the Re which is around 1% of U_b^2. Reynolds number has a significant influence on the rib generated shear layer regarding the size, and the TKE value. At the lower Re, the shear layer is found to cover the full inter-rib space. As Re increases, the shear layer shrinks toward the upstream rib up to Re ≈ 70k. For example, the high turbulent kinetic energy shear layer covers the full inter-rib space at Re ≈ 10k-30k, but it spreads up to $\left|\frac{Z1}{P}\right|$ ~ 1.4 at 50k ≤ Re ≤ 150k. The value of the non-dimensional TKE of the shear layer is found to decay with the increasing Re up to Re ≈ 70k. The maximum strength of the non-dimensional TKE reduces from 0.07 to 0.05 as Re increases from Re ≈ 10k to 70k. However, the maximum value of the non-dimensional TKE is observed to rise at Re ≈ 100k and 150k. This can attribute to the higher uncertainty in the PIV measurement at high Re cases due to fogging or pulling off the oil.

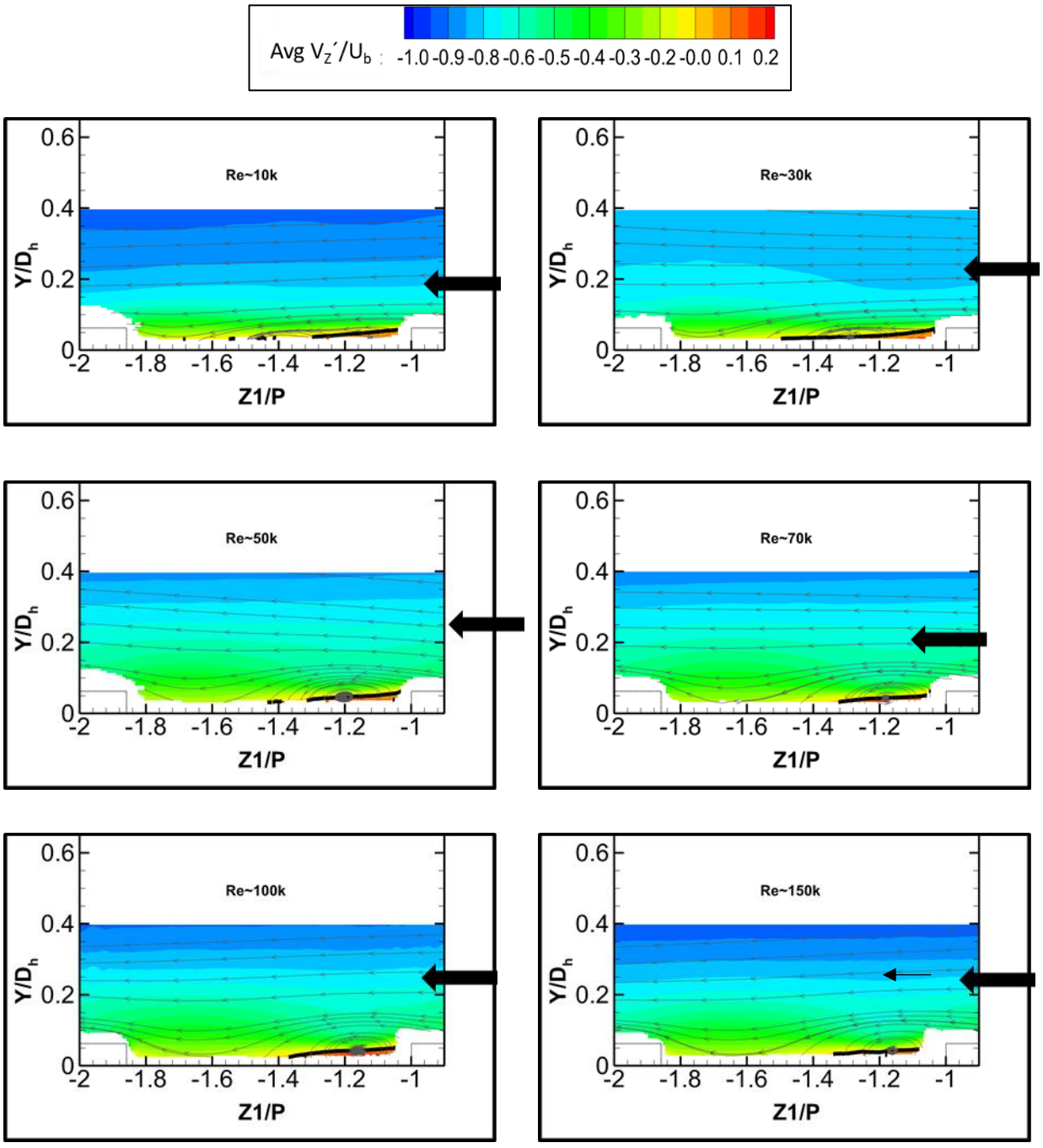

Figure 54 PIV results of the non-dimensional V_Z' at the streamwise midplane at different Re

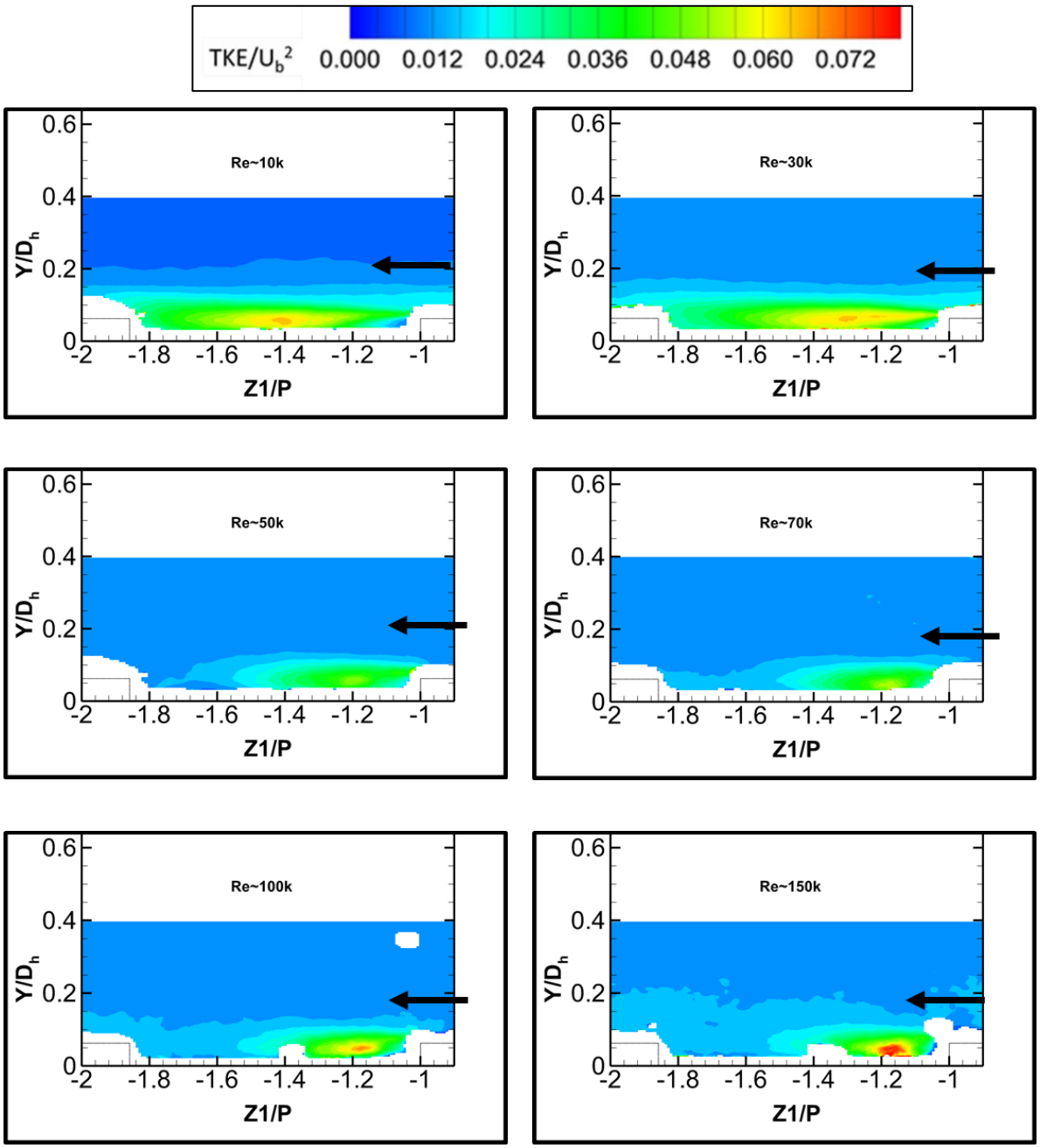

Figure 55 PIV results of the non-dimensional turbulent kinetic energy at different Re

CHAPTER 8: AEROTHERMAL ANALYSIS OF SHARP AND ROUND RIBS

The comparative results of fully developed average heat transfer and friction results between the sharp and round ribs (two ribbed walls) are discussed in Chapter 6. The detailed flow and heat transfer results for the sharp ribs for one wall study has been discussed in Chapter 7. This chapter discusses the comparative effect of the sharp and round ribs (two ribbed wall cases) on the flow behavior and the consequent impact on the heat transfer and pressure drop behavior. No experiment was conducted to investigate the flow behavior for both the sharp and round cases of the two ribbed wall study. Therefore, the flow behavior for these cases is analyzed with the help of the numerical results. It is found in Chapter 7 that the v^2-f model predicts the experimental flow behavior best among the RANS models. Hence, the v^2-f turbulence model has been chosen for this purpose. The analysis is done at Re ≈ 52,000. The coordinate system for the computational domains for both cases is shown in Figure 56.

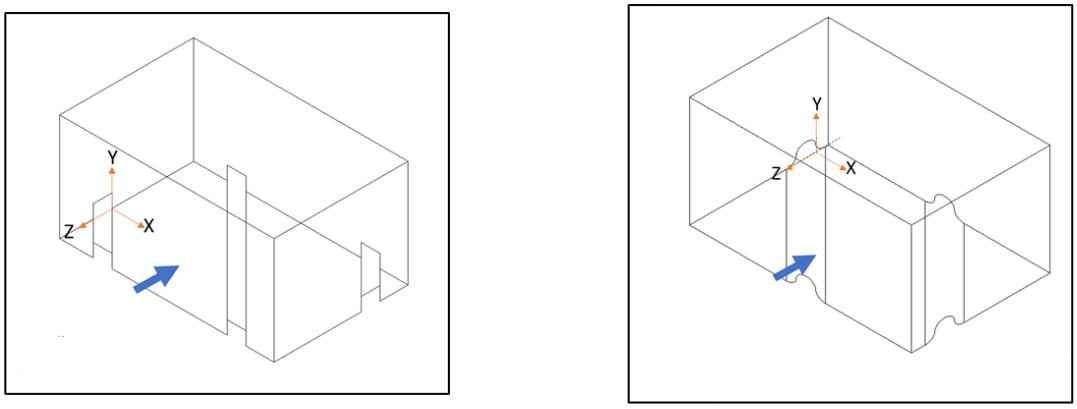

Sharp ribs Round ribs

Figure 56 Coordinate System for the computational domains

Flow Behavior Analysis

To analyze the comparative flow behavior for sharp and round ribs, the flow field results at the nine streamwise planes were extracted as shown in Figure 57. Similar to the one ribbed wall case described in the previous chapter, the velocity components were transformed to the $X^{'} - Z^{'}$ to capture the secondary vortices. Figure 58 and Figure 59 show the comparative results of non-dimensional $V_Z^{'}$ between the sharp and round ribs at the streamwise planes, $\frac{X}{W}$ = 0.9 and $\frac{X}{W}$ = 0.5, respectively. In these figures, the local coordinate $Z1$= -1 starts from the trailing edge of the rib for each plane.

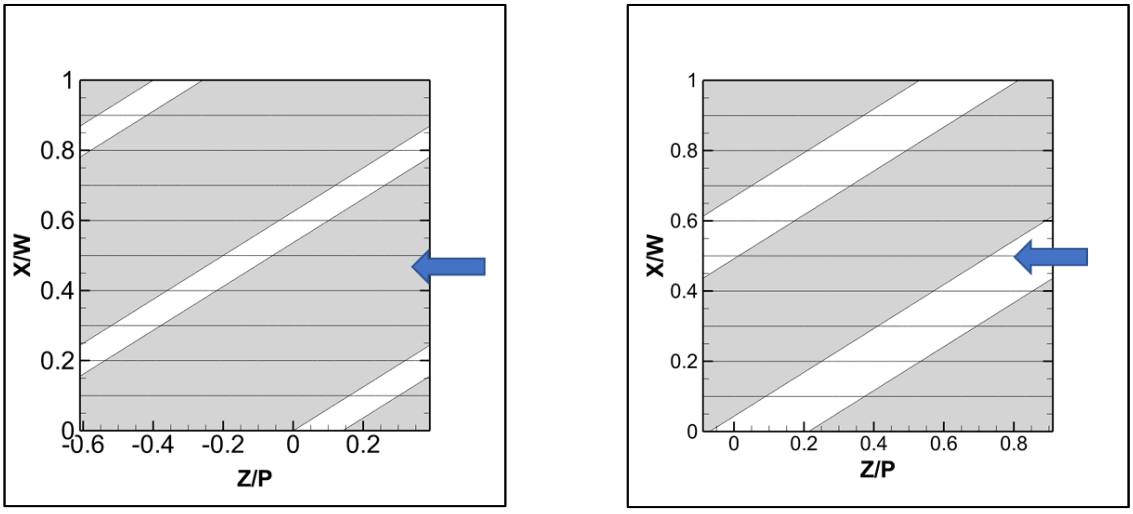

Sharp ribs Round ribs

Figure 57 Location of the streamwise planes for sharp and round ribs.

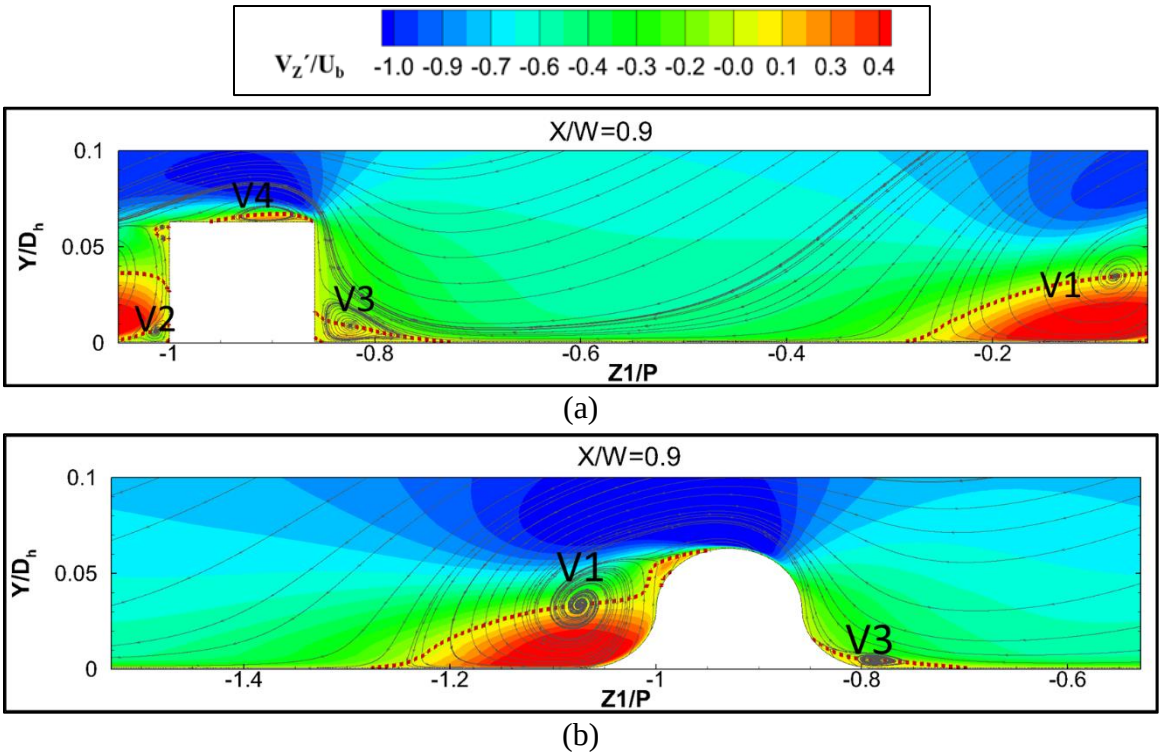

Figure 58 Non-dimensional V_Z' contour plots near the ribs for (a) Sharp ribs (b) Round ribs at the plane $X/W = 0.9$

In the previous chapter, a detail discussion has been done for the characteristics of the secondary flow created by the sharp ribs in one ribbed wall case. The characteristics of the secondary flow in the two ribbed wall case with the sharp ribs is very similar to the one in the one ribbed wall case. The flow experiences an acceleration on top of the ribs due to the reduction of the cross–sectional area caused by the ribs. Then, the flow encounters a sudden expansion behind the ribs. Consequently, the flow separation occurs and a wide recirculation zone V1 behind the ribs is observed. The vortex V1 is clearly seen in both sharp and round cases in Figure 58 and Figure 59. For sharp case, the vortex V1 is found to be accompanied with another small counter-rotating vortex V2 at the lower corner behind the ribs. There is another flow separation region V3 in front of the next rib. Later the flow hits the next rib, the flow deflects and another separation happens

and a small vortex V4 forms on top of the ribs. The flow does not separate on top of the ribs for the round case as the round ribs are streamlined. Hence the vortex V4 is not observed in this case. The vortex V2 and V3 are also not prominent for the round ribs due to the same reason.

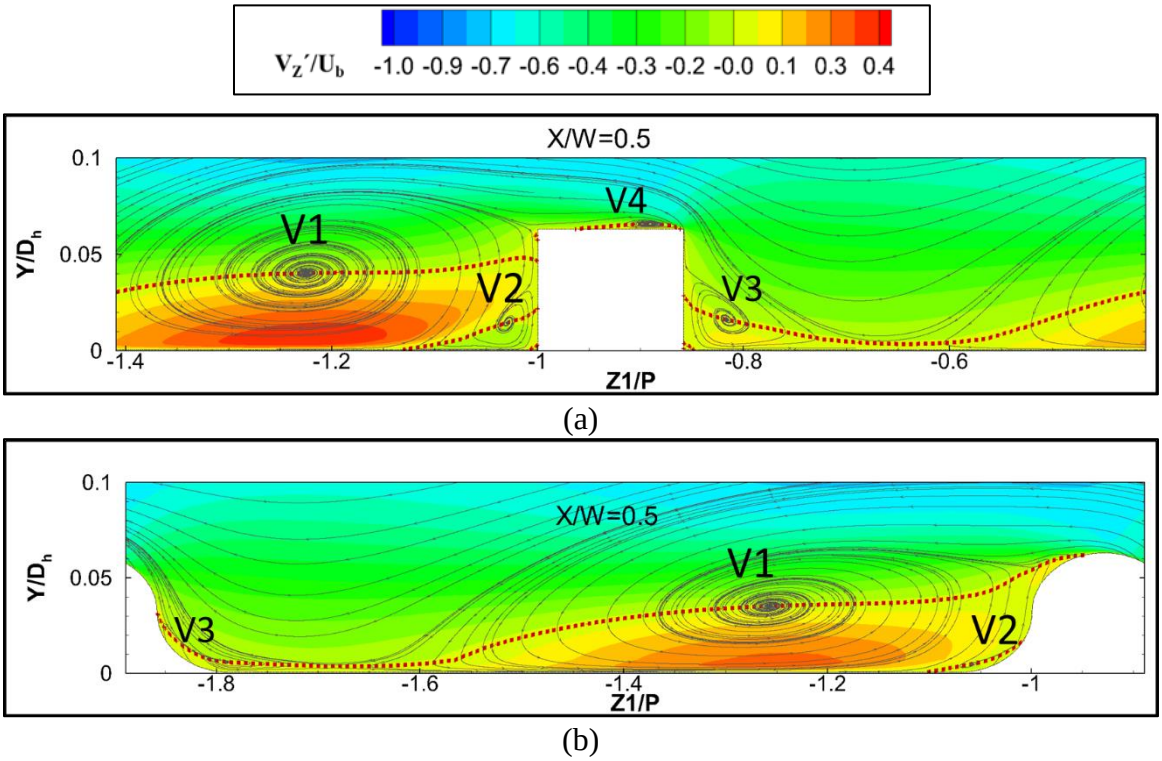

Figure 59 Non-dimensional $V_Z{}'$ contour plots near the ribs for (a) Sharp ribs (b) Round ribs at the plane $X/W = 0.5$

The contour plots of non-dimensional V_Z' at the different streamwise planes ($\frac{X}{W}$ = 0.9-0.2) for the sharp and round ribs are shown in Figure 60 and Figure 61, respectively. The secondary flow vortices are strongly guided by the rib's inclination. For both the sharp and round cases, the inception of the vortex V1 occurs at the intersection of the downstream face of the rib and upstream side wall and swirls diagonally toward the downstream side wall. As the vortex V1 moves toward

the downstream side wall, the vortex center moves away from the ribs, causing larger vortex size. The isolines $V_Z^{'}$ = 0 (black solid line) show the extent of the vortices. Simultaneously, the other vortices, V2 and V3 also grow as those advances toward the downstream side wall in the sharp ribs case. However, a slight growth of the vortex V2 and V3 is also detectable for the round ribs. Eventually, the secondary flow reaches the downstream side wall and the streamlines impinge on the downstream wall and merge with the main flow.

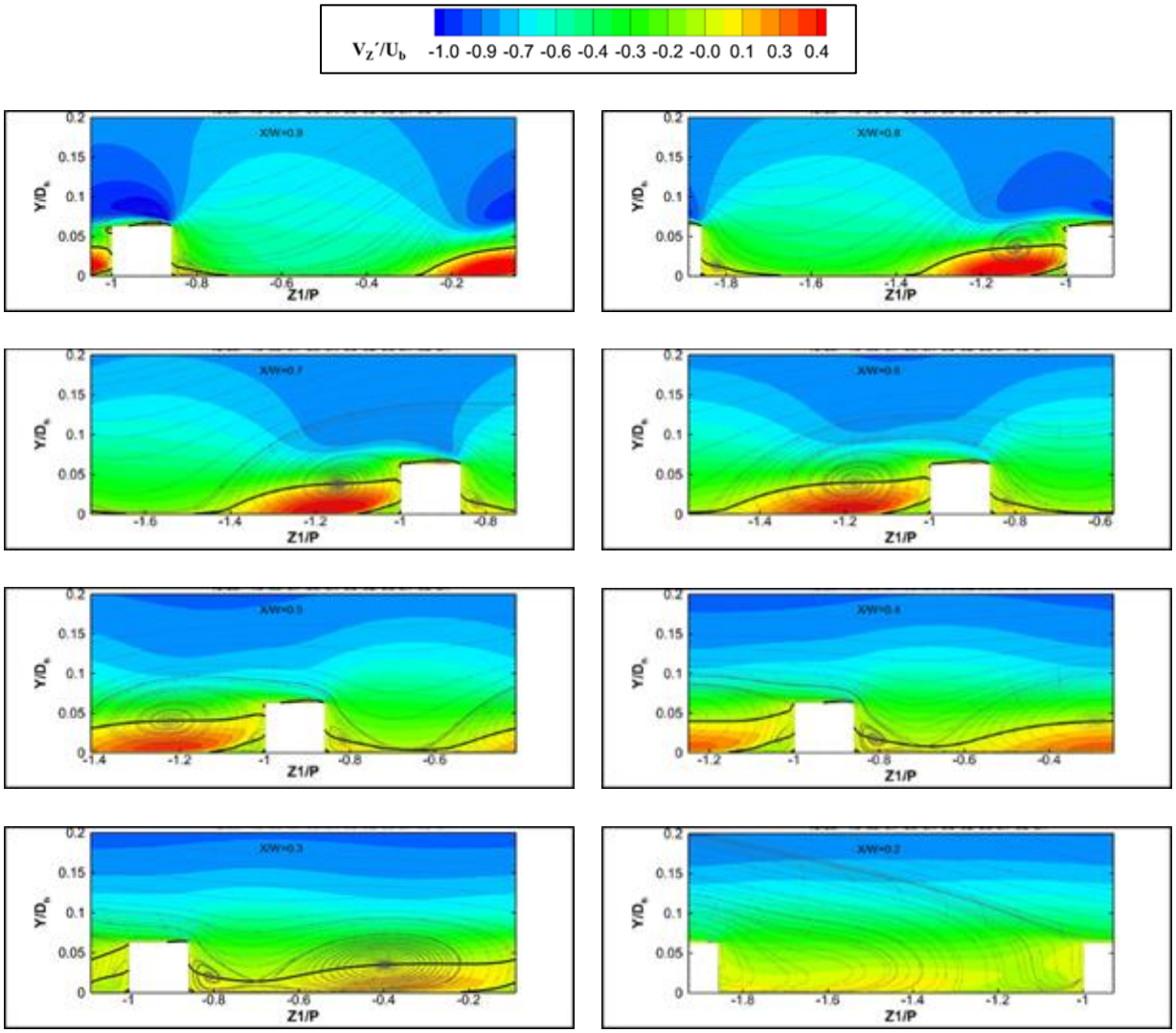

Figure 60 Non-dimensional $V_Z^{'}$ contour plots at different streamwise planes for sharp ribs

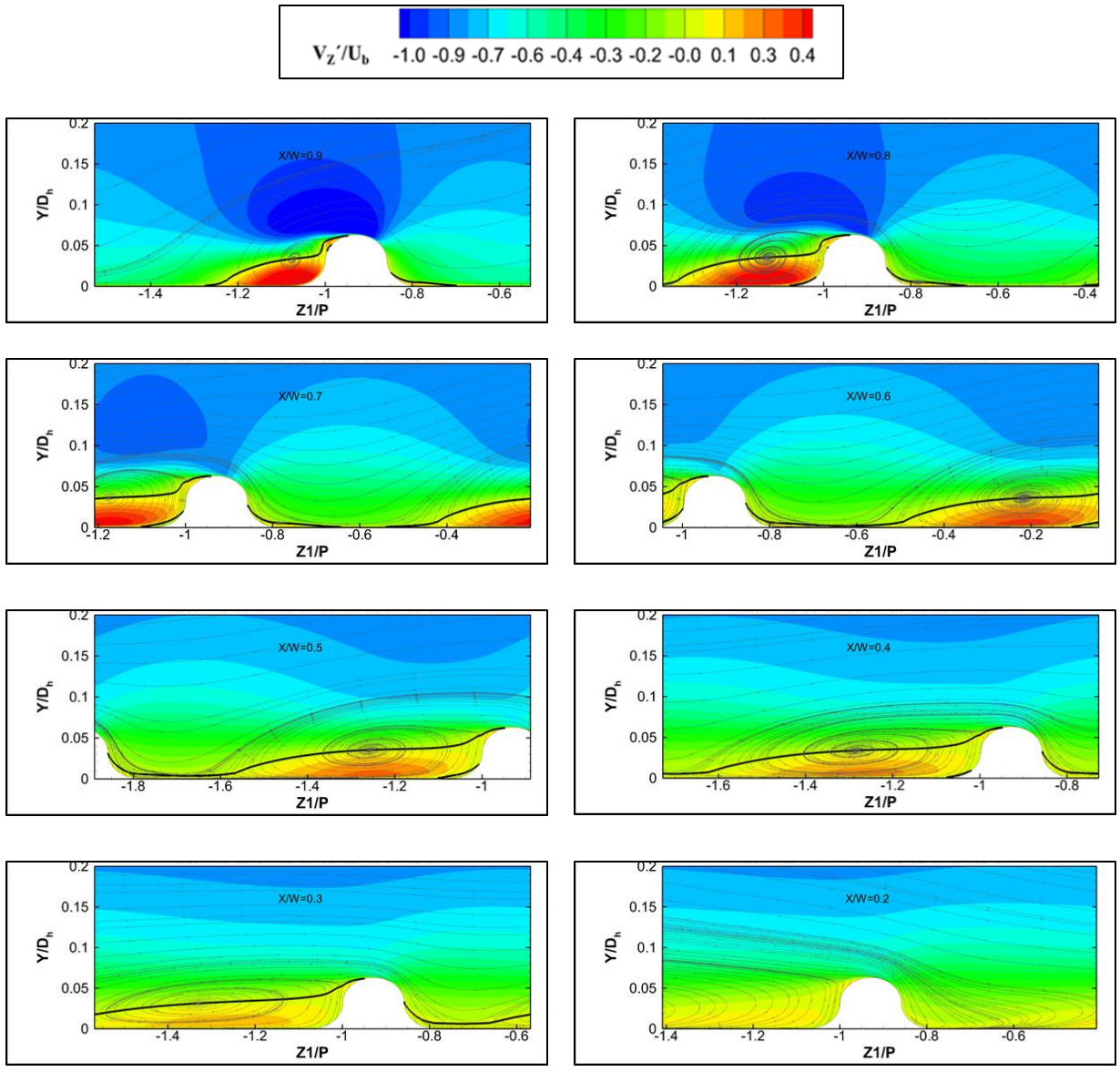

Figure 61 Non-dimensional $V_Z^{'}$ contour plots at different streamwise planes for round ribs

Figure 58 and Figure 59 show the close view of the recirculation zone in the planes, $\frac{X}{W}$ = 0.9 and $\frac{X}{W}$ = 0.5, respectively. An isoline $V_Z^{'}$ = 0 (red, broken line) is used to detect the extent of the vortices. In the plane $\frac{X}{W}$ = 0.9, the recirculation zone V1 is observed to reattach at $\left|\frac{Z1}{P}\right|$ ~ 0.29 (= 1.29 since

the flow is periodically fully developed) for both the sharp and round ribs. However, the recirculation zone V1 is seen not to reattach in the plane $\frac{X}{W}$ = 0.5 for both the cases. Instead, a saddle point observed between the vortex V1 and V3 at this plane. For both the cases, the recirculation vortex V1 shows a reattachment for $\frac{X}{W}$ = 0.9-0.7 planes. The rest of the planes do not show reattachment of vortex V1. Rather, the vortex V1 starts to lift off from the wall $\frac{X}{W} \leq$ 0.6. Figure 62 displays the comparative size of the vortex V1 at different streamwise planes ($\frac{X}{W}$ = 0.9-0.3) between the sharp and round ribs. The vortices start to dissipate at $\frac{X}{W}$ = 0.2. It is clearly observed that the vortex V1 grows continuously larger as it travels toward the downstream lateral wall. Another observation is that the round ribs cause a slight larger vortex V1 than the sharp ribs at the planes $\frac{X}{W}$ = 0.8-0.3.

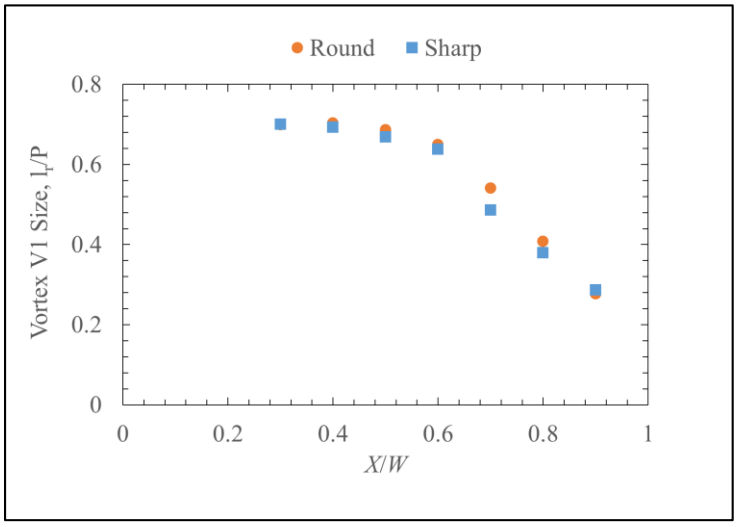

Figure 62 Comparative results of the size vortex V1 between sharp and round ribs

Figure 63 shows the contour of the Q criterion at the plane $\frac{X}{W} = 0.8$ for both the sharp and round ribs. The sharp ribs show high positive Q criterion at the locations for vortices V1, V2, V3, and V4. The round ribs case has a high positive value of Q at the core of the vortex V1 only. This also verifies the absence (or very weak) of other vortices in the round ribs case.

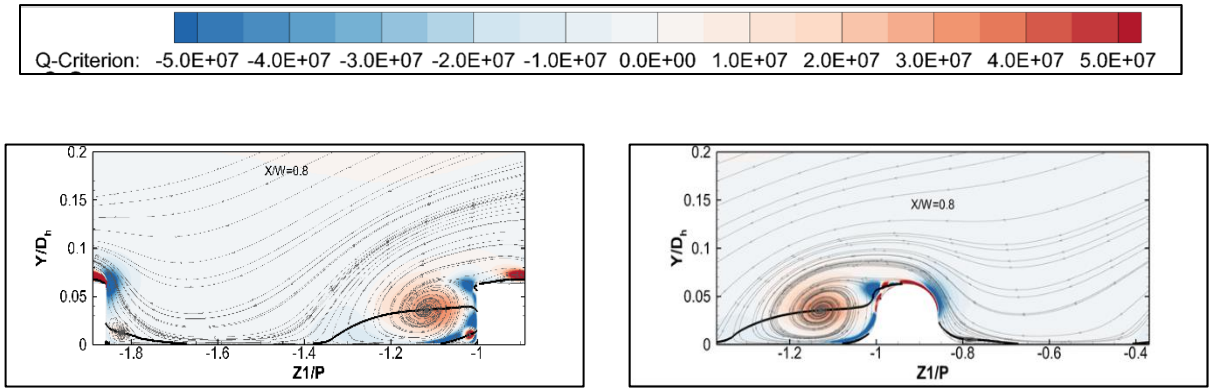

Sharp ribs Round ribs

Figure 63 Q criterion at the streamwise plane, $X/W = 0.8$

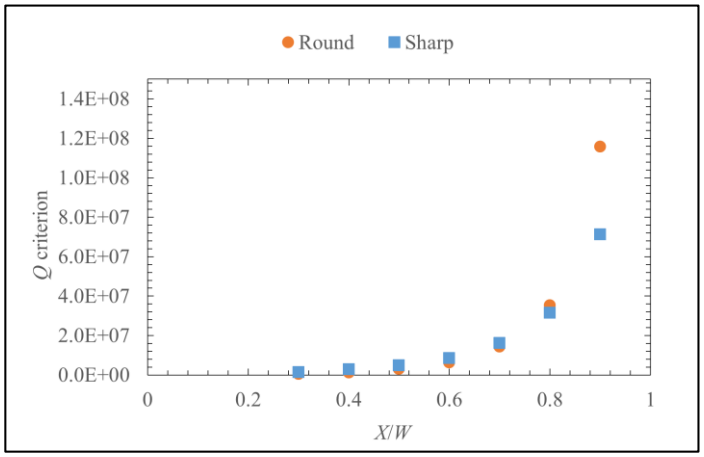

Figure 64 Q criterion at the vortex center V1 at different streamwise planes

The value of the *Q* criterion at the vortex V1 core at the different streamwise planes for both the sharp and round cases are shown in Figure 64. It depicts that the vortex V1 lose strength (indicated by *Q* criterion) as it travels toward the downstream lateral wall. The round ribs show the higher value of *Q* near the vortex inception location at $\frac{X}{W}$ = 0.9; afterward, the vortex V1 loses its strength faster for the round ribs than the sharp ribs and both types of ribs show the similar value of *Q* at the other planes.

Figure 65 displays the contour plots of non-dimensional turbulent kinetic energy for both sharp and round ribs at the streamwise midplane. Both ribs generate strong separated shear layer behind the ribs which starts from the leading edge of the ribs and spread up to ~ $\left|\frac{Z1}{P}\right|$ < 1.5. The sharp ribs have a stronger separated shear layer (TKE ~ 8% of U_b^2) than the round ribs on the top of the ribs due to the vortex V4 formation on it. Even behind the ribs, the round case possesses lower TKE (~ 5% of U_b^2) in the shear layer than the sharp ones.

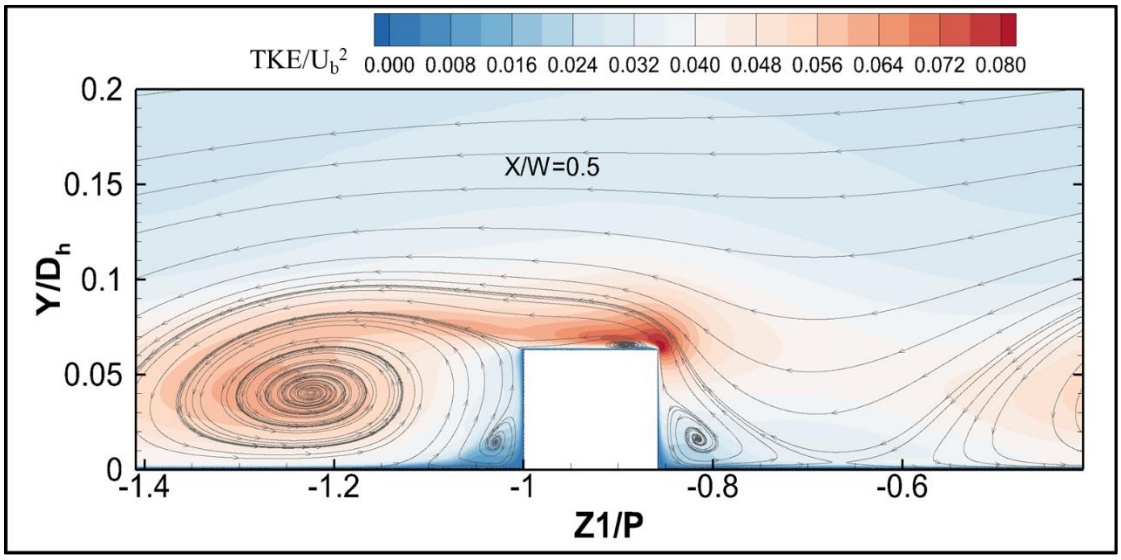

Sharp ribs

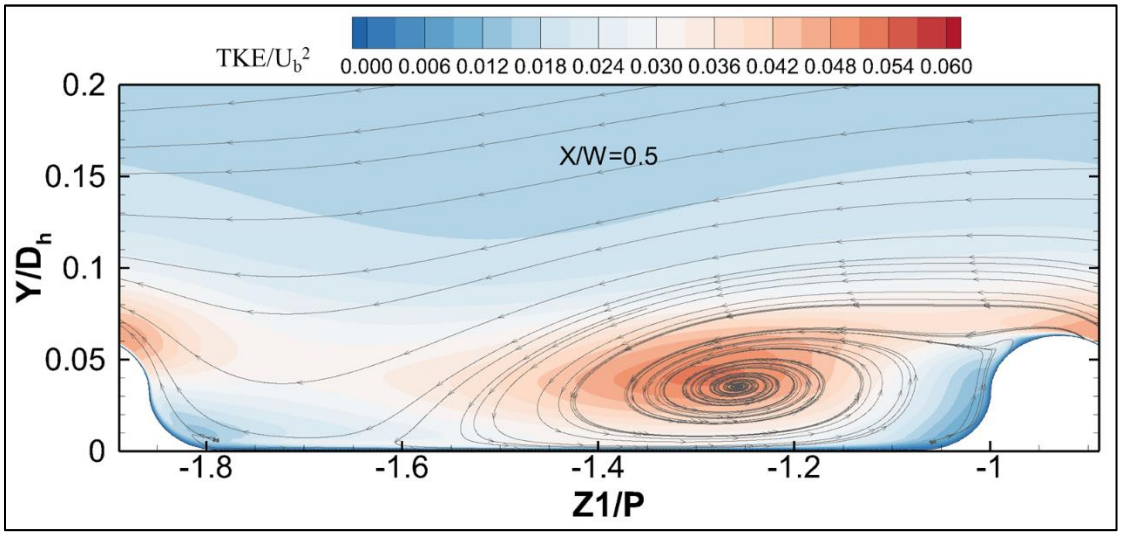

Round ribs

Figure 65 Non-dimensional turbulent kinetic energy contour plots at the streamwise midplane

Heat Transfer Behavior Analysis

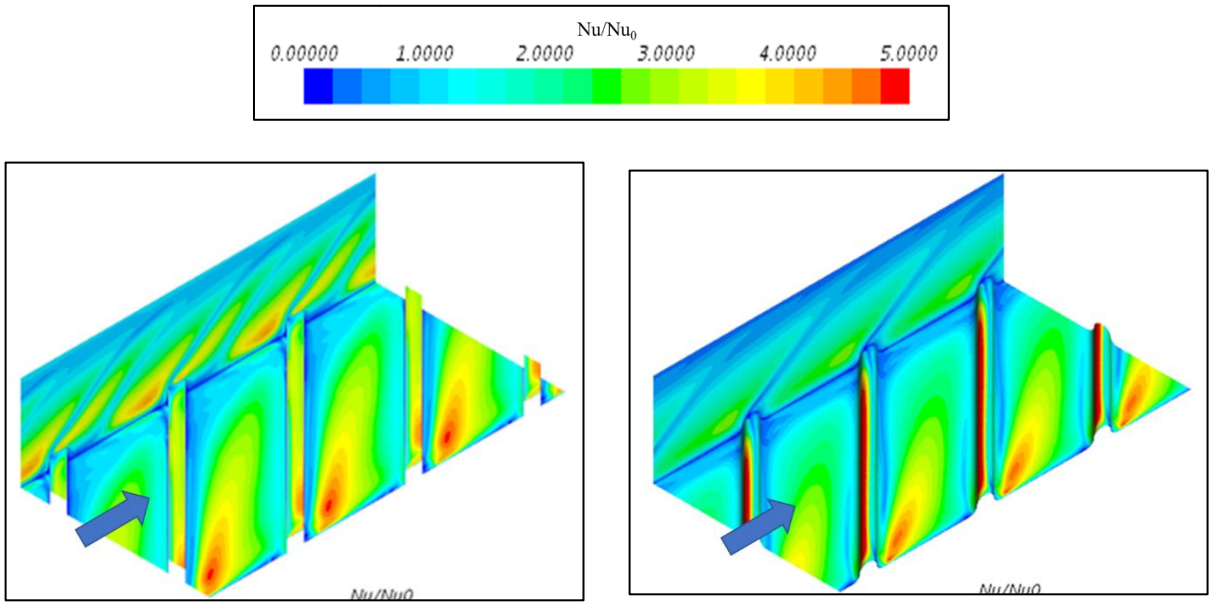

(a) Sharp ribs (b) Round Ribs

Figure 66 Periodically transformed local Nu/Nu_0 contour plots at Re ≈ 52,000

The contour plots of local heat transfer augmentation for sharp and round ribs are shown in Figure 66. As mentioned earlier, the computational domain for numerical studies were consists of one pitch only. For a better comprehension, the results are periodically transformed for two more ribs and presented in Figure 66. The Nu_0 for smooth channel calculated by using Dittus Boelter equation is used for normalization.

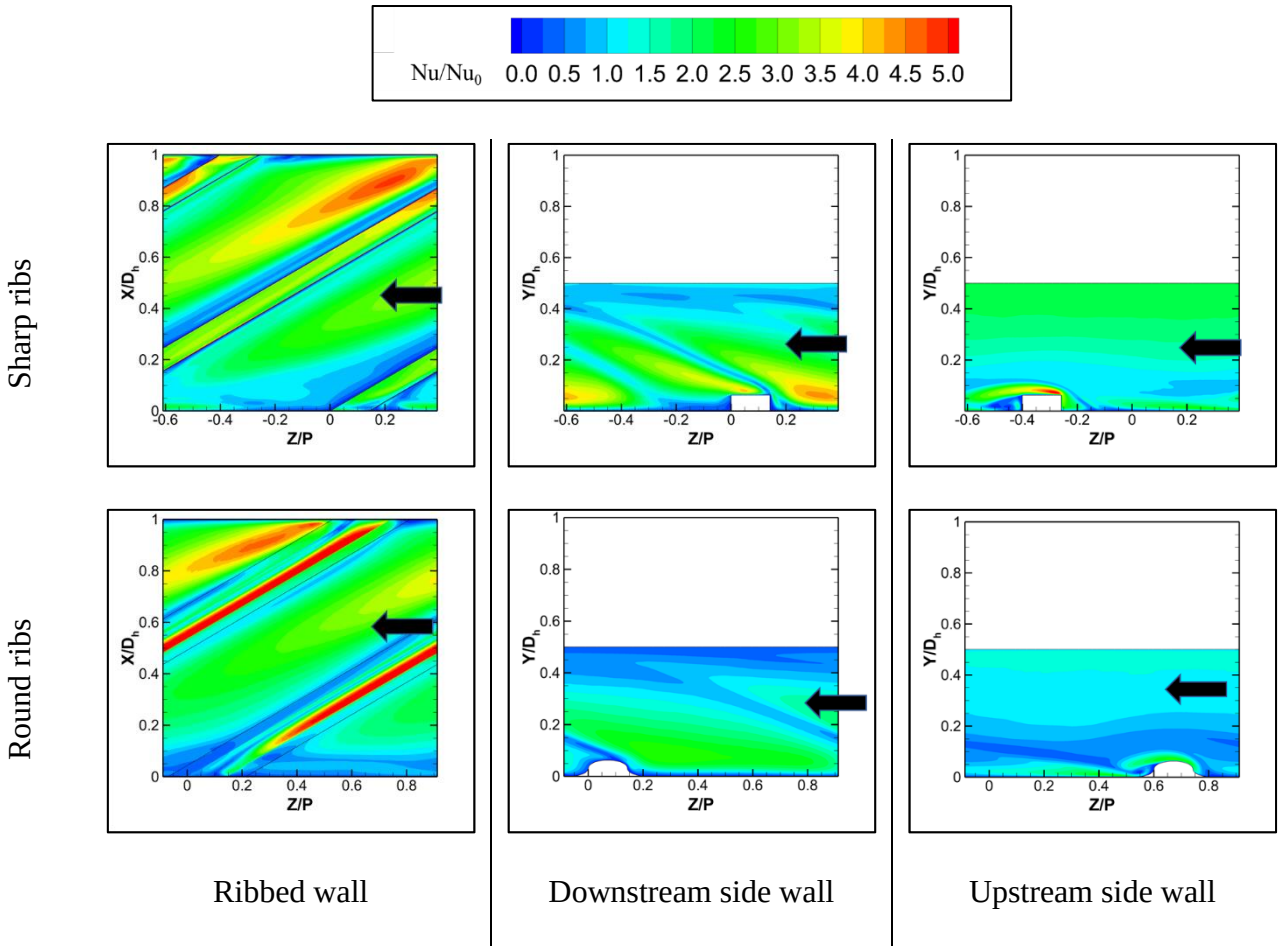

Figure 67 Local Nu/Nu_0 contour plots at Re ≈ 52,000

Figure 67 shows the contour plots of local Nu augmentation, $\frac{Nu}{Nu_0}$ for the ribbed and the side walls of both sharp and round ribs. For both cases, the basic characteristics of the $\frac{Nu}{Nu_0}$ distribution are very similar to the one ribbed wall case described in the previous chapter. The local heat transfer is found to be highly non-homogenous and influenced by the secondary flow induced by the ribs. There is a high heat transfer zone is noticed on the ribbed wall near the upstream side wall corner in the inter-rib space. This high heat transfer zone is caused due to the inception of the rib induced recirculating vortex V1 which improves mixing of the hotter fluid near the wall with the colder

fluid at the core. As mentioned earlier, the reattachment of vortex V1 occurs at $\frac{X}{W} \geq 0.7$ and shows the highest heat transfer augmentation in this zone. Afterward, the secondary vortex V1 does not reattach and cannot sweep away the heat from the wall effectively and reduces the heat transfer. The maximum Nu augmentation value in the inter-rib space is higher for sharp ribs ($\frac{Nu}{Nu_0} \sim 4.8$) than the round ribs ($\frac{Nu}{Nu_0} \sim 4.6$). It is clearly observed that this high heat transfer zone diverts away from the rib diagonally in the direction of the downstream side wall. The progressive contact between flow and wall while the secondary flow moves toward the downstream side wall causes the convective heat transfer less effective. This results in a reduction in the Nu augmentation value in this area toward the downstream side wall. There is a narrow portion of lower $\frac{Nu}{Nu_0}$ just behind the ribs due to the almost stagnant flow caused by the vortex V2. This lower heat transfer zone associated with V2 is more prominent in sharp ribs than the round ribs (especially up to $\frac{X}{W} = 0.6$) since the vortex V2 is very small for the latter case.

For the sharp ribs, the highest heat transfer augmentation ($\frac{Nu}{Nu_0} \sim 5.0$) occurs at the upper portion of the rib's front surface because of the shear layer impingement. The front face of the round ribs also possesses its highest heat transfer augmentation ($\frac{Nu}{Nu_0} \sim 4.9$) due to the high local acceleration of the flow on the round ribs. These high heat transfer augmentation zones can be seen clearly in Figure 68. The top face of the sharp ribs also shows higher heat transfer due to the presence of the stronger shear layer caused by the vortex V4. The maximum heat transfer augmentation ($\frac{Nu}{Nu_0} \sim 4.5$) on the top surface of the ribs is observed near the corner of the rib and the upstream lateral wall.

Since the round ribs are streamlined, no such high heat transfer zone is associated with the round ribs.

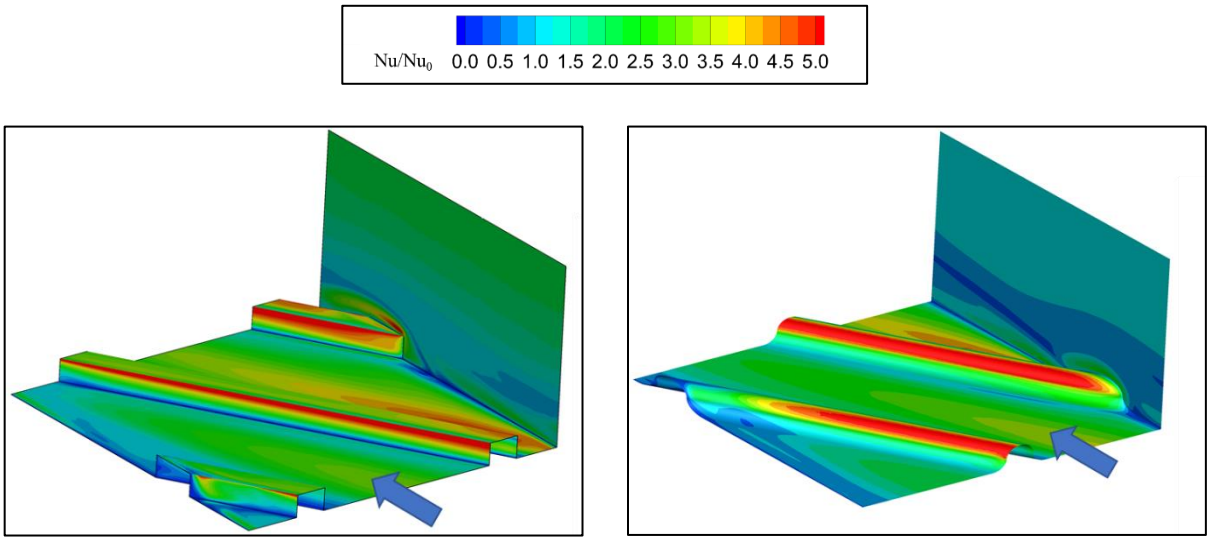

Figure 68 Local Nu/Nu_0 contour plots for ribbed and upstream side wall at Re ≈ 52,000

Table 18 Average heat transfer augmentation for sharp and round ribs at Re ≈ 52,000

	Average $\frac{Nu}{Nu_0}$	
	Ribs	Inter-rib space
Sharp ribs	2.58	2.10
Round ribs	2.23	2.09

The surface average of local heat transfer augmentation results of the ribs and the inter-rib space is tabulated in Table 18 for both types of the ribs. It shows that the average Nu augmentation in the inter-rib space is very similar for both cases. As discussed earlier, both types of the ribs cause

secondary vortex V1 of similar size and strength (Q criterion). This results in very similar average heat transfer augmentation in the inter-rib space. It also implies that the vortex V1 primarily dominates the local heat transfer distribution. The other smaller vortices have a minor influence on the local heat transfer augmentation distribution on the ribbed wall.

On the downstream side wall, there is an elongated high heat transfer area exists above and behind the ribs. The impingement of the streamlines of the main and secondary flow causes this high heat transfer area. The sharp ribs show higher heat transfer augmentation in this area (max $\frac{Nu}{Nu_0}$ ~ 4.2) than the round ribs (max $\frac{Nu}{Nu_0}$ ~ 2.7) due to the stronger impingement of the flow caused by the sharp ribs. For better comprehension, the contour plots of the non-dimensional $V_X^{'}$ at a streamwise plane $\frac{X}{W}$ = 0.02 (~ 1mm away from the downstream side wall) have been shown in Figure 69. The velocity $V_X^{'}$ implies the impingement velocity of the flow on the wall. Note that the negative value of $V_X^{'}$ denotes the flow toward the downstream side wall. It is clearly noticed that the Nu augmentation distribution on the downstream side wall is the direct manifestation of the flow impingement velocity. The sharp case causes higher impingement velocity than the round one which aids in higher heat transfer. A positive $V_X^{'}$ zone is observed at the bottom of the plane. This is caused by the downwash from the flow impingement on the wall, which causes a low heat transfer zone. This reverse flow zone is found to be wider for the sharp ribs than the round one. The Nu augmentation on the upstream side wall is noticeably lower than the downstream side wall. On the upstream side wall, a thin area of high $\frac{Nu}{Nu_0}$ is observed near the ribs for both cases. This

corresponds to the start of the secondary vortex formation behind the rib (V1). Overall, the round ribs cause much lower heat transfer augmentation on this wall than the sharp ribs.

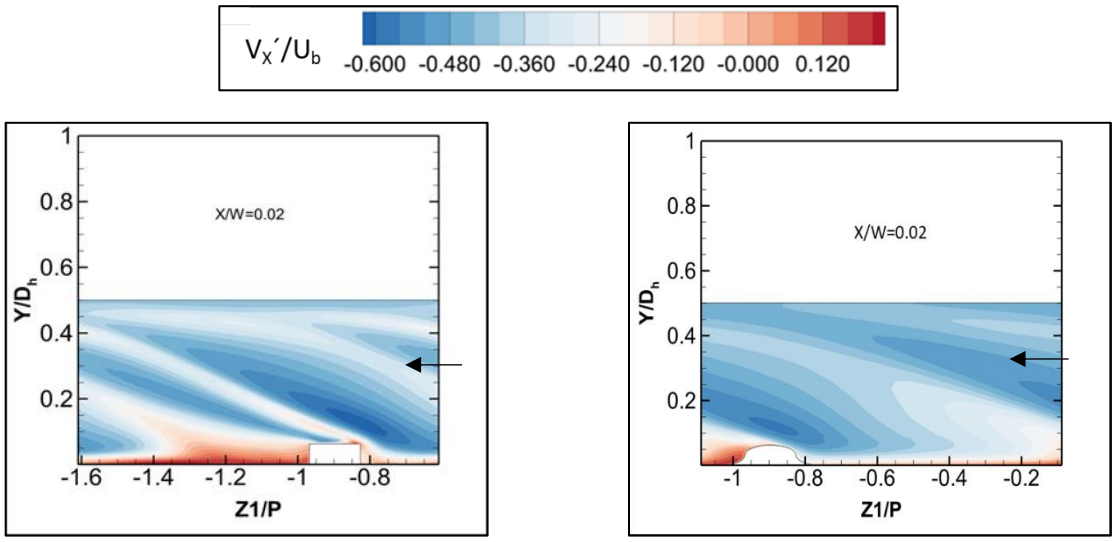

Figure 69 Non-dimensional $V_X{}'$ contour plot at the streamwise plane at X/W = 0.02

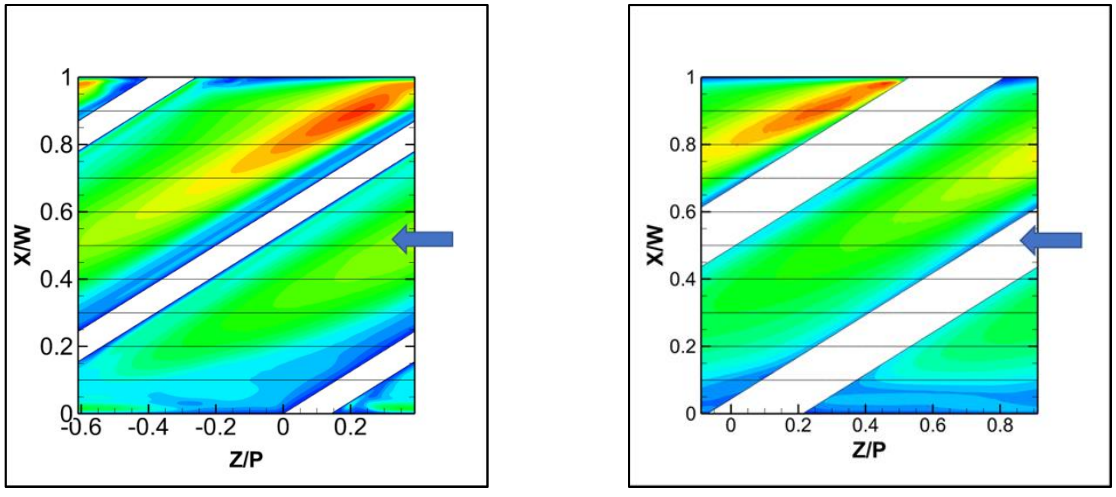

Sharp ribs Round ribs

Figure 70 Location for the polylines

Nu augmentation results on nine different streamwise polylines ($\frac{X}{W}$ = 0.9-0.1) on the ribbed wall were extracted as shown in Figure 70 for both sharp and round ribs. Note that, the $\frac{Nu}{Nu_0}$ data were

extracted only from the inter-rib space and the results are presented in Figure 71 and Figure 72. In these figures, the local coordinate $Z1$ = -1 starts from the downstream point of the ribs for each plane. A peak in heat transfer augmentation is observed, especially at the planes $\frac{X}{W} \geq 0.7$ for both the cases. The value of the peak $\frac{Nu}{Nu_0}$ decreases as the flow travel toward the downstream side wall.

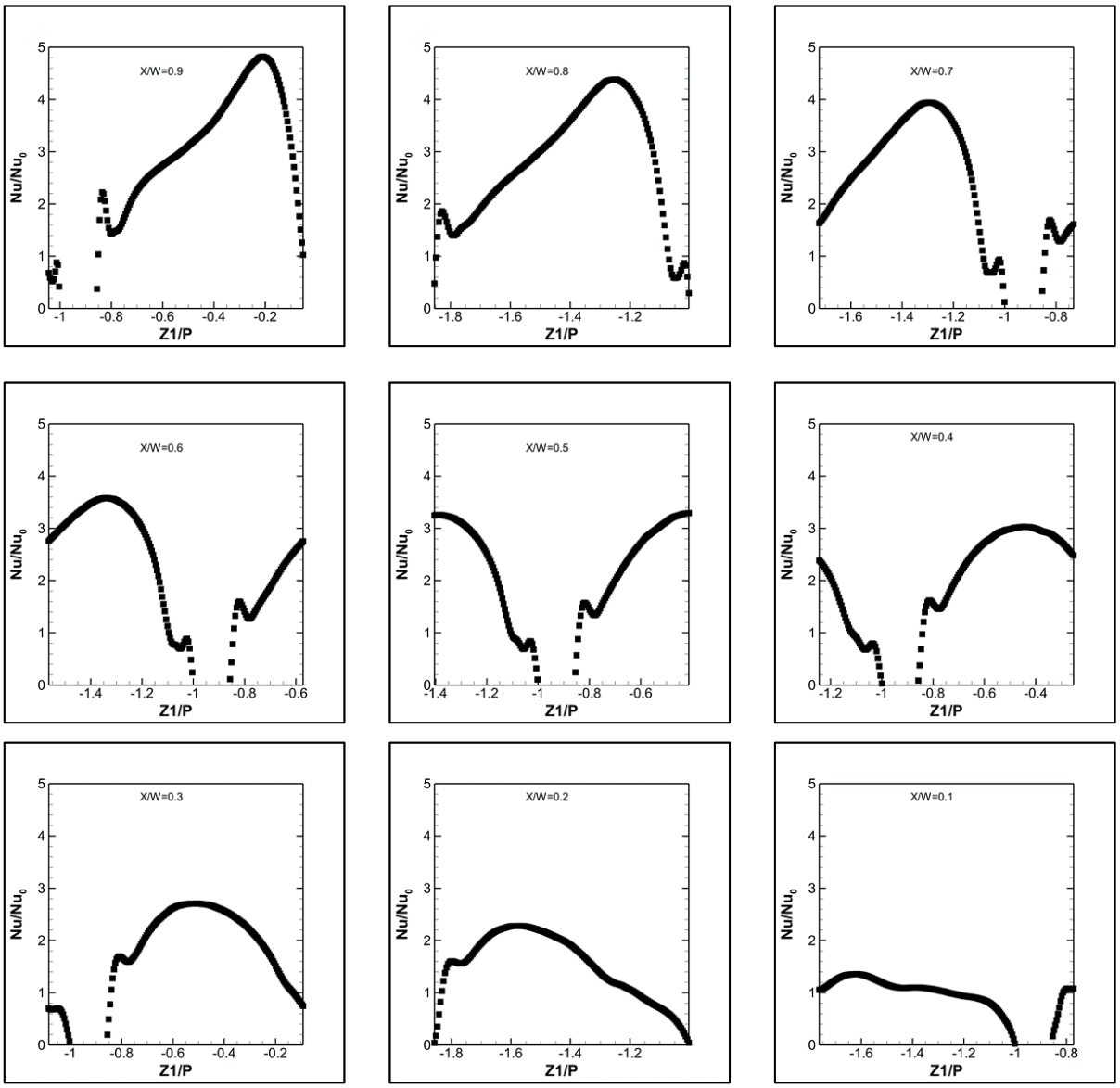

Figure 71 Local Nu augmentation along the streamwise polylines for sharp ribs

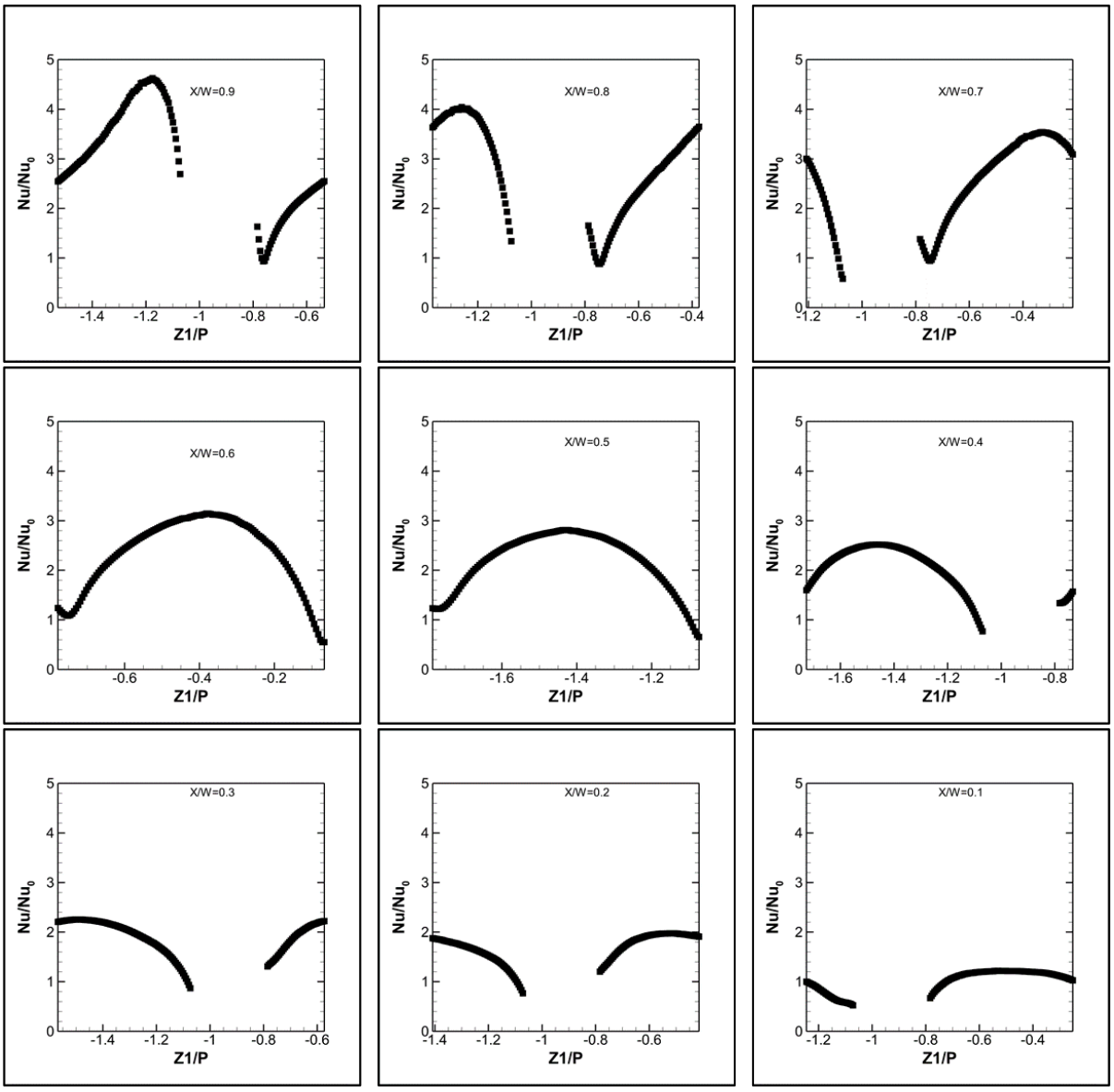

Figure 72 Local Nu augmentation along the streamwise polylines for round ribs

Recall that the main flow goes in -*Z*1 direction in the Figure 71 and Figure 72. Figure 73 (a) presents the average $\frac{Nu}{Nu_0}$ along the extracted polylines for both sharp and round ribs. Both sharp and round ribs show very similar results for the average heat transfer augmentation. Therefore, the average $\frac{Nu}{Nu_0}$ in the inter-rib space is very similar for both sharp and round cases which are also

shown in Table 18. However, the average heat transfer augmentation for the ribs is higher (~ 13.5%) for the sharp ribs than the round ribs which results in the overall higher heat transfer augmentation on the ribbed wall for the sharp ribs than the round ones.

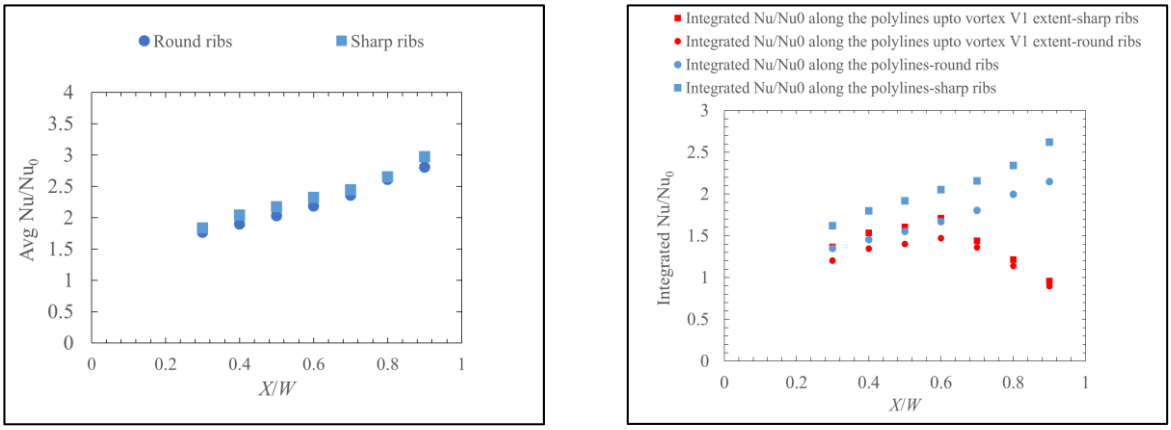

(a) (b)

Figure 73 Comparative results of (a) Average Nu/Nu_0 along the polylines (b) Integrated Nu/Nu_0 between the sharp and round ribs

Figure 73 (b) presents the comparative results of integrated $\frac{Nu}{Nu_0}$ along the streamwise polylines for both sharp and round ribs. Integrated $\frac{Nu}{Nu_0}$ denotes the total heat transfer augmentation along the polylines. Similarly, integrated $\frac{Nu}{Nu_0}$ up to the V1 extent indicates the contribution of vortex V1 to the total heat transfer augmentation along the polyline. The results are calculated for $\frac{X}{W}$ = 0.9 to 0.3 as the vortex V1 starts to dissipate at $\frac{X}{W}$ = 0.2. It is found that the integrated $\frac{Nu}{Nu_0}$ along the polylines decreases as the flow travel toward the downstream side wall. The integrated $\frac{Nu}{Nu_0}$ along the polylines and the vortex V1 extent shows a higher value for the sharp ribs than the round ribs.

However, the polylines were extracted from the inter-rib space only. For the round ribs, the inter-rib space, as well as the polylines are smaller due to the presence of rib fillet. Therefore, the average $\frac{Nu}{Nu_0}$ shows similar values for both the sharp and the round case. As mentioned earlier, the vortex V1 becomes larger while it travels from the upstream side to the downstream side wall. Consequently, the integrated $\frac{Nu}{Nu_0}$ up to the vortex extent continuously increases from $\frac{X}{W}$ = 0.9 to 0.6. Afterward, the integrated $\frac{Nu}{Nu_0}$ up to the vortex again decreases as the vortex V1 lifts off and loses its strength (low *Q* criterion) $\frac{X}{W} \leq 0.6$. Figure 74 shows the contribution of vortex V1 on the total heat transfer. It is observed that the contribution of vortex V1 is more for round ribs than the sharp ribs.

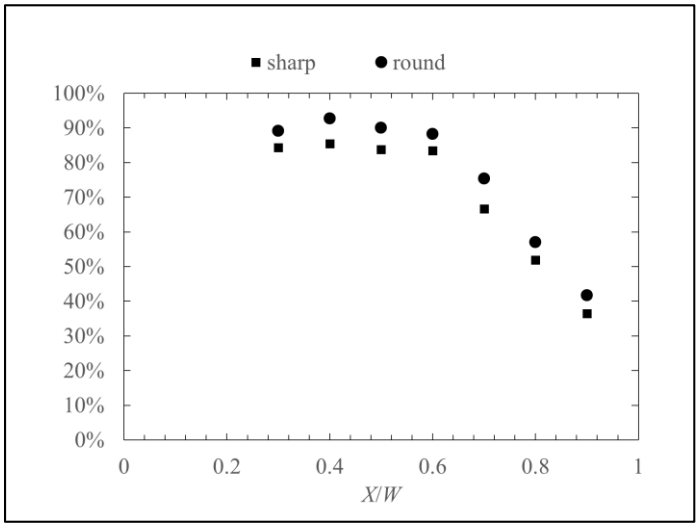

Figure 74 Contribution of vortex V1 on the total heat transfer

CHAPTER 9: CONCLUSION AND FUTURE WORK

Heat Transfer and Pressure Drop of Sharp and Round Ribs

Comprehensive comparative studies have been conducted between sharp and round ribs in a wide range of Re (6,000-135,000) by both experimental and numerical methods. Experimental results show that rounding the ribs' edges causes lower heat transfer than the corresponding sharp ribs for all the Re. The round ribs do not only reduce heat transfer on the ribbed wall but reduce the heat transfer on the adjacent side walls as well. At the lowest tested Re (~ 6,000), round ribs and sharp ribs possess similar heat transfer. Beyond that, the round ribs result in lower heat transfer than sharp ribs with the increasing Re (e.g., at Re ≈ 135,000, round ribs cause ~ 23% lower channel average heat transfer). The comparative friction results between sharp and round ribs show that rounding the rib corners does not reduce the friction appreciably for the tested blockage ratio. This contrasts with the findings with high blockage ratio round ribs, where high reduction of friction was reported [12, 7]. However, the current geometry shows that rounding the ribs edges causes only a 6% - 9% reduction in friction factor.

Comparative RANS results show that prediction capability of different turbulence model varies with the type of the ribs as well as the flow Reynolds numbers. RKE predicts the measured heat transfer data for both sharp and round ribs well with a maximum deviation ~ 6% (at Re ≥ 50,000). Similarly, SST k-ω also shows very good agreement for the sharp ribs' measured data (maximum deviation ~ 4%). However, this model underpredicts the round ribs' results by ~ 9% - 13%. On the contrary, the v^2-f turbulence model hugely overpredicts the heat transfer results for sharp ribs by

10% - 17%; however, it shows only 5% - 7% deviation from the experimental average Nu of round ribs.

All the turbulence models overpredict the friction for both types of ribs. Among them, RKE and SST k-ω show a reasonable prediction for the experimental friction data at higher Re (> 50,000). The experimental and CFD results show that thermal performance gradually decreases with the Re in both cases. The trend of the experimental curve indicates that the thermal performance of the sharp ribs becomes lower than unity at Re ≈ 180,000. On the other hand, thermal performance of the round ribs case falls below unity at much lower Re (Re ≥ 90,000).

Aerothermal Behavior Analysis with Sharp Ribs (One Ribbed Wall Case)

The detailed flow behavior in a square channel with 45° ribs was studied using both experimental and numerical methods. The ribs were applied to one of the walls of the channel. A detail benchmarking flow field data at the streamwise midplane in a 45° ribbed channel was acquired using stereo PIV technique. The measurements were conducted at a fully developed flow region for multiple Re in the range of Re = 10,000-150,000. Numerical studies were performed using LES as well as different RANS models at Re ≈ 30k. A detailed comparison has been conducted between the experimental data, LES and different RANS models.

The mean velocity and turbulence statistics results show excellent agreement between the experimental data and the LES. The rib induced recirculation zone is not visible in the mean streamwise velocity contour plot. It is found that the X-Z coordinate system is not a proper

representative coordinate system to capture the recirculating structure for the tested channel. To capture the recirculating secondary flow structure, a new coordinate system $X^{'} - Z^{'}$ was created. The direction of $X^{'}$ and $Z^{'}$ is parallel and normal to the ribs, respectively. The contour plots of mean velocity in $Z^{'}$ direction clearly shows a recirculation vortex V1 behind the ribs. This vortex is accompanied with another small counter-rotating vortex V2 at the lower corner behind the ribs. There are two more vortices V3 and V4 captured. The vortex V3 forms just in front ribs, and the vortex V4 forms on top of the ribs. The inception of the vortices happens in the corner of the upstream side wall with the trailing edge of the ribs. Then the vortices travel toward the downstream side wall diagonally following a spiral path. As the vortex swirls, the center of the vortex V1 moves away from the ribs, causing a larger vortex size. The other vortices also grow as they travel toward the downstream side wall. Moreover, the vortices lose their strength (indicated by *Q* criterion) as they approach the downstream lateral wall. Among the RANS models, RKE and v^2-f show good prediction of the mean velocity results, as well as the characteristics of the rib induced vortices. However, SST k-ω model shows some non-physical behavior for the rib induced vortices, specially at the streamwise midplane.

A strong shear layer behind the ribs is clearly observed both in the experiment, LES as well as RANS. A shear layer generates as the flow separation occurs from the rib's upper surface. The shear layer covers almost the full inter-rib space in the streamwise midplane. The maximum strength of the shear layer exists from the leading edge of the ribs to the middle of the rib pitch ($\left|\frac{Z1}{P}\right| < 1.45$). All the RANS models underpredict the strength of the separated shear layer. The v^2-f model shows the reasonably good prediction of the shear layer both qualitatively and

quantitatively. The results of the Reynolds stresses show that the flow is highly anisotropic near the ribs.

The LES results show excellent compliance with the experimental average heat transfer and friction data. The v^2-f turbulence model also matches the experimental results very well. An attempt is made to correlate the local $\frac{Nu}{Nu_0}$ with the flow behavior of the channel. It is observed that local heat transfer is highly non-homogenous and influenced by the secondary flow induced by ribs. The maximum heat transfer occurs near the top edge of the front wall of the ribs due to impingement of the shear layer. There is a high heat transfer zone in the inter-rib space which is associated with the vortex V1. There is a narrow portion behind the ribs with lower heat transfer associated with the almost stagnant flow caused by the vortex V2. There is also a slightly high heat transfer augmentation on the top surface and in front of the ribs associated with vortex V3 and V4. On the downstream side wall, there is an elongated high heat transfer area exists above and behind the ribs due to the impingement of the of the streamlines of the main and secondary flow. The $\frac{Nu}{Nu_0}$ on the upstream side wall is noticeably lower than the downstream side wall.

The stereo PIV results at different Re are analyzed to see the effect of increasing Re on the secondary flows. It is found that the rib induced vortex V1 shrinks toward the upstream rib's trailing edge, yielding in smaller vortex size, as the Re increases from Re = 10,000 to 70,000. The size and height of the vortex core remain invariant at Re ≥ 70,000. Re is also found to have a significant influence on the rib generated shear layer regarding size and the TKE value.

Aerothermal Behavior of Sharp and Round Ribs (Two Ribbed Wall Cases)

A detailed comparative study between the sharp and the round ribs (two ribbed walls) was conducted to see the effect of the round ribs on the aerodynamics as well as the heat transfer behavior. The v^2-f turbulence model was chosen for the investigation as it matched the experimental flow field data for the sharp ribs best among the RANS models. It is found that the characteristics of the secondary flow in the two ribbed wall case with the sharp ribs are very similar to the one in the one ribbed wall case. The rib induced vortex V1 is detected for both sharp and round ribs. The flow does not separate on top of the round ribs and hence the V4 is not observed in this case. As the round ribs are streamlined, the vortex V2 and V3 also do not form very prominently in this case. The round ribs cause a slight larger vortex V1 than the sharp ribs. Both ribs generate strong shear layer behind the ribs which starts from the leading edge of the ribs and spread up to the middle of the pitch. The sharp ribs have stronger shear layer than the round ribs on the top of the ribs due to the vortex V4 formation on it. Even behind the ribs, the round case has lower TKE in the shear layer than the sharp ones.

The distribution of the local heat transfer augmentation in the ribbed wall is found to have similar qualitative characteristics for both round and sharp ribs. Both cases show a high heat transfer zone in the inter-rib space which is associated with the vortex V1. For the sharp ribs, the highest heat transfer augmentation ($\frac{Nu}{Nu_0} \sim 5.0$) occurs at the upper portion of the rib's front surface because of the shear layer impingement. The front face of the round ribs also possesses its highest heat transfer augmentation ($\frac{Nu}{Nu_0} \sim 4.9$) due to the high local acceleration of the flow on the round ribs. The

average heat transfer augmentation in the inter-rib space is very similar for both sharp and round cases. However, the average heat transfer augmentation for the ribs is higher (~ 13.5%) for the sharp ribs which results in the overall higher heat transfer augmentation on the ribbed wall for the sharp ribs than the round ones.

Future Work

The current study with the lower blockage ratio ($\frac{e}{D_h}$ = 0.0625) finds that the rounding the ribs' edges cause a significant amount of lower heat transfer than the corresponding sharp ribs, especially at the higher Re. However, the round ribs do not reduce the friction appreciably. This contrasts with the findings with high blockage ratio round ribs [12, 7]. They reported that rounding the edges of the ribs do not have a significant effect on the heat transfer coefficient. However, the round ribs caused much lower pressure drop compared with the sharp ribs, especially with the taller ribs. To understand the effect of the blockage ratio on the round ribs, the author proposes an investigation on the comparative aerodynamical as well as the thermal behavior of the round ribs at the low and high blockage ratio. Both CFD and experimental approaches can be applied for the investigation.

The present study investigates the aerothermal behavior of the round ribs using the v^2-f turbulence model as it agrees best to the LES and experimental results. To achieve higher accuracy, the author proposes applying LES for the aerothermal investigation for the rounded edged ribs.

In the manual of the DaVis software, the detail guidelines for the stereoscopic PIV measurement is provided. For stereo PIV setup, a symmetrical camera arrangement is recommended to ensure higher accuracy in vector calculation. The optimal camera angle for stereo PIV ($\alpha 1 = \alpha 2$) is around 30°-35°. However, in the current study, a highly asymmetric camera arrangement was required to measure the flow field in the inter-rib space where $\alpha 1 = 55°$ and $\alpha 2 = 90°$ as shown in Figure 75. This extreme camera angle may result in a bias uncertainty in the stereo PIV measurement. The DaVis software provides the random or statistical uncertainties of the vector components V_Z, V_Y, V_X based on the Wienke's correlation statistics method [75, 76, 77]. The random or statistical uncertainties are caused due to the particle image size, seeding density, displacements, and shear, etc. However, this does not consider the probable bias uncertainties caused by the extreme camera angle which can have a considerable contribution to the error in the measurement. The author recommends DaVis software to incorporate the bias uncertainties due to the camera angle in the uncertainty calculation for stereo PIV.

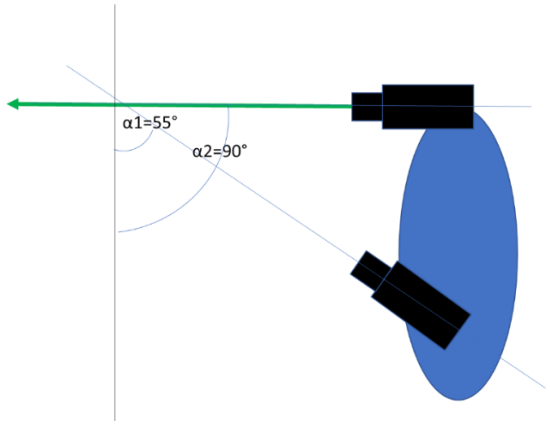

Figure 75 Asymmetric camera arrangement for the current study

APPENDIX A: EXPERIMENTAL UNCERTAINTY TREES

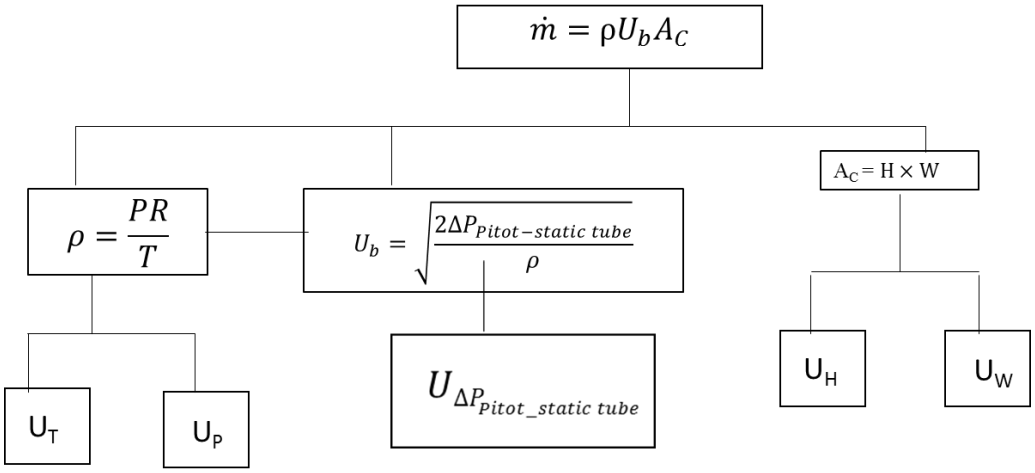

Figure 76 Uncertainty tree for mass flow rate

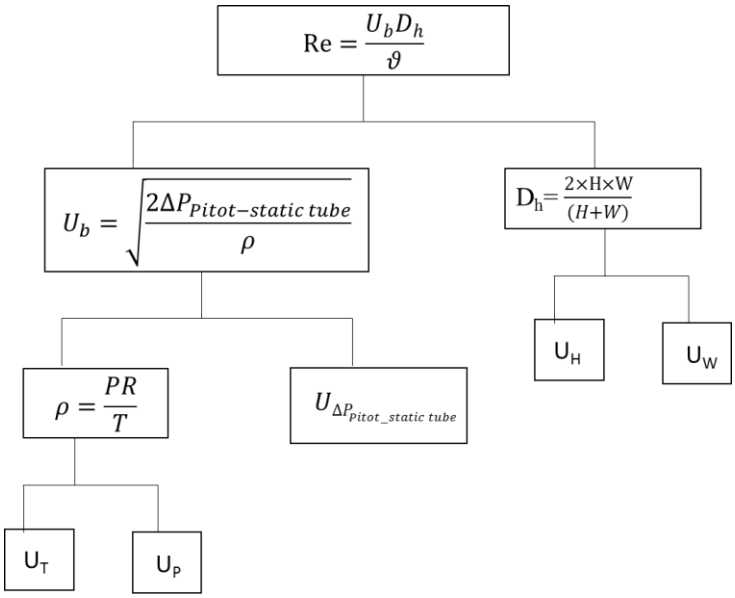

Figure 77 Uncertainty tree for Re

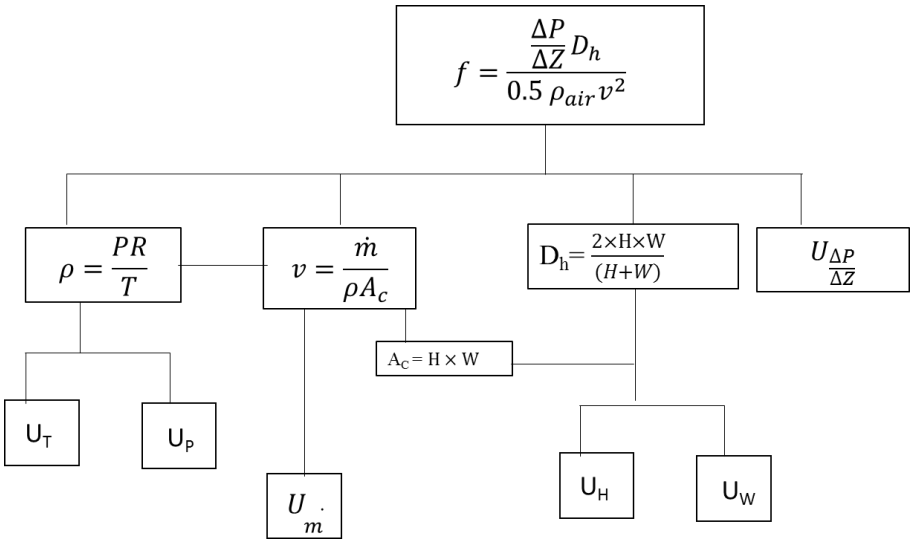

Figure 78 Uncertainty tree for friction factor

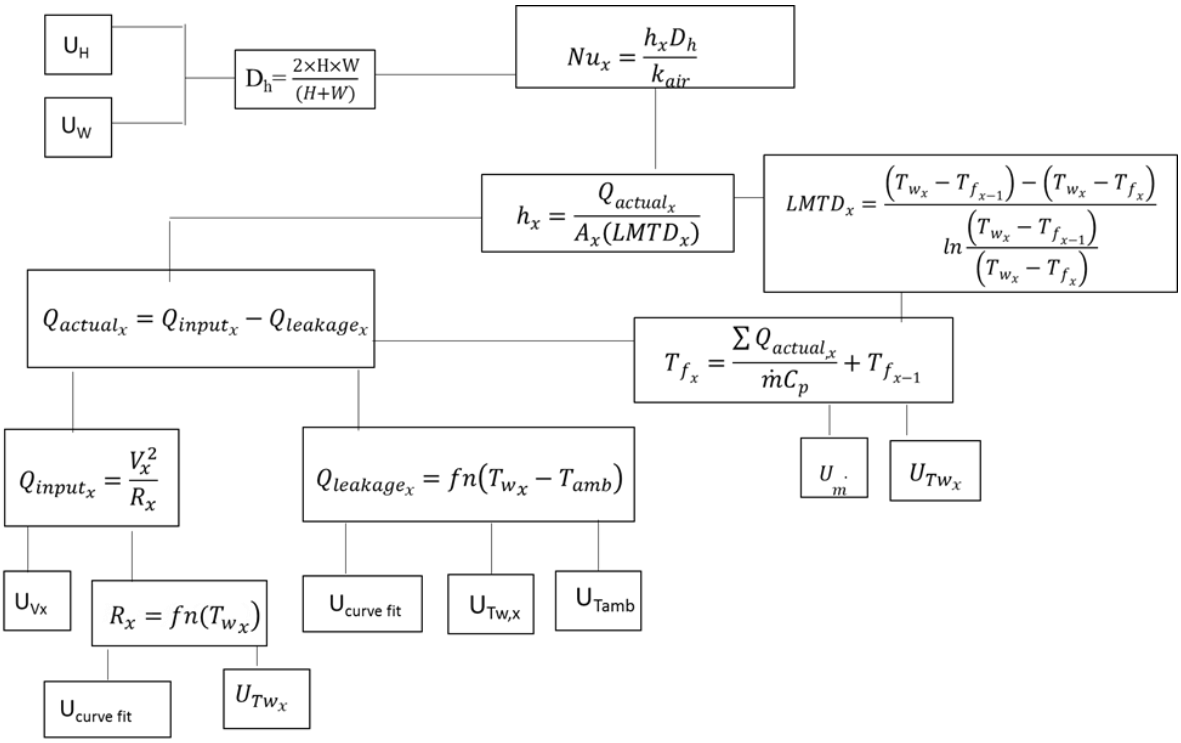

Figure 79 Uncertainty tree for Nu

APPENDIX B: PIV UNCERTAINTY

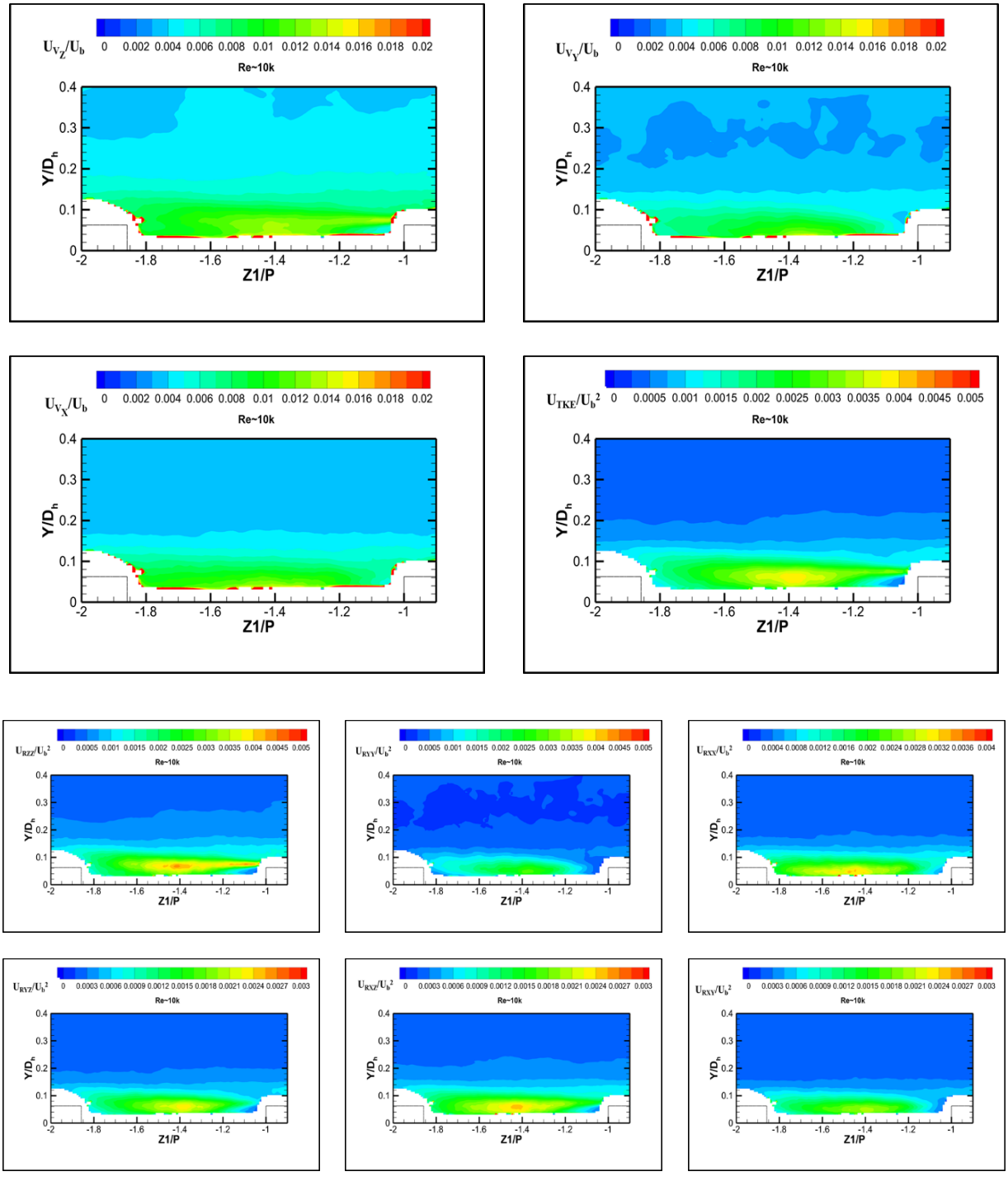

Figure 80 Uncertainties in PIV experiment at Re ≈ 10k

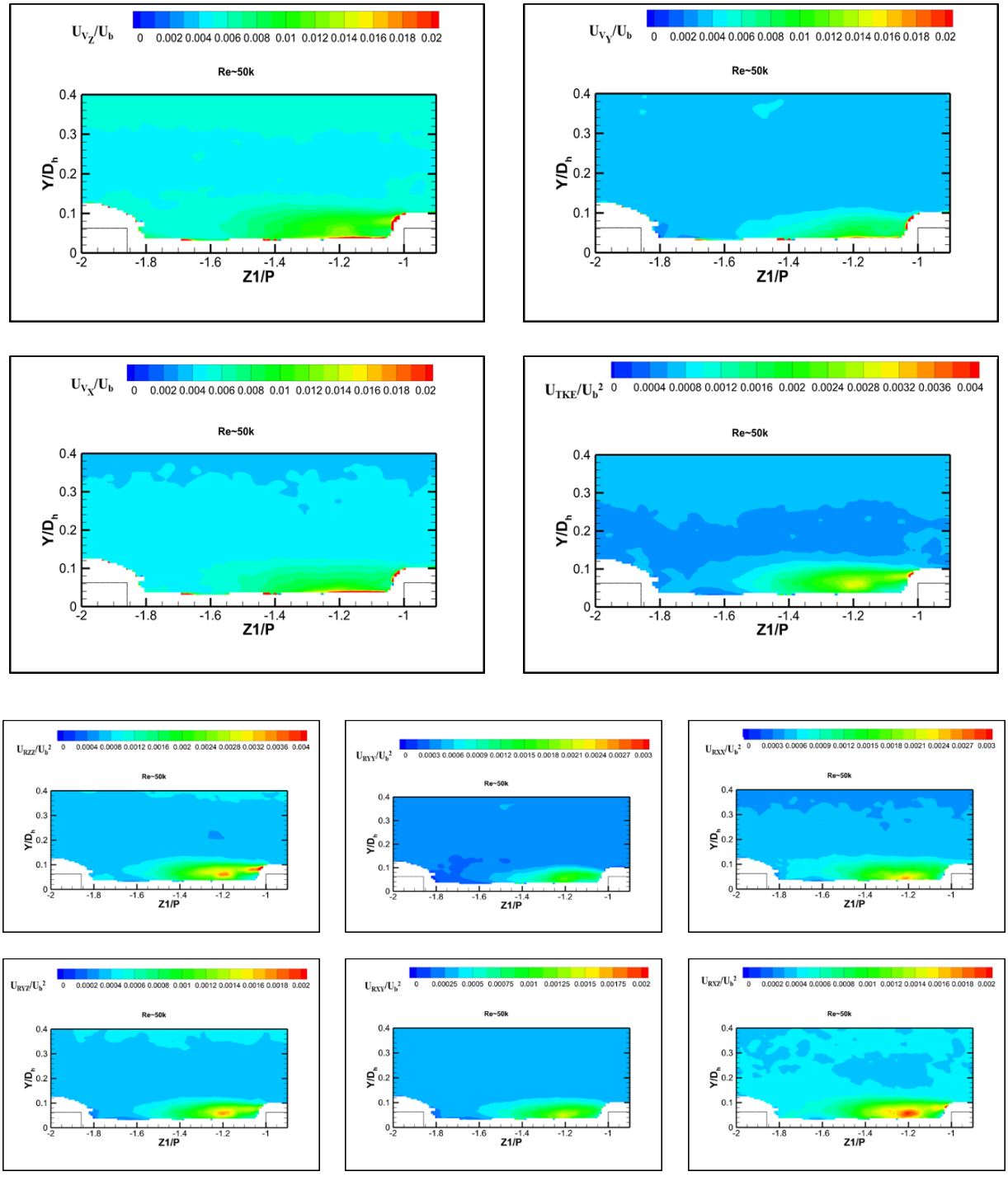

Figure 81 Uncertainties in PIV experiment at Re ≈ 50k

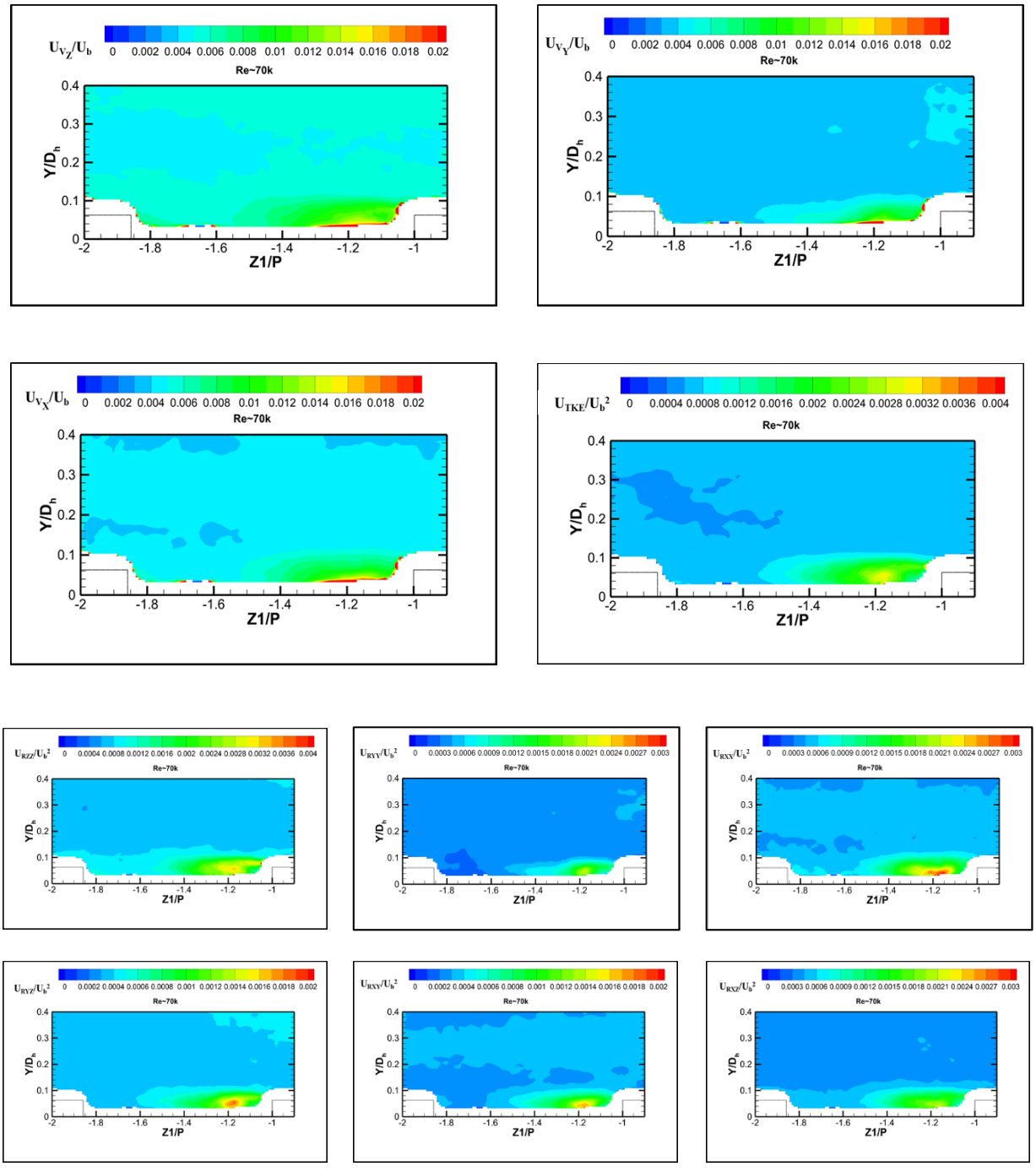

Figure 82 Uncertainties in PIV experiment at Re ≈ 70k

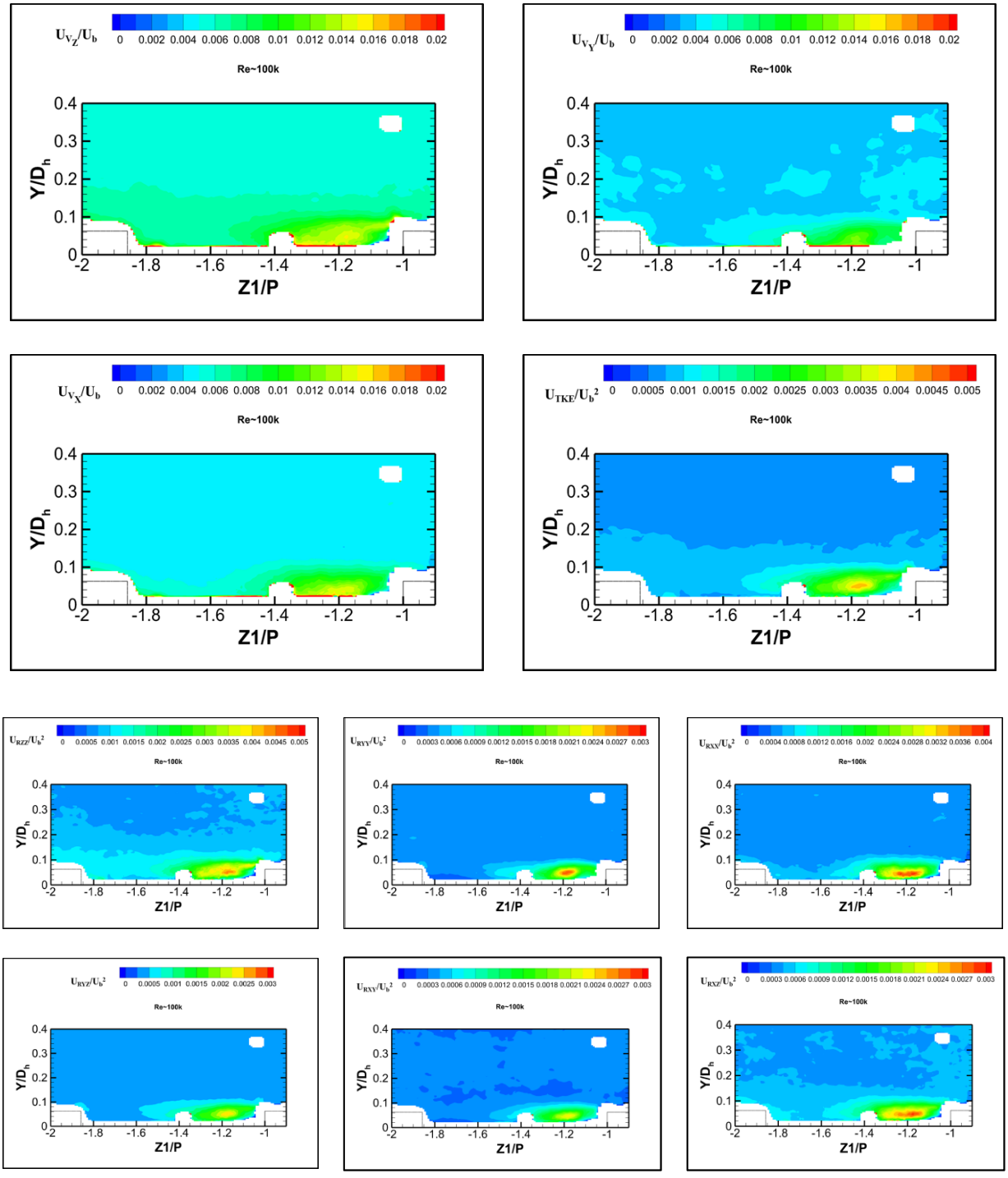

Figure 83 Uncertainties in PIV experiment at Re ≈ 100k

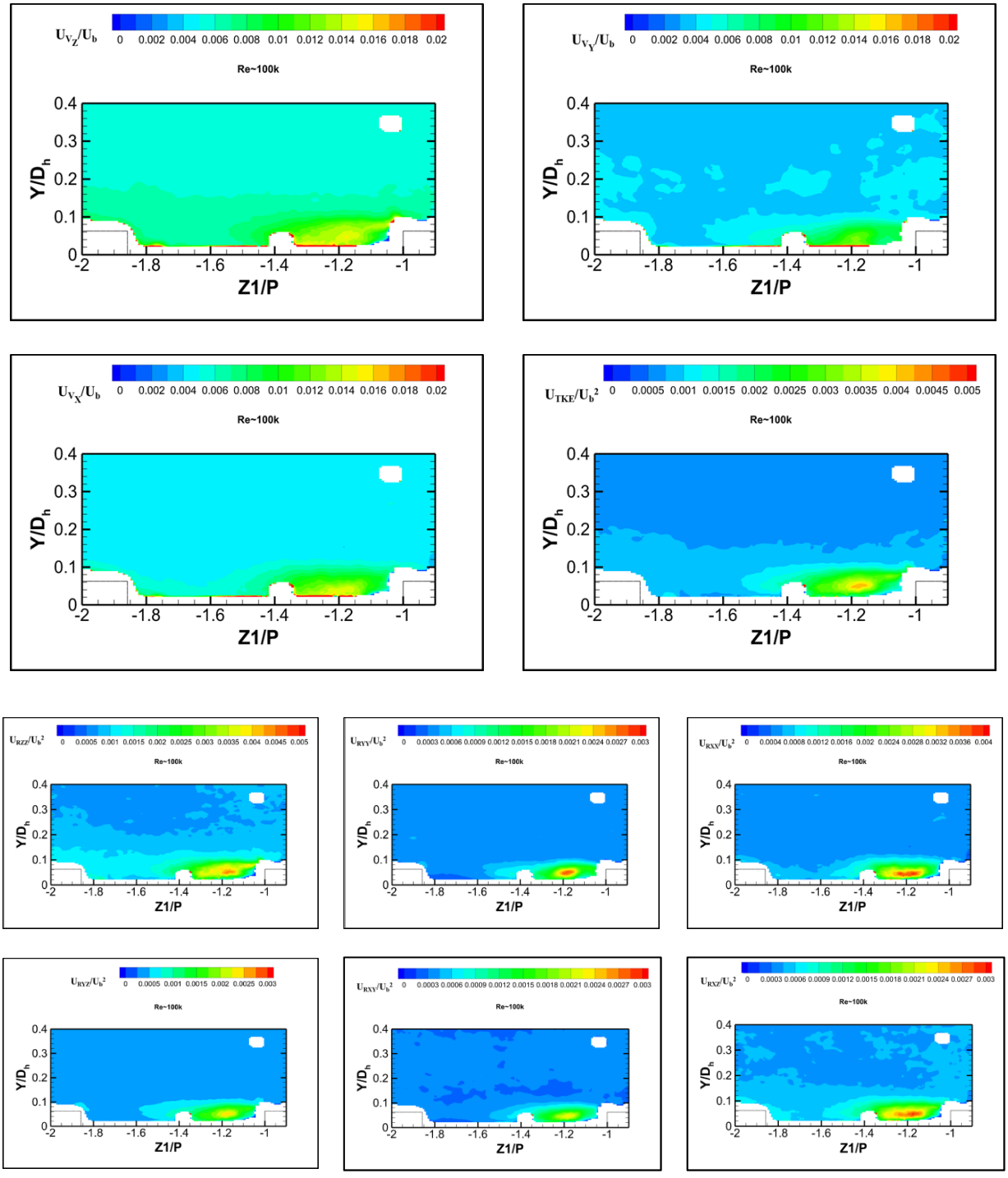

Figure 84 Uncertainties in PIV experiment at Re ≈ 100k

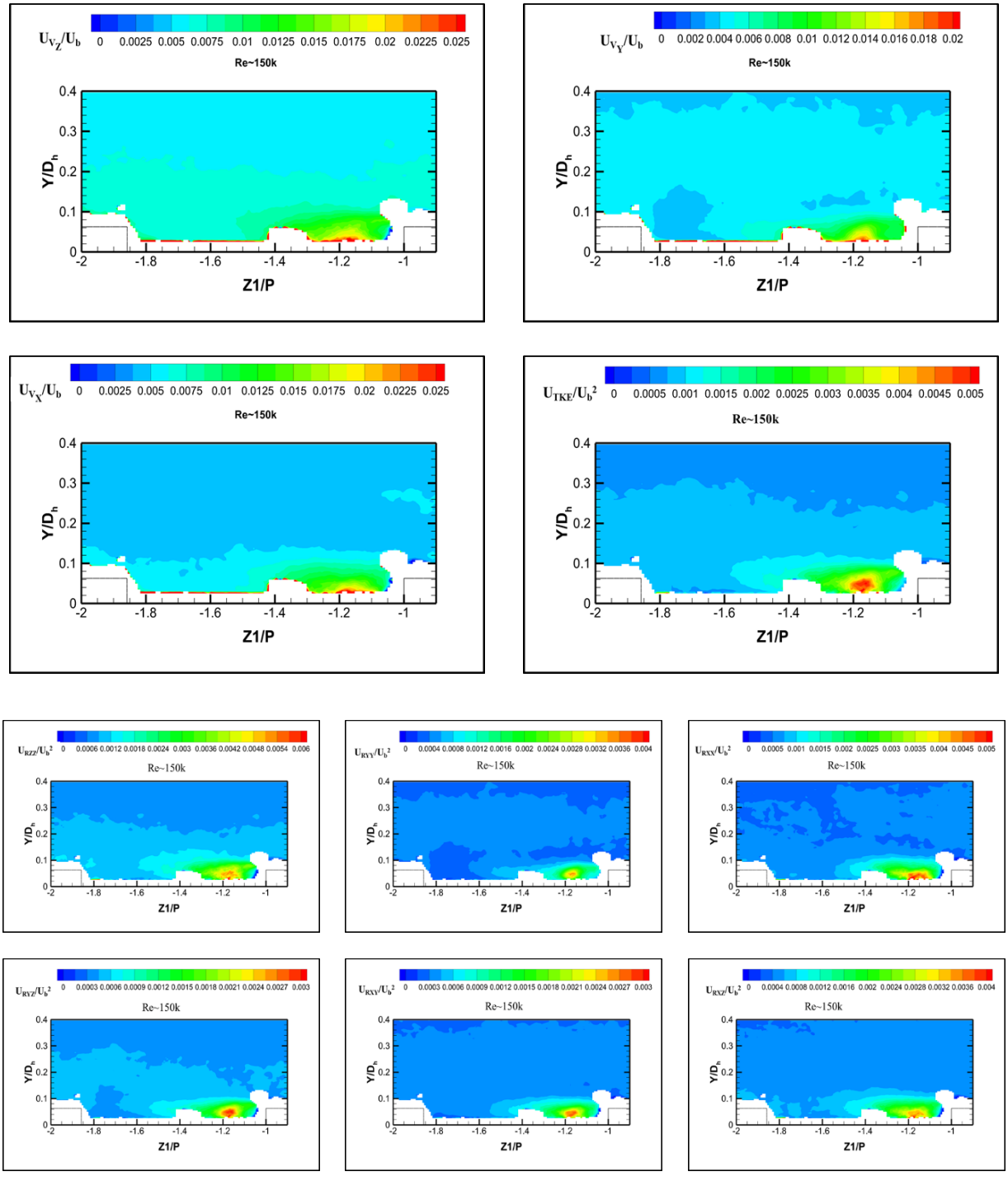

Figure 85 Uncertainties in PIV experiment at Re ≈ 150k

APPENDIX C: STATISTICAL CONVERGENCE OF LES

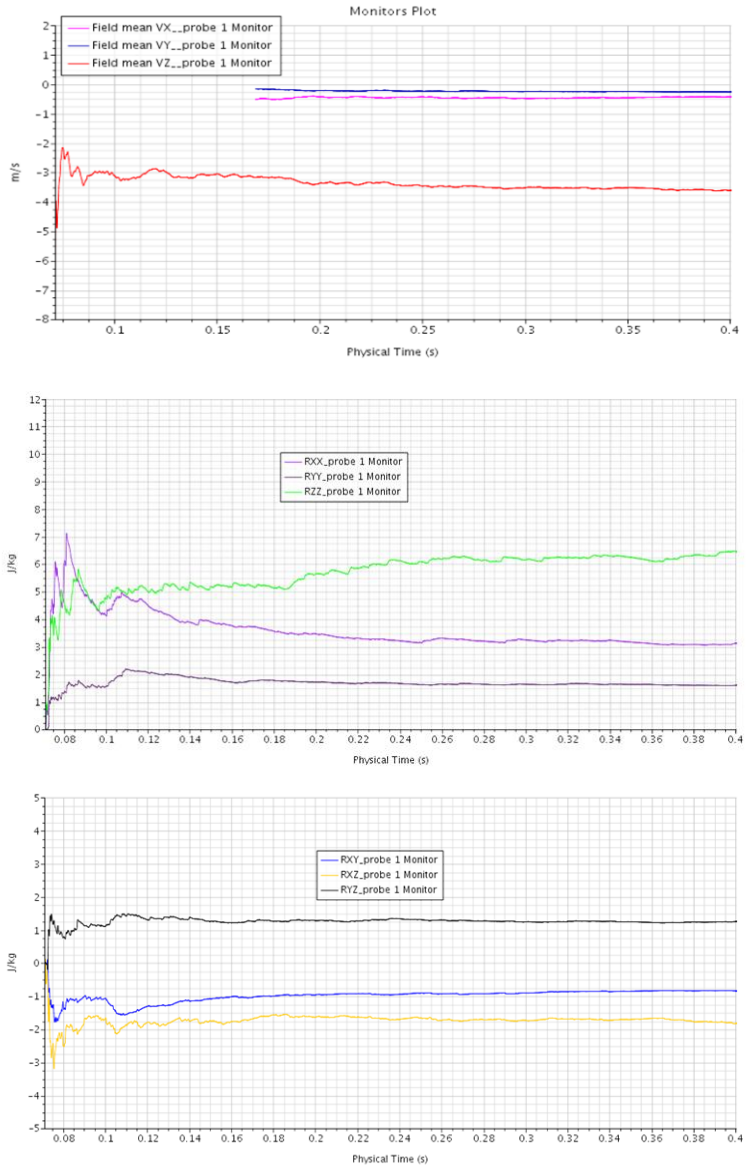

Figure 86 Statistical convergence of LES

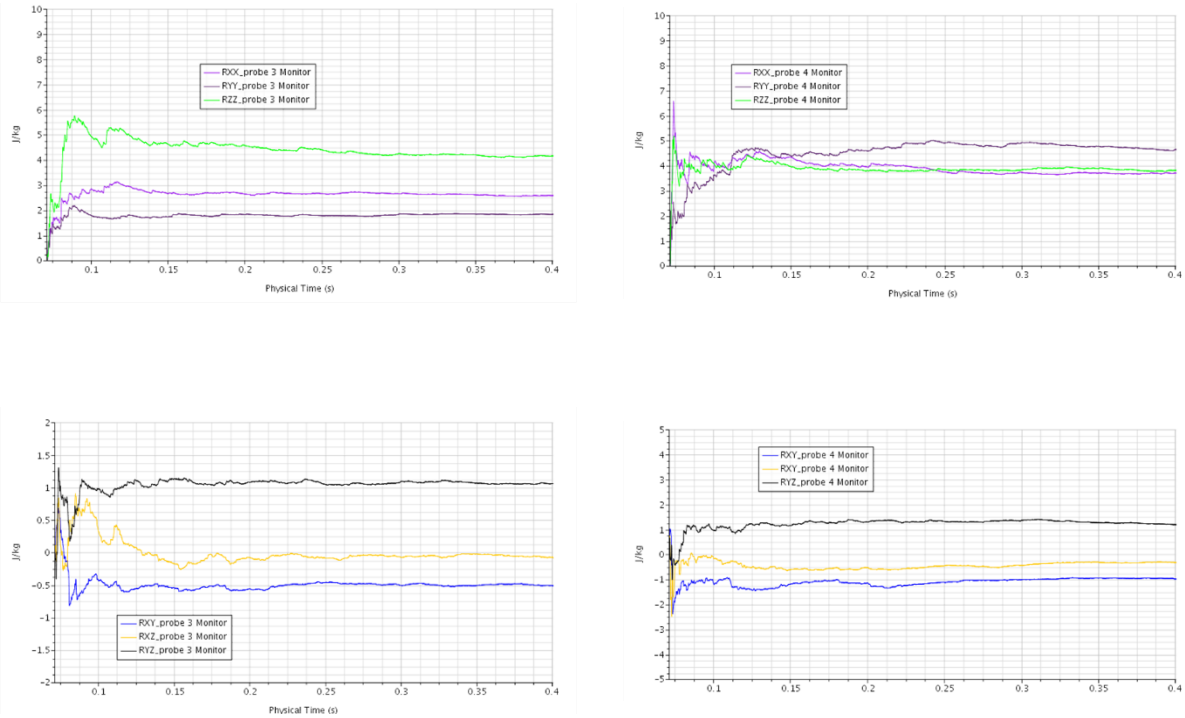

Figure 87 Statistical convergence of LES

APPENDIX D: 2D PLANER PIV MEASUREMENT

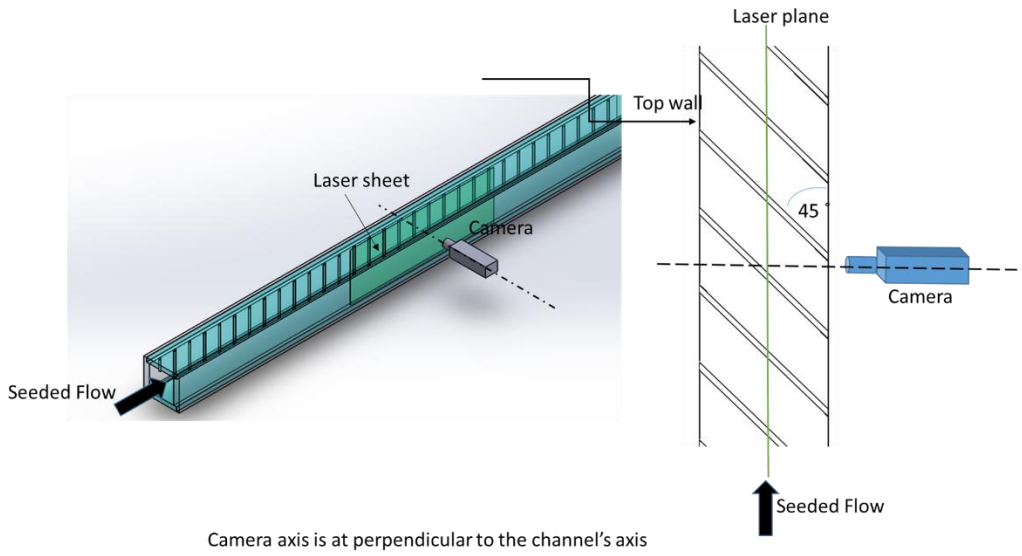

Figure 88 2D planer PIV measurement set up

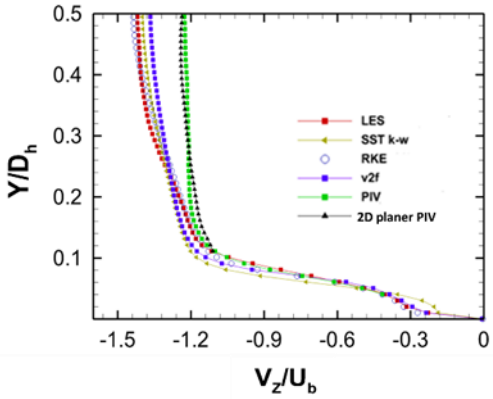

Loc $\left|\frac{Z1}{P}\right|$= 1.21 at the streamwise midplane

Figure 89 Comparative results of non-dimensional V_Z between 2D planer PIV, stereo PIV, LES, and RANS models

APPENDIX E: PERMISSION TO USE FIGURE 1 AND 2

RE: Seeking permission to use figures from your paper

Han, Je C <jc-han@tamu.edu>

Thu 10/11/2018 5:33 PM

To: Lumaya Ahmed <lumaya.ahmed@knights.ucf.edu>;

Okay.

From: Lumaya Ahmed [mailto:lumaya.ahmed@knights.ucf.edu]
Sent: Thursday, October 11, 2018 3:34 PM
To: Han, Je C <jc-han@tamu.edu>
Subject: Re: Seeking permission to use figures from your paper

Hi Dr. Han,

Thank you for your approval for using Figure 1.

I also want to use Figure 2 of the same paper with proper citation.

Je-Chin Han, "Recent Studies in Turbine Blade Cooling," International Journal of Rotating Machinery, vol. 10, no. 6, pp. 443-457, 2004.
https://doi.org/10.1155/S1023621X04000442.

I am seeking your permission to use Figure 2 of this paper in my dissertation.

Sincerely,
Lumaya Ahmed
Research Assistant
Center for Advanced Turbomachinery and Energy Research
University of Central Florida

From: Han, Je C <jc-han@tamu.edu>
Sent: Wednesday, October 10, 2018 5:33:14 PM
To: Lumaya Ahmed
Subject: RE: Seeking permission to use a figure from your papers

"I want to use Figure 1 of this paper in my dissertation with proper citation."

OKAY.

From: Lumaya Ahmed [mailto:lumaya.ahmed@knights.ucf.edu]
Sent: Wednesday, October 10, 2018 4:17 PM
To: Han, Je C <jc-han@tamu.edu>
Subject: Re: Seeking permission to use a figure from your papers

For your assistance, I have attached the paper herewith.

Thank you,
Lumaya Ahmed
Research Assistant
Center for Advanced Turbomachinery and Energy Research
University of Central Florida

From: Lumaya Ahmed
Sent: Wednesday, October 10, 2018 5:11:54 PM
To: jc-han@tamu.edu
Subject: Seeking permission to use a figure from your papers

Hi Dr. Han,

I am a PhD student in Mechanical Engineering, UCF. I am working on my dissertation on the effect of secondary flow on heat transfer and friction in square ribbed channel with 45 deg ribs. I came across one of your review papers.

Je-Chin Han, "Recent Studies in Turbine Blade Cooling ," International Journal of Rotating Machinery, vol. 10, no. 6, pp. 443-457, 2004.
https://doi.org/10.1155/S1023621X04000442.

I want to use Figure 1 of this paper in my dissertation with proper citation.

I hope you will kindly allow me to use the figure in my dissertation..

Thank you,

Lumaya Ahmed
Research Assistant
Center for Advanced Turbomachinery and Energy Research
University of Central Florida

REFERENCES

[1] J. C. Han, "Recent Studies in Turbine Blade Cooling," *International Journal of Rotating Machinery,* vol. 10, no. 6, pp. 443-457, 2004.

[2] J. C. Han, S. Dutta and S. Ekkad, Gas Turbine Heat Transfer and Cooling Technology, London: Taylor & Francis Group, 2012.

[3] J. C. Han, "Heat Transfer and Friction Characteristics in Rectangular Channels With Rib Tabulators," *Journal of Heat Transfer,* vol. 110, no. 2, pp. 321-328, May 1988.

[4] J. C. Han, J. S. Park and C. K. Lei, "Heat Transfer Enhancement in Channels With Turbulence Promoters," *Journal of Engineering for Gas Turbines & Power,* vol. 107, no. 2, pp. 628-635, July 1985.

[5] J. C. Han and J. S. Park, "Developing Heat Transfer in Rectangular Channels With Rib Turbulators," *International Journal of Heat and Mass Transfer.,* vol. 31, no. 1, pp. 183-195, 1988.

[6] J. S. Park, J. C. Han, Y. Huang, S. Ou and R. J. Boyle, "Heat Transfer Performance Comparisons of Five Different Rectangular Channels With Parallel Angled Ribs," *International Journal of Heat and Mass Transfer,* vol. 35, no. 11, pp. 2891-2903, November 1992.

[7] M. E. Taslim and A. Lengkong, "45 deg Round-Corner Rib Heat Transfer Coefficient Measurement in a Square Channel," *Journal of Turbomachinery,* vol. 121, no. 2, pp. 272-280, April 1999.

[8] J. C. Bailey and R. S. Bunker, "Heat Transfer and Friction in Channels With Very High Blockage 45° Staggered Turbulators," in *Turbo Expo: Power for Land, Sea, and Air*, Atlanta, Georgia, USA, 2003.

[9] M. E. Taslim, T. Li and S. D. Spring, "Measurements of Heat Transfer Coefficients and Friction Factors in Passages Rib-Roughened on All Walls," *Journal of Turbomachinery,* vol. 120, no. 3, pp. 564-570, July 1998.

[10] M. E. Taslim and S. D. Spring, "Effects of Turbulator Profile and Spacing on Heat Transfer and Friction in a Channel," *Journal of Thermophysics and Heat Transfer,* vol. 8, no. 3, pp. 555-562, 1994.

[11] A. P. Rallabandi, H. Yang and J. C. Han, "Heat Transfer and Pressure Drop Correlations for Square Channels With 45 Deg at High Reynolds Numbers.," *Journal of Heat Transfer,* vol. 131, no. 7, p. 071703(10 pages), May 2009.

[12] A. P. Rallabandi, N. Alkhamis and J. C. Han, "Heat Transfer and Pressure Drop Measurements for a Square Channel With 45 deg Round-Edged Ribs at High Reynolds Numbers," *Journal of Turbomachinery,* vol. 133, no. 3, p. 031019(10 pages), July 2010.

[13] Y. H. Liu, L. M. Wright, W. L. Fu and J. C. Han, "Rib Spacing Effect on Heat Transfer and Pressure Loss in a Rotating Two-Pass Rectangular Channel (AR=1:2) With 45-Degree

Angled Ribs," in *ASME Turbo Expo 2006: Power for Land, Sea, and Air*, Barcelona, Spain, 2006.

[14] N. Y. Alkhamis, A. P. Rallabandi and J. C. Han, "Heat Transfer and Pressure Drop Correlations for Square Channels With V-Shaped Ribs at High Reynolds Numbers," *Journal of Heat Transfer*, vol. 133, no. 11, p. 111901(8 pages), September 2011.

[15] L. M. Wright, W. L. Fu and J. C. Han, "Thermal Performance of Angled, V-Shaped, and W-Shaped Rib Turbulators in Rotating Rectangular Cooling Channels (AR=4:1)," *Journal of Turbomachinery*, vol. 126, no. 4, pp. 604-614, December 2004.

[16] J. C. Han and Y. M. Zhang, "High Performance Heat Transfer Ducts With Parallel Broken and V-Shaped Broken Ribs," *International Journal of Heat and Mass Transfer*, vol. 35, no. 2, pp. 513-523, 1992.

[17] M. Valentino, L. Tran, M. Ricklick and J. S. Kapat, "Comparison of Heat Transfer and Friction Augmentation for Symmetric and Non-Symmetric Wedge Turbulators on Two Opposite Walls," in *47th AIAA/ASME/SAE/ASEE Joint Propulsion Conference & Exhibit*, San Diego, California, 2011.

[18] J. C. Han, J. S. Park and C. K. Lei, "Heat Transfer and Pressure Drop in Blade Cooling Channels With Turbulence Promoters," NASA Contractor Report 3837, 1984.

[19] M. E. Taslim, T. Li and S. D. Spring, "Measurements of Heat Transfer Coefficients and Friction Factors in Rib-Roughened Channels Simulating Leading-Edge Cavities of a Modern Turbine Blade," *Journal of Turbomachinery*, vol. 119, no. 3, pp. 601-609, July 1997.

[20] N. Domaschke, J. V. Wolfersdorf and K. Semmler, "Heat Transfer and Pressure Drop Measurements in a Rib Roughened Leading Edge Cooling Channel," *Journal of Turbomachinery,* vol. 134, no. 6, p. 061006(9 pages), August 2012.

[21] J. Lei, J. C. Han and M. Huh, "Effect of Rib Spacing on Heat Transfer in a Two Pass Rectangular Channel (AR=2:1) at High Rotation Numbers," *Journal of Heat Transfer,* vol. 134, no. 9, p. 091901 (9 pages), July 2012.

[22] M. Huh, J. Lei and J. C. Han, "Influence of Channel Orientation on Heat Transfer in a Two-Pass Smooth and Ribbed Rectangular Channel (AR=2:1) Under Large Rotation Numbers.," *Journal of Turbomachinery,* vol. 134, no. 1, p. 011022(14 pages), June 2012.

[23] M. A. Smith, R. M. Mathison and M. Dunn, "Heat Transfer for High Aspect Ratio Rectangular Channels in a Stationary Serpentine Passage With Turbulated and Smooth Surfaces," in *ASME Turbo Expo 2013: Turbine Technical Conference and Exposition*, San Antonio, Texas, USA, June, 2013.

[24] A. Rallabandi, J. Lei, J. C. Han, S. Azad and C. P. Lee, "Heat Transfer Measurements in Rotating Blade-Shape Serpentine Coolant Passage With Ribbed Walls at High Reynolds Numbers," *Journal of Turbomachinery,* vol. 136, no. 9, pp. 091004-9, March 2014.

[25] S. F. Yang, J. C. Han, S. Azad and C. P. Lee, "Heat Transfer in Rotating Serpentine Coolant Passage With Ribbed Walls at Low Mach Number," *Journal of Thermal Science and Engineering Applications,* vol. 7, no. 1, p. 011013 (11 pages), March 2015.

[26] S. Acharya, S. Dutta, T. A. Myrum and R. S. Baker, "Periodically Developed Flow and Heat Transfer in a Ribbed Duct," *International Journal of Heat and Mass Transfer,* vol. 36, no. 8, pp. 2069-2082, 1993.

[27] D. L. Rigby, E. Steinthorsson and A. A. Ameri, "Numerical Prediction of Heat Transfer in a Channel With Ribs and Bleed," in *ASME 1997 International Gas Turbine and Aeroengine Congress and Exhibition*, Orlando, Florida, 1997.

[28] Y. J. Jang, H. C. Chen and J. C. Han, "Flow and Heat Transfer in a Rotating Square Channel With 45 deg Angled Ribs by Reynolds Stress Turbulence Model," *Journal of Turbomachinery*, vol. 123, no. 1, pp. 124-132, 2000.

[29] S. V. Ekkad and J. C. Han, "Detailed Heat Transfer Distributions in Two-Pass Square Channels With Rib Turbulators," *International Journal of Heat and Mass Transfer,* vol. 40, no. 11, pp. 2525-2537, July 1997.

[30] M. E. Taslim and A. Lengkong, "45 deg Staggered Rib Heat Transfer Coefficient Measurements in a Square Channel," *Journal of Turbomachinery*, vol. 120, no. 3, pp. 571-580, July 1998.

[31] G. Rau, M. Çakan, D. Moeller and T. Arts, "The Effect of Periodic Ribs on the Local Aerodynamic and Heat Transfer Performance of a Straight Cooling Channel," *Journal of Turbomachinery*, vol. 120, no. 2, pp. 368-375, April 1998.

[32] S. Y. Son, K. D. Kihm and J. C. Han, "PIV Flow Measurements for Heat Transfer Characterization in Two-Pass Square Channels With Smooth and 90° Ribbed Walls,"

International Journal of Heat and Mass Transfer, vol. 45, no. 24, p. 4809–4822, November 2002.

[33] L. Casarsa and T. Arts, "Experimental Investigation of the Aerothermal Performance of a High Blockage Rib-Roughened Cooling Channel," *Journal of Turbomachinery*, vol. 127, no. 3, pp. 580-588, January 2005.

[34] T. M. Liou, S. W. Chang, S. P. Chan and Y. S. Liu, "Particle Image Velocimetry Measurements in a Two-Pass 90 Degree Ribbed-Wall Parallelogram Channel," *Journal of Turbomachinery*, vol. 137, no. 4, p. 041012(10 pages), April 2015.

[35] X. Gao and B. Sunde´n, "Effects of Inclination Angle of Ribs on the Flow Behavior in Rectangular Ducts," *Journal of Fluids Engineering*, vol. 126, no. 4, pp. 692-699, September 2004.

[36] X. Gao and B. Sunde´n, "PIV Measurement of the Flow Field in Rectangular Ducts With 60° Parallel, Crossed and V-Shaped Ribs," *Experimental Thermal and Fluid Science*, vol. 28, no. 6, pp. 639-653, June 2004.

[37] J. Schabacker, A. Boelcs and B. V. Johnson, "PIV Investigation of the Flow Characteristics in an Internal Coolant Passage with 45deg Rib Arrangement," in *International Gas Turbine & Aeroengine Congress & Exhibition*, Indianapolis, Indiana, 1999.

[38] D. Chanteloup, Y. Juaneda and A. Bölcs, "Combined 3-D Flow and Heat Transfer Measurements in a 2-Pass Internal Coolant Passage of Gas Turbine Airfoils," *Journal of Turbomachinery*, vol. 124, no. 4, pp. 710-718, November 2002.

[39] F. Coletti, T. Maurer and T. Arts, "Flow Field Investigation in Rotating Rib-Roughened Channel by Means of Particle Image Velocimetry," *Experiments in Fluids,* vol. 52, no. 4, p. 1043–1061, April 2012.

[40] P. Burattini, S. Leonardi, P. Orlandi and R. A. Antonia, "Comparison Between Experiments and Direct Numerical Simulations in a Channel Flow With Roughness in One Wall," *Journal of Fluid Mechanics,* vol. 600, pp. 403-426, April 2008.

[41] S. Leonardi, P. Orlandi, R. J. Smalley, L. Djenidi and R. A. Antonia, "Direct Numerical Simulations of Turbulent Channel Flow With Transverse Square Bars on One Wall," *Journal of Fluid Mechanics,* vol. 491, p. 229–238, 2003.

[42] P. Orlandi and S. Leonardi, "DNS of Turbulent Channel Flows with Two- and Three-Dimensional Roughness," *Journal of Turbulence,* vol. 7, p. 1–22, 2006.

[43] J. Tyacke and P. G. Tucker, "Large Eddy Simulation of Turbine Internal Cooling Ducts," *Computers & Fluids 1,* vol. 14, p. 130–140, July 2015.

[44] S. Kubacki, J. Rokicki and E. Dick, "Hybrid RANS/LES of Flow in a Rib-Roughened Rotating Channel," in *ASME Turbo Expo 2014: Turbine Technical Conference and Exposition*, Düsseldorf, Germany, 2014.

[45] S. Patil and D. Tafti, "Large-Eddy Simulation With Zonal Near Wall Treatment of Flow and Heat Transfer in a Ribbed Duct for the Internal Cooling of Turbine Blades," *Journal of Turbomachinery,* vol. 135, no. 3, p. 031006 (11 pages), March 2013.

[46] O. Labbé, "Large-Eddy-Simulation of Flow and Heat Transfer in a Ribbed Duct," *Computers & Fluids,* vol. 76, pp. 23-32, May 2013.

[47] C. Kang and K. S. Yang, "Characterization of Turbulent Heat Transfer in Ribbed Pipe Flow," *Journal of Heat Transfer,* vol. 138, no. 4, p. 041901 (9 pages), January 2016.

[48] E. A. Sewall, D. K. Tafti, A. B. Graham and K. A. Thole, "Experimental Validation of Large Eddy Simulations of Flow and Heat Transfer in a Stationary Ribbed Duct," *International Journal Heat and Fluid Flow,* vol. 27, no. 2, pp. 243-258, April 2006.

[49] M. Tyagi and S. Acharya, "Large Eddy Simulations of Flow and Heat Transfer in Rotating Ribbed Duct Flows," *Journal of Heat Transfer,* vol. 127, no. 5, pp. 486-498, May 2005.

[50] K. Watanabe and T. Takahashi, "LES Simulation and Experimental Measurement of Fully Developed Ribbed Channel Flow and Heat Transfer," in *ASME Turbo Expo 2002: Power for Land, Sea, and Air*, Amsterdam, The Netherlands, 2002.

[51] D. K. Tafti, "Large-Eddy Simulations of Heat Transfer in a Ribbed Channel for Internal Cooling of Turbine Blades," in *ASME Turbo Expo 2003*, Atlanta, Georgia, 2003.

[52] J. Cui, V. C. Patel and C. L. Lin, "Large-Eddy Simulation of Turbulent Flow in a Channel With Rib Roughness," *International Journal of Heat and Fluid Flow,* vol. 24, no. 3, pp. 372-388, June 2003.

[53] C. D. Dritselis, "Large Eddy Simulation of Turbulent Channel Flow with Transverse Roughness Elements on One Wall," *International Journal of Heat and Fluid Flow,* vol. 50, p. 225–239, 2014.

[54] S. Leonardi, E. Mostarda, P. Orlandi and R. A. Antonia, "Turbulent Channel Flow With Rod and Square Bar Roughness on One Wall," in *16th AIMETA Congress of Theoretical and Applied Mechanics*, 2003.

[55] S. A. Wahab and D. K. Tafti , "Large Eddy Simulation of Flow and Heat Transfer in a Staggered 45° Ribbed Duct," in *ASME Turbo Expo 2004: Power for Land, Sea, and Air*, Vienna, Austria, 2004.

[56] R. Jia, B. Sundén and M. Faghri, "Computational Analysis of Heat Transfer Enhancement in Square Ducts With V-Shaped Ribs: Turbine Blade Cooling," *Journal of Heat Transfer*, vol. 127, no. 4, pp. 426-433, March 2005.

[57] J. Holgate, A. Skillen, T. Craft and A. Revell, "A Review of Embedded Large Eddy Simulation for Internal Flows," *Archives of Computational Methods in Engineering*, pp. 1-18, 2018.

[58] H. Tennekes and J. L. Lumley, A first Course in Turbulence, London, England: The MIT Press, 1987.

[59] S. B. Pope, Turbulent Flows, Cambridge University Press, 2000.

[60] F. M. White, Viscous Fluid Flow, McGraw-Hill, 1991.

[61] M. P. Bulat and P. V. Bulat, "Comparison of Turbulence Models in the Calculation of Supersonic Separated Flows," *World Applied Sciences Journal*, vol. 27, no. 10, pp. 1263-1266, 2013.

[62] D. C. Wilcox and M. W. Rubesin, "Progress in Turbulence Modeling for Complex Flow Fields Including Effects of Compressibility," Washington, USA, 1980.

[63] M. Behnia, S. Parneix, Y. Shabany and P. A. Durbin, "Numerical Study of Turbulent Heat Transfer in Confined and Unconfined Impinging Jets," *International Journal of Heat and Fluid Flow*, vol. 20, no. 1, pp. 1-9, February 1999.

[64] M. Germano, U. Piomelli, P. Moin and W. H. Cabot, "A Dynamic Subgrid-Scale Eddy Viscosity Model," *Physics of Fluids A: Fluid Dynamics,* vol. 3, no. 7, pp. 1760-1765, 1991.

[65] F. Nicoud and F. Ducros, "Subgrid-Scale Stress Modelling Based on the Square of the Velocity Gradient Tensor," *Flow, Turbulence and Combustion,* vol. 62, no. 3, pp. 183-200, 1999.

[66] S. V. Patankar, C. H. Liu and E. M. Sparrow, "Fully Developed Flow and Heat Transfer in Ducts Having Streamwise-Periodic Variations of Cross-Sectional Area," *Journal of Heat Transfer,* vol. 99, no. 2, pp. 180-186, May 1977.

[67] L. Ahmed, P. Tran, C. Vergos, E. Fernandez, L. Mears, J. Rodrigues and J. Kapat, "A Comparative Evaluation of Heat Transfer and Friction Behavior of a Square Channel with Sharp and Rounded 45° Ribs at Wide Range of Reynolds Numbers using Experimental and Numerical Computation," in *52nd AIAA/SAE/ASEE Joint Propulsion Conference*, Salt Lake City,Utah, USA, 2016.

[68] L. Ahmed, C. Vergos, P. K. Tran, W. Wang and J. Kapat, "Investigation of Pressure Drop and Heat Transfer Behavior of a Square Channel With 45° Angle Ribs at Wide Range of Reynolds Numbers," in *51st AIAA/SAE/ASEE Joint Propulsion Conference,* Orlando, FL., 2015.

[69] C. Vergos, L. Ahmed, P. Tran, T. Buchanan, E. Fernandez and J. Kapat, "Investigation of Pressure Drop and Heat Transfer Behavior of a Square Channel with 45° Angle Turbulators on One and Two Wall Configuration," in *52nd AIAA/SAE/ASEE Joint Propulsion Conference*, Salt Lake City, Utah, USA, 2016.

[70] R. L. Webb, "Performance Evaluation Criteria for Use of Enhanced Heat Transfer Surfaces in Heat Exchanger Design," *International Journal of Heat and Mass Transfer,* vol. 24, no. 4, pp. 715-726, April 1981.

[71] D. L. Gee and R. L. Webb, "Forced Convection Heat Transfer in Helically Rib-Roughened Tubes," *International Journal of Heat and Mass Transfer,* vol. 23, no. 8, pp. 1127-1136.

[72] "ASME PTC 19.1-2005 Test Uncertainty," ASME, 2006.

[73] S. J. Kline and F. A. McClintock, "Describing Uncertainties in Single Sample Experiments.," *Mechanical Engineering,* vol. 75, no. 1, pp. 3-8, 1953.

[74] R. J. Moffat, "Using Uncertainty Analysis in the Planning of an Experiment," *Journal of Fluids Engineering,* vol. 107, no. 2, pp. 173-181, June 1985.

[75] B. Wieneke and K. Pfeiffer, "Adaptive PIV With Variable Interrogation Window Size and Shape," in *15th Int Symp on Applications of Laser Techniques to Fluid Mechanics*, Lisbon, Portugal, 2010.

[76] B. Wieneke and A. Sciacchitano, "PIV Uncertainty Propagation," in *11th International Symposium on Particle Image Velocimetry-PIV15,* Santa Barbara, California, 2015.

[77] B. Wieneke, "Generic A-Posteriori Uncertainty Quantification for PIV Vector Fields by Correlation Statistics," in *17th International Symposeum on Application of Laser Techniques to Fluid Mechanics,* Lisbon, Portugal, 2014.

[78] U. Piomelli and J. Chasnov, Large Eddy Simulations: Theory and Applications., vol. vol 2, Springer, 1991, pp. 269-336.

[79] M. Schüler, F. Zehnder, B. Weigand, J. V. Wolfersdorf and S. O. Neumann, "The Effect of Turning Vanes on Pressure Loss and Heat Transfer of a Ribbed Rectangular Two-Pass Internal Cooling Channel," *Journal of Turbomachinery,* vol. 133, no. 2, p. 021017(10 pages), October 2011.

[80] J. Jeong and F. Hussain, "On the Identification of a Vortex," *Journal of Fluid Mechanics,* vol. 285, pp. 69-94, 1995.